Scanning Electron Microscopy for Nano-morphology Characterisation of Complex Hierarchical Polymer Structures

By:

Nicola Alessandra Stehling

A thesis submitted in partial fulfilment of the requirements for the degree of Doctor of Philosophy

The University of Sheffield
Faculty of Engineering
Department of Materials Science and Engineering

08/03/2020

Abstract

This thesis presents novel and innovative ways of imaging and analysing natural hierarchical polymers using low-voltage scanning electron microscopy and secondary electron energies. Materials such as plant fibres, feathers and silk, have received increased societal and scientific interest recently, while the plastic industry is faced with growing public concerns over its generation of waste, and use of petrochemical precursors. In nature, materials are produced sustainably and they furthermore exhibit inspiring mechanical performance. One such material is spider silk, which is spun at room temperature from a water-based protein gel to form a thread, which even with diameters as small as 5 μm easily suspends the weight of a palm-sized spider. It is known that the secret to spider silk's remarkable properties lies within its nanoscale structures. However, the direct observation of these nanostructures has remained difficult due to their small size and their sensitivity to chemical and mechanical alteration. This work presents novel sample preparation protocols and demonstrates their use in accessing size and location information of key nanostructures within spider silk through nanoscale observation in the scanning electron microscope. As the secondary electron spectroscopy technique employed here is relatively new, new workflows from sample preparation, over optimal imaging and spectral acquisition and novel multivariate data analysis techniques are innovated and described in detail. The rigorous consideration of the material and method are exemplified on a feather section, to show that the secondary electron energy signal in the scanning electron microscope may generate molecular composition maps on a proteinaceous structural polymer. This work lays out all requirements for unlocking the vast potential for nanoscale chemical mapping which lies in the nanoscale secondary electron signal, to further inspire ground-breaking studies into the nanostructures of complex hierarchical polymers.

Selected publications

"Mapping Polymer Molecular Order in the SEM with Secondary Electron Hyperspectral Imaging"

Robert C Masters, Nicola Stehling, Kerry J Abrams, Vikas Kumar, Martina Azzolini, Nicola M Pugno, Maurizio Dapor, Andreas Huber, Philip Schäfer, David G Lidzey, Cornelia Rodenburg
Advanced Science 6 (5), 1801752, **2019**

"Revealing spider silk's 3D nanostructure through low temperature plasma etching and advanced low-voltage SEM"

Nicola Stehling, Kerry J Abrams, Chris Holland, Cornelia Rodenburg
Frontiers in Materials 5, **2019**

"Making Sense of Complex Carbon and Metal/Carbon Systems by Secondary Electron Hyperspectral Imaging"

Kerry J Abrams, Maurizio Dapor, Nicola Stehling, Martina Azzolini, Stephan J Kyle, Jan S Schäfer, Antje Quade, Filip Mika, Stanislav Kratky, Zuzana Pokorna, Ivo Konvalina, Danielle Mehta, Kate Black, Cornelia Rodenburg
Advanced Science, 1900719, **2019**

"Exploiting Plasma Exposed, Natural Surface Nanostructures in Ramie Fibers for Polymer Composite Applications"

Sameer F Hamad, Nicola Stehling, Simon A Hayes, Joel P Foreman, C Rodenburg
Materials 12 (10), 1631, **2019**

"New perspectives on nano-engineering by secondary electron spectroscopy in the helium ion and scanning electron microscope"

Nicola Stehling, Robert Masters, Yangbo Zhou, Robert O'Connell, Chris Holland, Hongzhou Zhang, Cornelia Rodenburg
MRS Communications 8 (2), 226-240, **2018**

"Anisotropic Approach for Simulating Electron Transport in Layered Materials: Computational and Experimental Study of Highly Oriented Pyrolitic Graphite"

Martina Azzolini, Tommaso Morresi, Kerry Abrams, Robert Masters, Nicola Stehling, Cornelia Rodenburg, Nicola M Pugno, Simone Taioli, Maurizio Dapor
The Journal of Physical Chemistry C 122 (18), 10159–10166, **2018**

"Low-Voltage SEM of Natural Plant Fibers: Microstructure Properties (Surface and Cross-Section) and their Link to the Tensile Properties"

Sameer F Hamad, Nicola Stehling, Chris Holland, Joel P Foreman, Cornelia Rodenburg
Procedia Engineering 200, 295–302, **2017**

"Nanoscale mapping of semi-crystalline polypropylene"

Kerry J Abrams, Quan Wan, Nicola A Stehling, C Jiao, Abdullah C S Talari, Ihtesham Rehman, Cornelia Rodenburg
physica status solidi c 14 (12), 1700153, 2017

Selected conference presentations

2019

"Nanoscale Properties Mapping for Beam-Sensitive Materials Using Secondary Electrons"

E-MRS Spring Meeting 2019, **Nice, France**, May 2019, Symposium Z, full conference presentation

"Unlocking hyperspectral SEM image data—Principal Component Analysis and Monte Carlo Modelling"

E-MRS Spring Meeting 2019, **Nice, France**, May 2019, Symposium AA, full conference presentation

2018

"Secondary Electron Spectroscopy for Beam-Sensitive Materials – Examples, Challenges and Outlook"

19th International Microscopy Congress (IMC19), **Sydney, Australia**, September 2018, interactive poster presentation

"Inhomogeneity of Longitudinal Mechanical Properties in Spider Silk Revealed by Cryo-SEM"

10th European Solid Mechanics Conference (ESMC2018), **Bologna, Italy**, July 2018, full conference presentation

2017

"Introducing SEHI – revealing chemical contrast for mapping of surface morphology in a cellulosic biopolymer using low voltage SEM"

Microscience Microscopy Congress 2017 (mmc2017), **Manchester, UK**, July 2017, flash talk and poster

Acknowledgements

First, I would like to thank the people on the professional and academic side. I would like to thank Conny Rodenburg and Chris Holland for the guidance and support not only in PhD life, but also in my professional development. A special thanks goes out to Kerry Abrams and Rob Masters for taking me under their wings. I would like to thank the EPSRC for funding my PhD journey. I must thank Fritz Vollrath and Alex Greenhalgh for supplying me with spider silk before I became apt at spider rearing and reeling myself; I would like to thank Sameer Hamad as a colleague, collaborator and for supplying the ramie plant fibres and I thank Simon Hayes and Matthew Collinson for the generous bundle of carbon fibre. A big thanks to the Sorby Centre for Electron Microscopy, and especially to Cheryl Shaw and Le Ma, for training me on the electron microscopes and coordinating with our group to enable us to do some exciting EM experiments.

Many thanks to my assessors Beverley Inkson and Stuart Boden for making constructive suggestions and improving this work.

I will gladly remember sunny evenings in the pub with the K-floor crowd, and I am especially grateful for the support and friendship from Dan, Sam and Josh. Thank you Lauren for your candid chats and bubbly energy. I am full of love for Sheffield's climbing community—Kate, Tom, Sara, all from different walks of life but equally fun and inspiring. I am so grateful to have met the TechnoKletter crowd, even though I wish I could have been part of you sooner. Thank you, Sam, for your friendship, for being a fellow geek and for an amazing summer on Peak limestone. Alex, Ania and Caitlyn and the Reinheimer for being constants when other things move on. My family for the immense support they have given me from day one.

Thank you, Jamie, for taking me off the trodden path, and for a year which will be a tough act to follow. Thank you, Morgan, for the celebrations and the warmth. A warm thanks also to Sean for your support throughout this journey.

Contents

1 Introduction

1.1   Challenges for Material Science

The UK's position as a highly developed country and economic leader is closely linked to its past, present and one may also suppose its future material innovations. The two main challenges for the UK's materials industrial strategy are performance and sustainability: Due to its high production costs compared to developing countries around the world the UK must offer novel and better materials than those which can be cheaply produced in bulk overseas. Another major part of the UK's industrial strategy lies in the transition to a regenerative circular economy [1]. The incentive to innovate and produce sustainable materials has recently gained significant momentum, with increased customer demand and public awareness of secondary negative environmental and health effects of materials production, such as pollution, emission and waste. Thus, there is an increasing drive to limit waste generation and energy use while continuing to produce and innovate materials which guarantee the UK's place as an industry leader in the developed world.

In the modern world, the production of polymers and plastics by weight rivals that of important construction materials such as metals or concrete [2]. Polymers are distinct from other chemical compounds, consisting of a chemically bound repeating sequence of molecules which make up polymer strands or networks of varying lengths and sizes. Many different repeating molecular blocks—called monomers—can be used [3]. Although synthetic polymers have only emerged as a class of materials in the last century, their importance in today's society cannot be overstated with plastics, synthetic textiles and structural polymers being an integral part of every aspect of public life, science, engineering and manufacturing. Their versatility and widespread availability

are a vehicle towards innovation and novel material solutions. However, their prevalence is not without controversy as problems such as energy efficiency and waste are becoming more pressing for the industry and also in the eye of the general public [4–6].

It is problematic that the polymer industry still heavily relies on precursors from non-renewable fossil fuels and employs energy intensive and resource inefficient processes which generate toxic waste. New processes and materials must be developed in line with the UK's industrial strategy and to secure the its role in leading developed economies in becoming more environmentally friendly, but also to serve the country beyond short-sighted economic metrics.

1.2   Learning from Nature

Nature is a source of inspiration in solving the problem of energy and resource efficient materials, as time and time again many different remarkable natural materials and inspiring processes have evolved. Nature's building blocks—such as proteins and sugar molecules—are won from renewable biomatter and are combined into polymers via enzymatic processes at near-ambient temperatures using sustainable energy sources in a resource efficient way [7]. This is in stark contrast to the hazardous non-renewable solvents and petrochemical starting materials used in energy-intensive synthetic polymer processes which have only been systematically developed since the early 20th century.

Besides setting a precedent in production, resource efficiency and safety, natural materials are superior to synthetic polymers in some key respects. Biological polymers such as deoxyribonucleic acid (DNA) or proteins have a very well-defined length and thus molecular weight, as the sequence of their building blocks is conserved during polymerisation to a very high degree. In proteins this Angstrom-scale specificity is

defined by the amino-acid sequence, which is also called the primary protein structure. Through the assembly into higher order structures the primary structure dictates the nanoscale secondary structure, such as α-helices and β-sheets, and the tertiary and the quaternary structure of the protein [7,8]. In the case of proteinaceous structural materials, this means that the primary protein structure encodes a multiscale hierarchical material right up to the macroscale, such as in the case of a strand of spider silk [9]. This coupling and assembly of structures across length scales of many orders of magnitude results in a structural organisation which is also reflected in a distinct mechanical response, quite unlike synthetic materials. It is believed that his multiscale hierarchy is the basis of outstanding mechanical properties of some natural materials [10], and thus the key to engineering novel high-performance materials.

Ultimately, the goal is to combine the best of both worlds: to produce materials industrially and in larger volumes, with the resource efficiency and the remarkable and tailored material performance inspired by natural structural materials. To even start to understand what novel nature-inspired materials may look like, it is necessary to understand the key properties which set apart natural structural polymers from their synthetic counterparts.

1.3   Role and limitations of characterisation

To uncover the secret of nature and her materials, one may use one of hundreds of analytical techniques available to chemists, biologists and material scientists. They all answer different questions, and when considering the time and money spent asking the overarching question "What makes nature's most inspiring materials so remarkable?" one may expect that the secrets are largely uncovered, and that one can start making synthetic materials following nature's blueprint. However, for many of nature's material systems this is still not the case. One explanation for this may be that the complex

hierarchical structural build-up of biopolymers means that they, perhaps more so than classic synthetic polymers, must be understood beyond their chemical composition if one is to understand where their properties originate from. Many analytical techniques probe information within a limited length-scale window, making it difficult to characterise key multi-scale interactions. Thus, despite the wealth of information present about these materials, it is still a challenge to consolidate past research efforts into a larger picture or even a multiscale-model, with many previously proposed models still not sufficiently considering all of the levels of structural order which are known to exist. Of the structures which have been characterised chemically, many are not characterised in space—that is, the questions "Where are they" or more specifically "How are they distributed" is not sufficiently answered [11]. Despite all available experimental techniques, it is still a technical challenge to fully understand these multiscale structures with regards to their size, distribution, chemical identity and their mechanical response.

1.4   Charged particle microscopy for natural structural polymers

An effective way of determining material properties throughout space is microscopy. The three largest fields of microscopy are optical, scanning probe and charged particle microscopy, which are named after the way in which the material is probed to generate an image. In the broadest sense, optical microscopy detects interactions of the material with light and is a highly developed field with many different established approaches and experimental set-ups. However, optical microscopy is inherently limited by the optical resolution limit, which complicates the acquisition of images of more than 250 nm resolution [12]. Ground-breaking and Nobel-prize winning super-resolution techniques surpass this limit and reach resolution of below 10 nm [13], although the developments have reached a limitation in their requirement for great skill and meticulous sample preparation [12]. Detailed preparation and staining protocols may be

necessary to create optical contrast between different components in the material, and compositional information beyond optical absorption and emission may only be attained by coupling microscopy to other techniques in more complex experimental designs.

Scanning probe microscopy includes atomic force microscopy (AFM) and scanning tunnelling microscopy (STM), of which only AFM is of use in the investigation of insulating materials such as polymers. In AFM, a nanoscale probing tip is scanned across the sample, and its interaction with the material is measured to generate maps of topography and other material properties deduced from the interaction of the tip with the sample surface. AFM can produce topography maps and quantify other local material properties, such as the mechanical response of the surface to tip indentation, spanning multiple length scales down to the atomic level. For soft materials, interactions between the tip and the surface can be complex and may be described by different models to fit the raw data and extract material properties throughout the scanned area [14,15]. The requirement of time and computing power has previously limited the field of view which can be analysed and mapped at once. Nonetheless, AFM has been widely applied to soft and biological materials [16,17], and the current hurdles to applying AFM to soft materials benefit from advances in automated processing strategies.

In charged particle microscopy the sample is impinged by ions or electrons which have been accelerated to a defined energy, and the resulting signal is measured to generate an image or micrograph. The impact of ions and especially electrons onto a material results in many different signals, such as secondary electrons, secondary ions, X-rays and light. Thus, many experiments can be performed in-situ to obtain spatially resolved chemical and structural information. The helium ion microscope (HeIM) is a recent innovation in the field [18] and its role compared to much older and established electron and ion microscopes is discussed in detail in Chapter 4.

Electron microscopes are very well equipped micro- and nanoanalysis tool for metals and inorganic samples and has been a workhorse for such materials and their innovation for nearing a century. When looking to apply the capabilities of EM to the materials of interest for this project, there are some challenges: Firstly, most polymers are insulators and the exposure of an insulating sample to a charged particle beam can lead to charge build up, which will distort further measurement due to local electric fields occurring where the charge cannot be removed in time. Secondly, softer, carbon-based materials such as polymers are more susceptible to damage from charged particle beams, and finally, many microanalysis tools in electron microscopes only have limited information content for carbon-based materials where the atomic composition is already known.

The solution of the first two problems lies in the application of low voltage scanning electron microscopy (LV-SEM). Low electron beam voltages (500 eV to 2 keV) and low currents (typically 5–50 pA), are used to limit damage and charging behaviour of otherwise challenging samples. Thus, there is no need for a conductive coating and the real sample surface is exposed ready for microanalysis—which leads us to the question which micro- and nanoanalysis tools are useful for soft materials in the SEM?

At low currents and voltages, the signals usually used for microanalysis—namely X-rays and back scattered electrons (BSEs)—have very low yields and unsatisfactory spatial resolution. However, the yield of secondary electrons for low atomic number materials such as polymers is highest at these low voltages [19,20], making them the ideal signal to focus on. Traditionally, and especially in the case of coated samples, the secondary electron signal is only taken for its topographical information, as the edge effect makes the images easy to interpret by the human eye. However, secondary electrons contain respond to chemical and multiscale structural properties as well [21] and may map many material properties of interest, such as order, crystallinity and

polymer composition [22–26], and thus are a major vehicle to achieving the aims of this project.

1.5   Modern Data Analysis Strategies

In close correlation to Moore's predictions about the rapid exponential improvement of electrical components [27], the amount of available and affordable computing power has skyrocketed in the last 30 years [28]. Digital data capture has long replaced the exposure of photosensitive films in electron microscopy, and the collection of larger and larger data sets has become commonplace. To unlock the extra information contained within such increasingly large data, new data analysis strategies are required, as simple data analysis tools may become too time or resource intensive. One method of dealing with large multivariate data sets is multivariate analysis (MVA), for example in the form of a principal component analysis (PCA) [29], in which an algorithm determines which components best describe the signals and their variation within the dataset. In effect this reduces the dimensionality of the data to facilitate interpretation and communication of results while still considering the entirety of the available data. For spectral data sets from different instruments negative intensity values are unphysical so the commonly employed algorithm is that of the non-negative matrix factorisation (NMF) [30]. Chapter 5 and 6 of this work utilise MVA strategies and demonstrate their power in making sense of large spectral image data sets.

1.6   Aims

The aim of this project is to develop and apply advanced low-voltage SEM (LV-SEM) techniques to map and characterise hierarchical structures of natural structural polymers down to the nanoscale, and to correlate these to macroscale mechanical properties. Spatial analysis of secondary electron energy signals through energy spectroscopy and secondary electron hyperspectral imaging (SEHI) in the SEM have

been developed as powerful analytical tools to reveal these nanoscale structures with advantages over other nano-scale resolution techniques.   In doing so, modern workflows for successful imaging and spectral acquisition have been established and novel tools for specialised data analysis have been developed.

Biopolymer multiscale structures have the potential to inspire breakthroughs in the polymer industry and to achieve step changes in making novel high-performance polymers efficiently. By supplying the research community with spatially-resolved property maps of the materials of interest, this project aims to contribute to novel models of these remarkable materials and thus to an in-depth understanding of hierarchical polymer systems.

1.7   Comments on Thesis Structure

As part of the completion of this project this thesis is presented in the alternate format, with two peer-reviewed and published papers (Chapters 4 and 7) and two traditional results chapters (Chapter 5 and 6). Comments follow which will help the reader understand the published papers in the context of the aims stated above and in the thesis as a coherent body of work.

Chapter 4 presents the paper "New Perspectives on Nano-engineering by Secondary Electron Spectroscopy in the Helium Ion and Scanning Electron Microscope" [31] as a forward-looking review which discusses the potential of secondary electron spectroscopy and hyperspectral imaging in both the SEM and the Helium Ion microscope (HeIM). This paper includes a comprehensive literature background on the HeIM and recent developments of secondary electron spectroscopy in charged particle microscopes, and thus may, in part, be seen as an extension of the literature review which follows this introduction (Chapter 2). In addition, novel results are presented which exemplify the potential and current limitations of secondary electron

spectroscopy. This publication was important for the research aims of this project, as it communicates the potential that secondary electron spectroscopy has for carbon based and natural materials—in both the HeIM and the SEM. The HeIM is a novel charged particle microscope with immense potential but still in need of microanalysis tools; and so the publication presents secondary electron spectroscopy as a potential solution to a growing community of material scientists.

The traditional results Chapter 5 titled "Instrument Parameterisation for Successful Spectral Imaging" explains the process of method development with regards to sample preparation, optimisation of spectral imaging and the handling of the data to obtain high quality data and results. It discusses in detail how optimal imaging and spectral parameters are obtained.

Chapter 6: "Sample Preparation for Successful Spectral Measurements", describes sample preparation protocols of spider silk for cryogenic and room temperature SEM imaging. The importance of thoughtful sample preparation and mitigation of contamination is demonstrated, and successful SE spectroscopy—also through the utilisation of MVA—is presented on a sectioned pigmented feather as a practical example.

The second publication "Revealing spider silk's 3D nanostructure through low temperature plasma etching and advanced low-voltage SEM" [32] focusses on spider silk as a material and contributes towards supplying the modelling community—and thus bottom-up approaches to polymer design—with more information as to where the order and disorder is spatially distributed in a well-studied spider silk. This publication further addresses the project aims by tentatively correlating observations made on the nanoscale to macroscale mechanical properties of the sample fibres investigated for the paper and by discussing the results in light of previously published work.

1.8   References

1.   *Industrial Strategy: building a britain fit for the future*. Ind. Strateg. (2017), https://www.gov.uk/government/publications/industrial-strategy-building-a-britain-fit-for-the-future (accessed August 12, 2019).

2.   R. Geyer, J.R. Jambeck and K.L. Law: *Production, use, and fate of all plastics ever made*. Sci. Adv. **3**, e1700782 (2017), doi:10.1126/sciadv.1700782.

3.   G.H. Michler: Electron microscopy of polymers, (Springer Science & Business Media, 2008).

4.   L.C.M. Lebreton, J. van der Zwet, J.-W. Damsteeg, B. Slat, A. Andrady and J. Reisser: *River plastic emissions to the world's oceans*. Nat. Commun. **8**, 15611 (2017), doi:10.1038/ncomms15611.

5.   J.R. Jambeck, R. Geyer, C. Wilcox, T.R. Siegler, M. Perryman, A. Andrady, R. Narayan and K.L. Law: *Plastic waste inputs from land into the ocean*. Science (80-.). **347**, 768–771 (2015).

6.   E. van Sebille, C. Wilcox, L. Lebreton, N. Maximenko, B.D. Hardesty, J.A. van Franeker, M. Eriksen, D. Siegel, F. Galgani and K.L. Law: *A global inventory of small floating plastic debris*. Environ. Res. Lett. **10**, 124006 (2015), doi:10.1088/1748-9326/10/12/124006.

7.   D. Voet: Biochemistry, Fourth edi, (Hoboken, NJ : John Wiley & Sons, 2011, Hoboken, NJ, 2011).

8.   T.E. Creighton: Proteins : structures and molecular properties, 2nd ed., (New York : Freeman, 1993, New York, 1993).

9.   A. Nova, S. Keten, N.M. Pugno, A. Redaelli and M.J. Buehler: *Molecular and nanostructural mechanisms of deformation, strength and toughness of spider silk fibrils*. Nano Lett. **10**, 2626–2634 (2010).

10.   F. Vollrath and D.P. Knight: *Liquid crystalline spinning of spider silk*. Nature **410**, 541–548 (2001).

11.   Q. Wang and H.C. Schniepp: *Nanofibrils as Building Blocks of Silk Fibers: Critical Review of the Experimental Evidence*. Jom (2019), doi:10.1007/s11837-019-03340-y.

12.   B. Huang, H. Babcock and X. Zhuang: *Breaking the diffraction barrier: super-resolution imaging of cells*. Cell **143**, 1047–1058 (2010).

13.   E. Rittweger, K.Y. Han, S.E. Irvine, C. Eggeling and S.W. Hell: *STED microscopy reveals crystal colour centres with nanometric resolution*. Nat. Photonics **3**, 144 (2009).

14.   D.C. Lin, E.K. Dimitriadis and F. Horkay: *Robust strategies for automated AFM force curve analysis—I. Non-adhesive indentation of soft, inhomogeneous materials*. J. Biomech. Eng. **129**, 430–440 (2007).

15.   D.C. Lin, E.K. Dimitriadis and F. Horkay: *Robust strategies for automated AFM force curve analysis—II: adhesion-influenced indentation of soft, elastic materials*. J. Biomech. Eng. **129**, 904–912 (2007).

16.   T.-Y. Lin, H. Masunaga, R. Sato, A.D. Malay, K. Toyooka, T. Hikima and K. Numata: *Liquid crystalline granules align in a hierarchical structure to produce spider dragline microfibrils*. Biomacromolecules **18**, 1350–1355 (2017).

17.   Y. Ding, G.-K. Xu and G.-F. Wang: *On the determination of elastic moduli of cells by AFM based indentation*. Sci. Rep. **7**, 45575 (2017).

18.   J. Notte, B. Ward, N. Economou, R. Hill, R. Percival, L. Farkas and S. McVey: *An introduction to the helium ion microscope*. AIP Conf. Proc. **931**, 489–496 (2007).

19.   H. Seiler: *Secondary electron emission in the scanning electron microscope*. J. Appl. Phys. **54**, R1–R18 (1983), doi:10.1063/1.332840.

20.   D. Joy: *Low Voltage SEM*. J. Microsc. **140**, 282 (1985), doi:10.1111/j.1365-2818.1985.tb02681.x.

21.   J.H. Butler, D.C. Joy, G.F. Bradley and S.J. Krause: *Low-voltage scanning electron microscopy of polymers*. Polymer (Guildf). **36**, 1781–1790 (1995).

22.   Q. Wan, K.J.K.J. Abrams, R.C.R.C. Masters, A.C.S.A. Talari, I.U.I.U. Rehman, F. Claeyssens, C. Holland and C. Rodenburg: *Mapping Nanostructural Variations in Silk by Secondary Electron Hyperspectral Imaging*. Adv. Mater. **29**, 1703510 (2017), doi:10.1002/adma.201703510.

23.   R.C. Masters, A.J. Pearson, T.S. Glen, F.-C. Sasam, L. Li, M. Dapor, A.M. Donald, D.G. Lidzey and C. Rodenburg: *Sub-nanometre resolution imaging of polymer-fullerene photovoltaic*

blends using energy-filtered scanning electron microscopy. Nat. Commun. **6**, (2015).

24.   R.C. Masters, N.A. Stehling, K.J. Abrams, V. Kumar, M. Azzolini, N.M. Pugno, M. Dapor, A. Huber, P. Schäfer, D.G. Lidzey and C. Rodenburg: *Mapping Polymer Molecular Order in the SEM with Secondary Electron Hyperspectral Imaging*. Adv. Sci. (2019).

25.   K.J. Abrams, Q. Wan, N.A. Stehling, C. Jiao, A.C.S. Talari, I. Rehman and C. Rodenburg: *Nanoscale Mapping of Semi-Crystalline Polypropylene*. Phys. Status Solidi **14**, 1700153 (2017).

26.   V. Kumar, W.L. Schmidt, G. Schileo, R.C. Masters, M. Wong-Stringer, D.C. Sinclair, I.M. Reaney, D. Lidzey and C. Rodenburg: *Nanoscale Mapping of Bromide Segregation on the Cross Sections of Complex Hybrid Perovskite Photovoltaic Films Using Secondary Electron Hyperspectral Imaging in a Scanning Electron Microscope*. ACS Omega **2**, 2126–2133 (2017).

27.   G.E. Moore: *Cramming more components onto integrated circuits*. (1965).

28.   M. Hilbert and P. López: *The world's technological capacity to store, communicate, and compute information*. Science (80-.). **332**, 60–65 (2011).

29.   K. Pearson: *LIII. On lines and planes of closest fit to systems of points in space*. London, Edinburgh, Dublin Philos. Mag. J. Sci. **2**, 559–572 (1901), doi:10.1080/14786440109462720.

30.   M.W. Berry, M. Browne, A.N. Langville, V.P. Pauca and R.J. Plemmons: *Algorithms and applications for approximate nonnegative matrix factorization*. Comput. Stat. Data Anal. **52**, 155–173 (2007).

31.   N. Stehling, R. Masters, Y. Zhou, R. O'Connell, C. Holland, H. Zhang and C. Rodenburg: *New perspectives on nano-engineering by secondary electron spectroscopy in the helium ion and scanning electron microscope*. MRS Commun. **8**, 226–240 (2018), doi:10.1557/mrc.2018.75.

32.   N.A. Stehling, K.J. Abrams, C. Holland and C. Rodenburg: *Revealing spider silk's 3D nanostructure through low temperature plasma etching and advanced low-voltage SEM*. Front. Mater. **5**, 84 (2018).

2 Literature Review

2.1 Organic Materials

The materials of interest for this project have in common that they are considered 'organic' compounds. The term 'organic molecules' describes materials and chemical compounds which firstly mostly consist of carbon and hydrogen atoms, and secondly exhibit molecular structures with covalent bonds being prevalent over ionic and metallic type bonding [1]. The majority of materials produced by nature can be considered to be organic, although inorganic natural structures—such as teeth and bone—are also of importance. The molecular build–up of organic materials directly relates to their macroscale properties: they are mostly insulating due to the electronic structure being best represented by discreet molecular orbital energy levels rather than the conducting energy bands present in metals [2]. Furthermore, due to the prevalence of carbon, hydrogen, oxygen and nitrogen atoms, organic materials are low atomic number (z) compounds. This has implications for the analysis of materials using electrons and X–rays, which will be discussed in detail in section 2.5: Electron Microscopy and its Role for Polymer Materials.

Organic materials gain their properties not solely from the atoms which they consist of, but by the exact arrangement of this rather limited variety of atoms in a covalently bound molecule. For example, different combinations of carbon, hydrogen, oxygen, nitrogen and phosphorous atoms may make up the blueprint of life in deoxyribonucleic acid (DNA) or may make up the powerful synthetic explosive trinitrotoluol (TNT). This justifies the vast toolbox of analytical methods which exist to characterise the molecular structure of organic compounds, further discussed in section 2.4: Silk Study and Characterisation. However, in the context of materials the complexity of both

synthetic and natural materials extends far beyond the molecular scale to larger length scales. For example, a protein may arrange into a cluster of proteins to form haemoglobin, or it may be extruded from the body as a nano–structured protein to make a microscale object such as a hair or a thread of silk. Nano– and microscale structuring is vastly important for macroscale properties, and thus it is no coincidence that natural structural compounds exhibit structure–property relationships down to the smallest length scales. It is thought that these multi–scale structures interact with one–another favourably to create a hierarchical structure, although models to explain exactly how these structures interact across length–scales are still difficult to parameterise and compute [3].

2.2   Nature's Material Building Blocks: Carbohydrates, Proteins and Minerals

Future plans of moving towards a sustainable, circular economy have bought natural materials into the spotlight as solutions to replace unsustainable petrochemical polymers and plastics. It has been suggested that today's dominance of petrochemical materials is not due to the inferiority of natural, biomass sourced materials, but instead is the result of heavy investment into synthetic plastics throughout the last century [4]. In recent years, attention has shifted back to natural materials for sustainable and high–performance materials solutions.

Natural structural materials
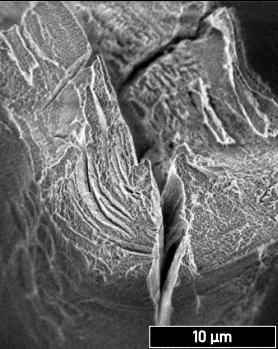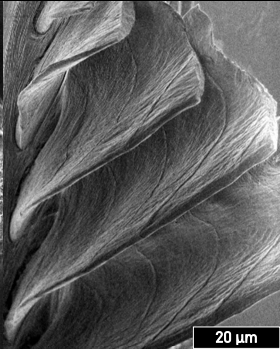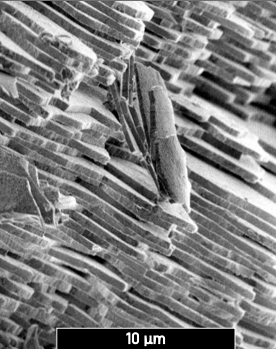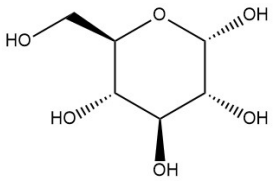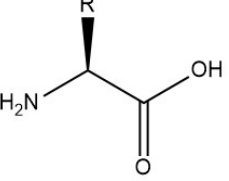
	Cellulosic	Proteinaceous	Inorganic Mineral
Macroscale structure			
Microscale structure	10 µm	20 µm	10 µm
Building block	Monosaccharide (e.g. glucose)	Amino acid (e.g. glycine for R=H)	CaCO$_3$ Mineral (e.g. aragonite)

Figure 2.1: Common natural structural materials from the macro– to the atomic scale. SEM images and shell from this work, depiction of tree adapted (cropped, isolated and histogram adjusted) from Jon Feinstein (https://www.flickr.com/people/jonfeinstein/) under a CC BY 2.0 licence (https://creativecommons.org/licenses/by/2.0/), depiction of feather adapted (rotated, cropped and histogram adjusted) from Pepetka (https://www.flickr.com/people/pepetka/) under a CC BY–NC 2.0 licence (https://creativecommons.org/licenses/by–nc/2.0/).

In the evolution of higher organisms, nature repeatedly solved the problem of producing materials which are suited for withstanding mechanical stress. These materials are often evolved specifically for the mode of mechanical stress and are furthermore

resource efficient in their production—specifically natural structural materials are often made up of the same building blocks which are key players in molecular scale processes of organisms and are thus already available in the organism. For example, glucose is a vital energy unit to plants as well as other organisms, but also serves as a building block (monomer) for remarkably strong macroscale cellulose structures such as plant fibres (See **Figure 2.1**). A common theme in natural materials is therefore that they are made up of readily available raw materials, and that it is not the material building block which governs their properties but their hierarchical structural arrangement across multiple length scales [5]. The most commonly encountered natural structural materials may be classified into cellulosic, proteinaceous or inorganic materials such as minerals, although their micro– and nanoscale structures exhibit an enormous diversity—as seen in **Figure 2.1**—which may serve as inspiration for scientists and materials manufacturers.

2.3   Spider Silk as a Remarkable Structural Biopolymer

A natural structural material of particular interest to this project is spider silk, as the considerable research effort to link its nanoscale structures and macroscale properties has yet to produce conclusive hypotheses and mechanical models.

Silk holds its own place amongst the natural structural biopolymers by the distinction that it is spun, and not grown. Instead of being slowly produced and added to an existing structure, it is spun from a protein solution and turns into the solid silk ad–hoc and almost instantly [6]. Silk is not uncommon in invertebrates, with silk production being present in the lives of some bees, mites, caterpillars and spiders to name but a few. The biological class *Arachnida* comprises of millions of spider species which have established themselves in varied eco–systems all around the earth and is particularly well known for its use of silk in all aspects of life.

In innovating new, sustainable and high-performance materials, one may use nature as a source of material feedstock, or one may abstract key features into blueprints for synthetic materials. An example for the first approach is the production of materials from nature for bulk applications, such as cellulose for paper and caterpillar silk for textiles [4]. Farming spider silk, however, is financially unviable due to two main reasons [7]. Firstly, spiders are cannibals and farming them would be space-intensive and logistically complicated as they need to be given room. Secondly, while caterpillar silk cocoons are simply unravelled after the caterpillars pupate, spider silk would have to be won periodically from a web or directly from the live spider, making it a practical challenge. Therefore, to obtain spider silk as a biomass material precursor, genetic engineering of other organisms has been performed. Genes giving rise to the expression of spider silk proteins (spidroins) have been sequenced, and by the use of genetic modification silk protein can be expressed and isolated in organisms such as bacteria and goats [8,9]. This resulting protein solution is called non-native feedstock or recombinant spider silk. The overall financial and time investment is large, in part also due to the necessity of purification steps, and the resulting mechanical properties of the spun fibres are inferior to natural spider silk, suggesting that the spinning process and the nanoscale structures significantly contribute to the properties of native spider silk [8-10]. Nonetheless, recombinant spider silk is widely used in investigations into possible commercial spinning solutions for protein solutions to spin silk at a larger scale [9,11-13].
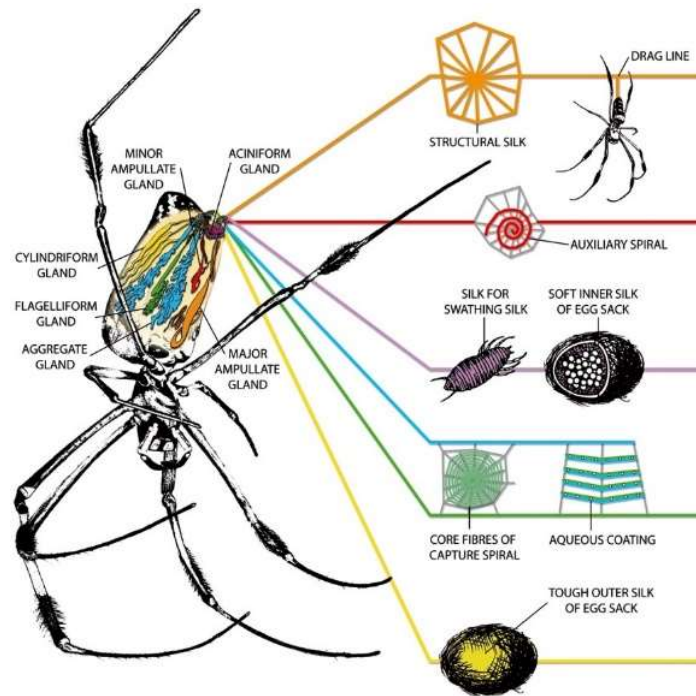
Figure 2.2: Schematic depicting the different silk glands of a female *Nephila* spider, the different resulting silks and their uses. Reproduced by permission from Chris Holland, Copyright Vollrath and Holland 2005.

Within the spider, silk is stored as a viscous liquid in highly specialised glands (shown in **Figure 2.2**), and solidifies when it is drawn out of the spinnerets into the environment. The spinning process has attracted a lot of interest, with scientists investigating the chemical balance, the shear forces and the flow dynamics present in the spinning duct to yield the remarkable structural and mechanical properties of spider silk [6,14–20]. Although this project focusses on the ready–spun solid fibre, investigations into the transition from a protein gel into a solid have yielded some relevant hypotheses as to how the nanostructures form: bulk measurements of the protein gel would suggest that the proteins are assembled as random coils [21,22]. However a closer look at the amino acid sequence and the protein gel under AFM and TEM supports the idea that about 100-300 nm sized hierarchical structures self–assemble in the protein dope before it is spun [23–25]. It is suggested that shear forces elongate the structural domains of these

nano–clusters and may serve as seeds for the further shear–induced solidification and structural transformation of the gel into a nanostructured solid [23,25,26]. Tentative links have been made between the nano–clusters present in the gel and the nanostructures within a solid fibre [25]. However, such associations will be difficult to make with confidence, until a consensus has been established for the exact form and spatial distribution of such nanostructures in the solid fibre.

In the life of a spider, different silks are used in a range of applications such as building egg–sacs for reproduction, intra–species communication and prey–capture (see **Figure 2.2**). Thus, the material properties of the different silks are specialised according to their respective application [27,28]. The silk of orb–weaving spiders has attracted the attention of the materials science community in particular, due to its remarkable mechanical properties: the orb–web is an extremely light–weight structure which supports the weight of the spider and also effectively withstands insect impact.

The main component of spider silk is a group of proteins called spidroins and it is widely accepted that these proteins dictate the structure within the silk fibres. As proteins, spidroins naturally introduce a hierarchical structure from the nanometre to the micron scale. In the early 1990s Xu et al. used gene sequencing methods to reveal the DNA blueprint of *Nephila clavipes* major ampullate (dragline silk) spidroin and discovered that highly conserved poly–alanine regions form β–sheet crystals responsible for the tensile strength, while the glycine–rich repeat units are responsible for the elasticity of the solid fibre [29–31]. They also discovered two distinct *N. clavipes* dragline spidroins, which were initially called spidroin 1 and spidroin 2 (now commonly abbreviated to MaSp1 and MaSp2) [30,31]. The most remarkable difference between the primary sequence of MaSp1 and MaSp2 is the proline content. Proline residues are believed to introduce disorder into spider silk protein structure, increasing the domains accessible

to water and causing the spider silk to supercontract when in contact with water [28,32,33].

It is generally accepted that poly–alanine primary sequences lead to formation of β-sheet nanocrystals within the core, which in turn arrange into larger structures which are thought to contribute to the tensile strength of the fibres, such as nano–fibrils of 20–150 nm diameter, [34,35]. These nano–fibrils have so far been suggested to exist as diffuse but aligned structures in AFM studies of the fibre surface [36], and are thought to give rise to the globular appearance of tensile cross–sections [37]. The problem with these studies is that they only vaguely resolve a small region of the complex structure within a dragline thread. In this case the AFM study probed the skin of the fibre, which may not be representative of the core, and the cross–sectional SEM imaging was performed after sputter coating, potentially obscuring features of the fracture surface. A recent review of experimental findings on the question of nanofibrils concluded that while clear resolution of nano–fibrillar structures has been achieved for *Bombyx mori* silkworm silk [38], direct observation of the nano–fibrils or even the nanoscale β–sheet crystals remains elusive for spider dragline silk [39]. The location, distribution, and volume fraction of such nanofibrils has not been sufficiently determined to date.

Besides the hierarchy within the silk which is introduced by the spidroin proteins, there are other layers to the structure such as multiple outer layers with functionalities including carrying pheromones, microbial protection and maintaining plasticity [40]. Li et al. first reported the observation of two distinct phases within the core using atomic force microscopy (AFM) on *Nephila clavipes* dragline silk and suggested that this may indicate an uneven distribution of the different spidroins throughout the cross–section [34]. This claim has since been further validated in work by Sponner et al., who found that the outer core contains less MaSp2 and thus less order–disrupting proline, and

Knight et al., who found an increased β–sheet crystal content in the outer core in the dragline silk of the closely related *Nephila edulis* spider [16,40].
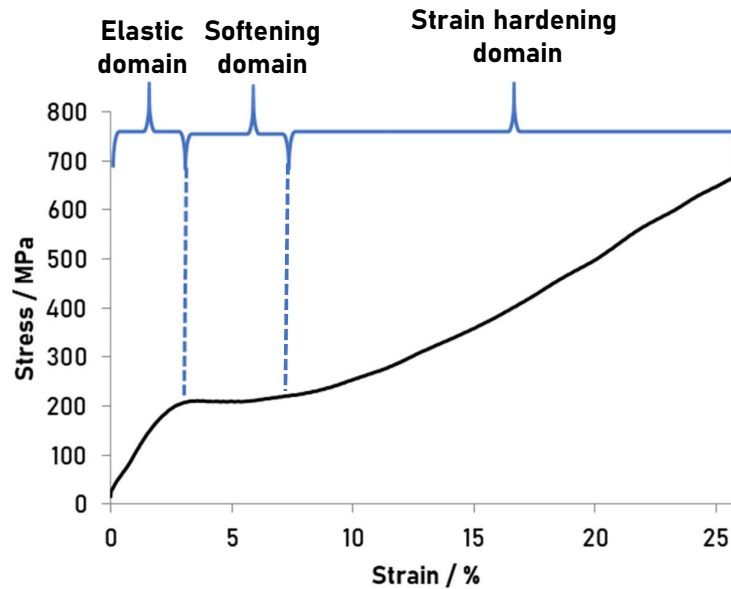
Figure 2.3: Schematic stress strain behaviour of spider silk dragline thread based on results from this work, collected as described in section 3.1.2

While the discussion about the situation and properties of the internal nanostructures is ongoing, the bulk mechanical properties of dragline spider silk are well characterised. The typical tensile behaviour of spider dragline silk is shown in **Figure 2.3**: the fibre initially exhibits an elastic zone, from which the elastic modulus is calculated. The stress–strain curve proceeds through a yield point before exhibiting strain–hardening behaviour. Numerous modelling studies have used structural models of spider silk dragline to relate the tensile characteristics to the interactions between the different structural domains [41–43]. In a 2016 review, Su and Buehler rationalise the tensile behaviour with respect to the nano–structure as follows [44]: in the initial elastic zone the less ordered (semi–amorphous) phases of the fibre stretch reversibly, until at the yield point hydrogen bonds within secondary structures associated with lower order domains dissociate irreversibly. In the following plateau, these less– ordered structures are extended along the fibre axis, continuously unravelling their

secondary structures. Simultaneously, these stretched semi–amorphous domains are now free to form new hydrogen bonded β–strands stimulated by the tensile force along the fibre. In the strain–hardening domain, the disordered phases reach their limit of extensibility and the force is transferred to the strongly hydrogen bonded β–sheet crystals. Failure occurs when the tensile forces are strong enough to pull the hydrogen bonded β–sheets apart. While this description of nano–mechanics is consistent with spectroscopic analysis [41,42,45], the evolution of the different structures throughout tensile strain is yet to be directly observed.
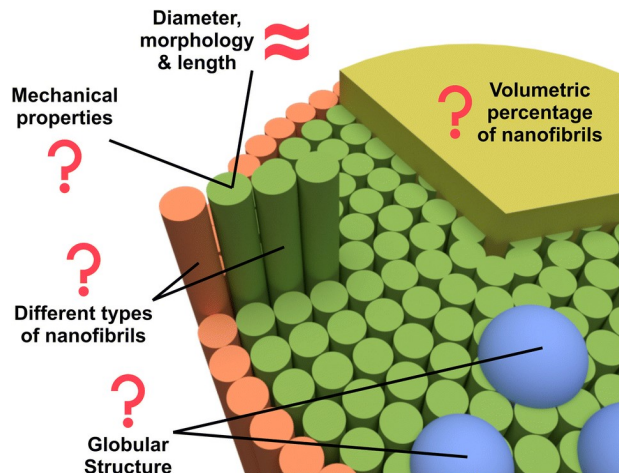
Figure 2.4: Schematic depiction of the uncertainty within structural models for spider silk. Reprinted by permission from Springer Nature Customer Service Centre GmbH: Springer Nature, JOM Journal of the Minerals, Metals and Materials Society [39]

The role of the different multiscale structures present in spider silk upon deformation may be explained through a mechanical model. The existing models and their limitations have recently been reviewed [3] and are discussed in detail in Chapter 7 [46]. Most mechanical models of spider silk deformation only offer an insight into structures of a certain size and have not been extended across length scales to model the bigger picture—not least because structural information is still lacking to parameterise such models (see **Figure 2.4**). These parameters include the mechanical properties, size, shape and spatial distribution of different multiscale structures.

In understanding the evolution of structures through mechanical deformation, one way of investigating spider silks with different strain histories is by obtaining force reeled samples with different reeling speeds. It has been shown that with increasing reeling speeds the modulus increases while the extensibility decreases, resulting in a maximum toughness at about 2 mm s^{-1} [47]. This is in line with X–ray diffraction studies showing higher β–sheet crystal content and alignment of the domains along the fibre axis for higher reeling speeds [48].

Reeling speed is not the only parameter with a significant impact on the fibre properties. As with most biological samples, the natural variability of the material needs to be taken into account when trying to compare values between studies as the environmental temperature and humidity, the species and the constitution of the spider have been found to influence mechanical properties as well [47,49,50]. This must be kept in mind for good experimental design using spider silk and when comparing results from different researchers or even samples from the same spider.

2.4   Silk Study and Characterisation

Spider silk is a widely studied material. Spectroscopic structural analysis tools have been reviewed in detail recently [51], and a general review of spider silk literature relevant to this project can be found in Chapter 7. This review will put an emphasis on spider silk's thermal analysis, as it is relevant to the sample preparation methods employed in this project, but will also look more in–depth at spatially resolved techniques, under the premise that spatially resolved information will bring forth the compositional maps required to piece together all other spatially averaged information which has been determined by different methods in the past.

2.4.1   Thermal Analysis

Through the use of thermal analysis techniques such as dynamic mechanical analysis (DMA) and differential scanning calorimetry (DSC) it has been found that spider silk exhibits remarkable mechanical properties at temperatures significantly above and below the expected performance window required in nature, which at a push may be about -20 to 60 °C, with mechanical properties mostly maintained in a range of -66 to 100 °C [52]. Yang et al. point out that the toughness of silk fibres increases significantly and continuously below 0 to at least -66 °C [53], and also maintains its high strength down to liquid nitrogen temperatures, where plastic deformation still readily occurs [54]. Tensile properties slowly decrease above 60 °C with increasing temperature, with Guess and Viney suggesting the glass transition temperature lies at 160 °C for *Nephila clavipes* silk which has been subject to drying for at least 24 h [52] and Guan et al. measured the glass transition at 194 °C for *Nephila edulis* silk [55]. Plaza et al. establish the role of humidity as well as temperature in the transition of the silk's mechanical response from a 'glassy' to a rubbery material: they suggest that both increased temperature and increased humidity serve to increase mobility of the molecular chains present in spider silk and contribute to a rather abrupt transition to a rubbery mechanical response [56]. It should be noted that the terms 'glassy' and 'rubbery' are established terms in the field of synthetic thermoplastic polymers and must be applied to a complex multi-phase mechanical response such as that of spider silk with care. When referring to spider silk's mechanical response at room temperature as 'glassy', this is in reference to the pre-yield behaviour in which hydrogen bonds keep the biopolymer chains in place. Irrecoverable deformation may still readily occur if the material is stressed beyond the yield point.

These thermal methods are all performed on the bulk fibre, however they allow some conclusions about the presence and role of the different structure in the mechanical

response: the temperature–dependent mechanical behaviour highlights the important

role of water with the less–ordered domains within the spider silk [52,56]. The absolute

thermally induced mechanical failure of *Nephila* dragline silk has been found to occur

above 350 ℃ [53], where the ordered crystallites degrade, as is evident from thermal

X–ray studies [57]. While these thermal studies do not contribute to mapping the

structural nanoscale components present within spider silk, they do have implications

for sample preparation and manipulation strategies, as will be discussed in Chapter 6.

2.4.2   Spatially Resolved Techniques

2.4.2.1   Optical spectroscopy

Spider silk has been analysed in depth using Raman and infrared spectroscopy, with

specific wavelengths giving answers about the crystallinity and the mechanical history

of the bulk fibre [58–65]. With increased speed of spectral acquisition Raman mapping

and correlative spectroscopy have become more powerful. For example, Raman

mapping can be integrated into SEMs to obtain microstructural and local chemical

information simultaneously, with advantages over EDX maps for low z materials [66,67].

Theoretically, SEM-Raman can achieve sub-micron lateral resolution and 1.5 µm depth

resolution [66]. However, spider silk is transparent over a significant portion of the IR-

visible-UV window of the electromagnetic spectrum [68], and exhibits complex

refraction behaviour [69]. Thus, incident light rays would travel and scatter far into the

material and delocalise emission information. Perhaps that is why—to the author's

knowledge—there are no published Raman or IR spectroscopy maps of spider silk,

whether in conjunction with SEM or not.

2.4.2.2   AFM

AFM has the big advantage over electron microscopy that it may be performed in

ambient, or environmentally controlled conditions [70]. This has made it especially

suitable for investigating localised changes in modulus when immersing a fibre surface and an axial cross–section in water [71,72]. The results show that the increased modulus of the outer–core in *Nephila* dragline silk, which was first reported in 1994 [34], decreases significantly when exposed to water or humidity, to match the rubbery mechanical response of the inner–core [72]. AFM is also capable of resolving the compositional difference between the outer–core and the outermost skin on *Nephila* dragline silk [40,72]. In an attempt to characterise smaller–scale structures Du et al. have imaged 40—80 nm structural segments on the surface of *Nephila pilipes* silk [36]. However, it is well established that *Nephila* dragline silk has an outermost lipid and not proteinaceous layer [40], and it is doubtful whether imaging the skin using AFM can offer insights into the structural make–up of the fibre as a whole.

To look at internal structures present inside the fibre, one may employ sectioning techniques and different embedding matrices have been trialled, such as paraffin wax, epoxy resins or acrylic resins [34,40,72]. The overall chemical alteration of the spider silk in the embedding process is both poorly understood and insufficiently validated with protocols often involving other steps, such as dipping the sectioned sample in an ethanol solution to remove the wax. Furthermore, the question remains whether room–temperature sectioning causes plastic deformation of the observed section, meaning that in effect, the sample imaged has potentially been altered chemically and mechanically. Li et al. comment on the fact that they observe no identifiable knife artefacts from their microtome, although they are present on the epoxy matrix [34], suggesting that the silk may have plastically deformed in response to the knife passing over resulting in an unknown degree of material recovery to its original state. Recently, Lin et al. have coupled high resolution environmentally controlled AFM with sectioning techniques, to image a longitudinal section of *Nephila clavata* dragline silk [25]. Within the section, they observe 'granules' approximately 133 nm in size, which align along the

fibre. While the study demonstrates the qualities of AFM in its environmental control and resolving power, the sample preparation implications mean that the possibility of preparation artefacts cannot be excluded.

The challenge of cross–sectional sample preparation complicates the interpretation of hitherto published AFM images significantly. Nonetheless, the possibility of imaging in ambient conditions remains an advantage over measurements which must be performed in vacuum.

2.4.2.3   Electron Microscopy for Spider Silk

The problem of obtaining sections for imaging also applies to the field of electron microscopy of spider silk. To add to sample preparation complications, sufficient contrast for transmission electron microscopy (TEM) studies of embedded and sectioned spider silk use heavy metal stains such as osmium tetroxide and lead citrate [40,73–75], again with no consideration of whether the sample preparation method interferes with the measurement. Despite the effort involved in the preparation of these sections for TEM studies, some of the images obtained in the respective studies have a spatial resolution which would equally be achievable in modern scanning electron microscopy systems at less effort, perhaps due to dose restrictions. TEM diffraction experiments and electron energy loss spectroscopy was performed on *Nephila* dragline silk in the mid-1990s, again on chemically dehydrated and embedded silk [76]. The results for the crystallite content and size are in significant disagreement with other bulk spectroscopic measurements [77], perhaps due to the exposure of the fibre to solvents. which is known to increase crystallinity beyond the natural state [78].

Scanning electron microscopy (SEM) has the advantage over AFM and TEM that the sample does not have to be planar or thin to perform imaging, making it possible to omit the embedding and sectioning preparation steps. For example, Poza et al. have investigated the tensile fractures of *Argiope trifasciata* silk, and were able to see nano–

morphological differences between the skin and the core in the fractured cross–section, with smooth and rough, globular morphologies respectively [37]. Cross–sections for SEM observation may also be obtained by cryo–fracture [53], however the plasticity of spider silk—discussed above—makes it unclear how much structural transformation has taken place before the fracture is imaged.

Despite the proven effectiveness of low–voltage SEM, it is still common practice to coat the samples in gold before SEM observation. As the structures of most interest exist on the nanoscale, even a nanometre–thick gold coating may interfere with the size measurement of structures found within the silk. Low–voltage SEM observation of uncoated spider silk has been shown to yield excellent image quality [46,79], and furthermore retains access to the sample surface for microanalysis tools, making it a promising technique in electron microscopic observation of spider silk.

2.4.3   Summary of Findings

Despite the large body of analytic and spectroscopic work performed on spider silk, the results are difficult to consolidate into a single model of what spider silk nanostructure looks like. The large sample of spider species which have been investigated complicate the matter further. In a recent review, Wang and Schniepp have revisited the question of nanofibrils in spider silk and have compared spatially resolved results from different techniques and species [39]. For *Nephila* spider silks, statements about the arrangement of nanofibrils (fibrils or segmented globules) and their size diverge wildly (3-300 nm), as illustrated in **Figure 2.5**. The misalignment of results from different techniques suggest that a correlative approach may be more successful, where nanostructure and compositional information can be extracted in one experiment.
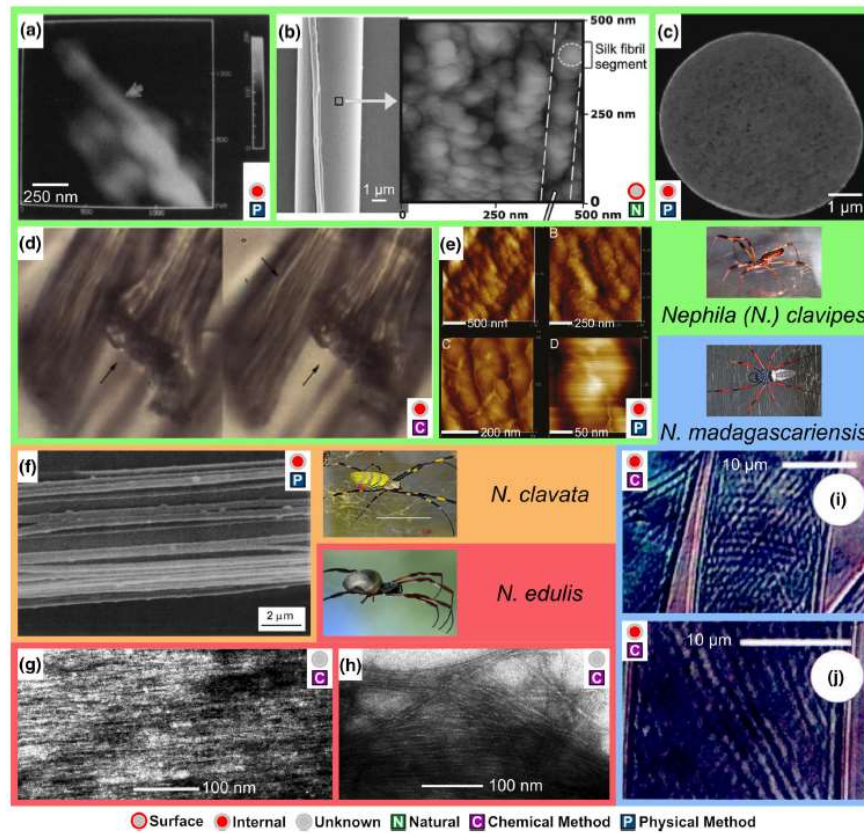
Figure 2.5: Spatially resolved observations of *Nephila* spider silk and its internal nanostructure in literature. Reprinted by permission from Springer Nature Customer Service Centre GmbH: Springer Nature, JOM Journal of the Minerals, Metals and Materials Society [39]

2.5   Electron Microscopy and its Role for Polymer Materials

Electron microscopes (EMs) were pioneered in by Ruska and Knoll in 1931 and gradually evolved to be incredibly versatile instruments [80,81]. The EM field may be parted into SEM and TEM and while both are able to measure a multitude of signals resulting from electron–matter interactions, the two imaging modes are traditionally regarded as separate disciplines due to separate instrumental design, sample preparation implications and information to be gained. More recently, scanning transmission electron microscopy (STEM) has provided a step change in the capabilities of electron microscopy, with many transmission experiments now being performed in SEMs, and scanning coils becoming a feature within traditional TEM designs more frequently [82].

Transmission mode electron imaging requires for samples to be 'electron–thin' to reach the transmission detector on the other side. The requirement for sample thicknesses of hundreds of nanometres and below means that samples may have to be extensively and skilfully prepared. Nonetheless well–established fixating, staining and sectioning protocols exist to enable the TEM observation of biological materials, for example the imaging of snapshots of fundamental biological processes [83,84].

SEMs are generally easier to operate and are thus more widely accessible to non-expert electron microscopists in search of a microstructure and analysis tool. In the regular imaging mode, only the surface is probed, so samples of varying shapes and sizes may be observed without the need for time intensive preparation. Many modern SEMs allow the low voltage observation of samples, granting access to the analysis of beam sensitive materials in a non–destructive manner. Recent technological advances have made the SEM, in particular low voltage SEM, very attractive to novel work on materials which were previously difficult to image at high resolution [85–87]. In line with the project focus, the following section will focus on the general principles and technological advances in the low voltage operation of SEMs, which is especially suited

for the observation and analysis of polymers and other beam–sensitive insulating

material of interest to this project.
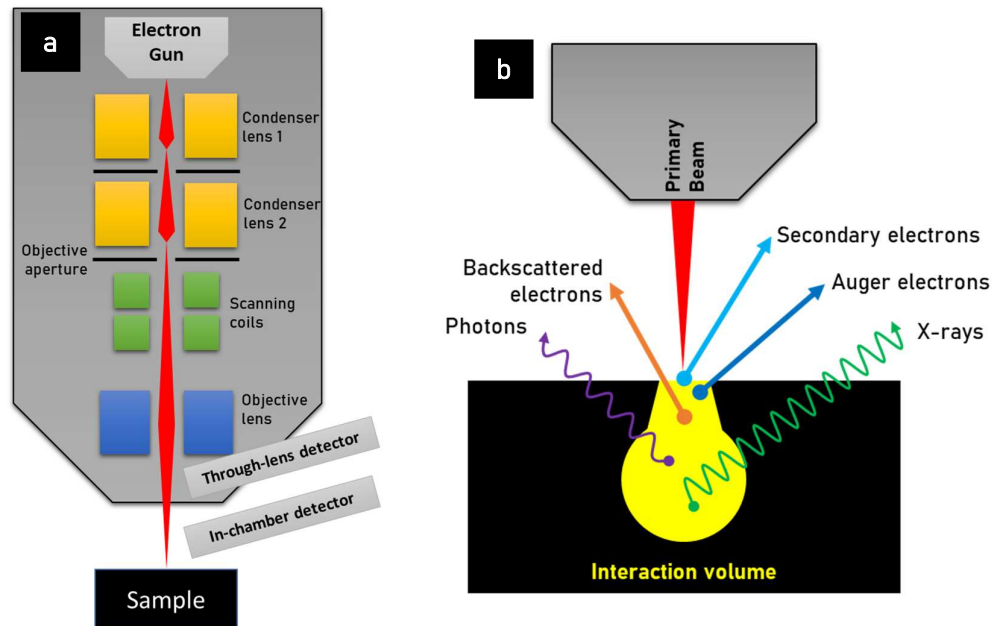
Figure 2.6: a) Schematic of a scanning electron microscope column and situation of secondary electron detectors b) Signals arising from electron beam impingement of a sample in the scanning electron microscope

2.5.1   Basics

The basic principle of electron microscopy relies on the interactions of electrons—in

the form of an electron beam—with the sample [1]. Electron–matter interactions are

complex, and thus the many different events which can occur within the interaction

volume when electrons impinge the sample yield different signals, which are

summarised schematically in **Figure 2.6 b**. There are multiple detection systems

available to measure the emerging signals and so many different experiments may be

performed in EMs. As the different signals are a result of a cascade of interactions

within the interaction volume, the spatial resolution of an emitted signal depends not

only on the probe size of the electron beam but crucially on the size of the interaction

volume. The commonly measured X–ray and backscattered electron (BSE) signals are

stronger at higher accelerating voltages, but at the cost of a lower spatial resolution. In contrast, the secondary electron signal becomes both stronger and more spatially localised with decreasing accelerating voltages, making it the favourable signal for LV–SEM experiments. For the sake of the following discussion LV–SEM will be defined by having primary beam energies from 300 eV up to 5 keV, although 2 keV is the maximum used in this project.

2.5.2   Technical and Practical Consideration for Low Voltage SEM

The technological advances required to transition from high accelerating voltage investigation of conducting materials to low–voltage SEM experiments were driven by the semiconductor industry, which required ways of observing their poorly conducting samples without the need for a conductive coating [88]. The new developments were quickly taken on by scientists investigating polymers and biological materials when it was found that the nanometre resolution of a low–voltage capable SEM could rival TEM studies which required more extensive expertise and sample preparation [1,88,89].

The key LV–SEM enabling technologies include the cold field emission gun, which boasts higher emission currents, lower electron energy spread and a more spatially focussed emission compared to older electron gun designs [1,87]. Other technological advances benefitting low voltage applications were improved vacuum systems, electron optics and extended user control of critical parameters such as accelerating voltage and beam current [1,86,90]. In the SEM, the electron beam is directed onto a focussed spot which is scanned across the sample surface to generate the image— pixel by pixel. The importance of controlling the scanning pattern when imaging insulators was recognised early on, with minimal dwell times (i.e. how long the beam stays on one spot) being favourable to avoid unwanted beam–sample interactions such as charging [88]. In regular TEM, where the primary beam is projected onto an area rather than focussed on a spot, such scanning parameters do not exist, which is

perhaps why they have not received as much attention as the scientific discussions about current density and beam dose [91]. Nonetheless scanning patterns are of great importance to other EM fields, such as scanning transmission electron microscopy (STEM) [92] and electron and ion beam nanoengineering [93], so that control over different scanning parameters and protocols is now more widely available to users.

Many publications have addressed sample surface charging, sample damage and surface contamination build–up, and even today these must be carefully considered by LV–SEM operators.

To manage charge, there are established strategies which help the operator in finding the optimum imaging conditions. In the case of insulators, only a fraction of the charge injected into the sample may be neutralised to ground and so surface charge can build up, resulting in distorted images and measurements. To determine the overall charge flux at the sample surface, the emitted charge (e.g. SEs) must also be considered. Due to the smaller interaction volume at lower accelerating voltages, more secondary electrons can make their way back to the surface and escape into vacuum and so the secondary electron emission yield is increased in the low voltage SEM range compared to higher accelerating voltages. It may also be the case that at certain accelerating voltages with high SE yields, more negative charge may be emitted in the form of SEs than is injected by the primary beam [87,88]. The overall change in charge flux with accelerating voltage leads to the switch between positive and negative charging domains, but crucially also to the crossover energies E_1 and E_2, where the injected and emitted charges are in balance. This is illustrated schematically in **Figure 2.7**. E_1 is typically at voltages below the regular SEM operating range, but E_2 is within range and well defined for many polymers (e.g. E_2 = 1.2 keV for Nylon–6) [88].
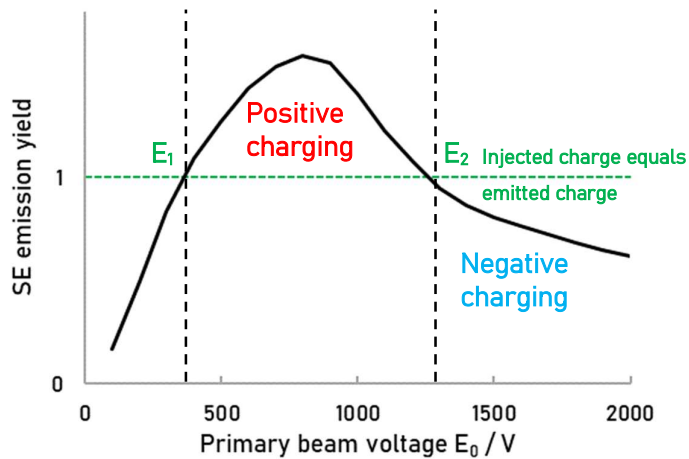
Figure 2.7: Schematic graph of the secondary electron yield as a function of the primary beam voltage E_0 and the resulting charging domains and crossover energies E_1 and E_2.

Setting the accelerating voltage to E_2 greatly helps with minimising surface charge and acquiring high quality images of uncoated samples. However as many experts in the field have pointed out the charge balance is dynamic and highly dependent on complex parameters such as the beam dwell time, current density, magnification and topography of the sample [90,94–97]. In general this means that not just the accelerating voltage but also other user–controlled parameters such as magnification, current, sample tilt and dwell time should be optimised by systematic empirical observation of the extent of charging at all times [87]. These decade old workflows are still generally valid today, but do not consider modern capabilities of SEMs and would benefit from receiving an update.

Besides the challenge of charging, sample damage was initially expected to be considerably worse in the SEM investigation of soft materials compared to their TEM observation, as in TEM a much smaller fraction of electrons interacts with the sample as they travel right through the electron–thin sample. Significant damage has indeed been observed in LV–SEM experiments due to electron impact and resulting cascade of interactions leading to damaging effects such as molecular bond cleavage, but

overwhelmingly it has been established that reducing the accelerating voltage significantly reduces the extent of any observable damage in the SEM compared to the TEM [87,88,91]. It has been suggested that the apparent stability of uncoated organic samples under low accelerating voltages is due to the small size of the interaction volume reducing the overall spatial extent of damage, but it has also been pointed out that the overall power injected into the sample is less at lower primary beam energy [89,98]. Additionally, the high yield of secondary electrons means that lower beam currents can be used in modern systems with high detection efficiencies. While the hundreds of keVs necessary for TEM observation remain destructive and a limitation for the TEM observation of organic materials, it is widely accepted today that the same samples can be very stable on the timescales required for LV–SEM observations.

As the escape depth of SEs decreases with primary beam voltage (E_0), LV–SEM measurements are a reflection of the top few nanometres of a sample only. This means that surface effects such as adsorbed molecules or contamination layers gain importance at lower E_0 and as a consequence, contamination and surface effects need to be managed and mitigated. Surface modifications have a drastic effect on image contrast [99], which is both a curse and a blessing—these contrast changes may be tracked—especially with through–lens detection systems [100]—and can guide the adjustment of imaging parameters to mitigate the extent of any detrimental effects on the measurement.

2.5.3   Electron Spectroscopy as a microanalysis tool

Electrons may be differentiated by their energy to yield electron energy spectra which respond to different electron-matter processes, and thus sample composition and structure.

2.5.3.1   Electron Energy Loss Spectroscopy

In electron energy loss spectroscopy (EELS) the beam energies are characterised after the beam has passed through the sample in a transmission experiment. Through inelastic scattering primary beam electrons have lost energy to the sample, which manifests in the spectrum as an energy loss compared to the primary beam energy. EELS is an immensely powerful tool due to its high energy resolution and sensitive response to sample structure and composition. Recently the energy resolution has become high enough (40 meV and below) to observe vibrational spectra amongst the primary beam induced electronic transitions also for biological materials, albeit with careful monitoring of radiation damage [101–103]. For EELS studies of beam-sensitive materials, a scanned primary beam is commonly used to control dose and provide local EELS spectra, and primary beam energies are reduced down to 60 keV, which is still a lot higher than even high-energy SEM experiments.

2.5.3.2   Secondary Electron Spectroscopy in the SEM

Secondary electron spectroscopy is an old idea but has benefitted from much less technological advancement compared to EELS. In terms of electron-matter interactions it may be considered complementary to EELS, as it measures the electrons resultant of inelastic scattering processes, however EELS and secondary electron spectroscopy are currently performed with very different instrumental configurations. This may also be a justification for further investment into secondary electron spectroscopy as a technique, as it may be a beneficial analysis tool for materials which cannot withstand beam energies of 60 keV. Furthermore, the small escape depth and thus high depth resolution of secondary electrons may provide an advantage over EELS for layered or 3D nanostructured materials, as transmission EELS will provide an average over the sample thickness.

The origins and developments of secondary electron spectroscopy in the HeIM and SEM are reviewed in detail in Chapter 4, as part of the heading "In–situ SE spectroscopy (SES): experimental considerations". In the following some additional aspects and the most recent developments in the SEM are explained and discussed.

Besides utilising the secondary electron signal for spectral acquisition and imaging, it should be noted that there are analogous developments concerning back–scattered electron (BSE) energy analysers with the aim to select energies in which nanostructural and compositional contrast dominates and topographical information is excluded [104–108]. Notably these techniques are applicable to nanostructural differences in polymers and plant fibres, although due to the low BSE yield at low voltage SE energy–selective techniques have a clear advantage [87]. The low BSE yield is especially relevant for beam–sensitive materials, as signifies the requirement for higher electron beam exposures to obtain the same signal to noise ratio as the corresponding SE image. Furthermore, there is compelling work which shows that secondary electron hyperspectral imaging (SEHI) has the capability to reveal true material contrast and supress topography similar to regular BSE imaging, but with higher resolution capabilities [109].

With a renewed interest in the emission behaviour of secondary electrons in scanning electron microscopes, and with modelling approaches on the rise, a number of studies have simulated the generation of secondary electrons in matter. The method of choice is commonly a Monte Carlo simulation, where each event is assigned a statistical probability—derived from experimental data and first principles—and many events are simulated until a statistically relevant representation of the overall outcome is reached. Using this approach in conjunction with experimental data on a conductive polymer it has been shown that the secondary electron energy spectrum is sensitive to the electron affinity of the material, and also the local crystallinity [110,111]. Besides

polymers, there has been significant progress in the analysis of carbon species: The joint approach of Monte Carlo modelling and experimental studies has yielded the characteristic SE spectra of specific sp^2–hybridised, sp^3–hybridised or hydrocarbon contamination moieties [112,113]. This is an immensely important result as it means contamination and electron beam induced deposition can be detected and controlled. Further modelling approaches have made encouraging progress towards gaining a better understanding of the time dependence of secondary electron emission [114] and perhaps more importantly for uncoated insulating samples, the time dependence of the charge dynamics of insulators [115]. These studies have direct implications on the way images and spectra on uncoated insulators are recorded and will be discussed in detail in Chapter 5.

From the instrumentation side there is a renewed effort to better characterise the energy filtering properties of existing and purpose–built systems [116,117], and energy and angular acceptance diagrams describing one of the energy filtering instruments used in this work have been published very recently [118].

In summary, SEHI is a surface sensitive technique which is able to resolve nanoscale structural and compositional differences on surfaces of beam–sensitive insulators. Energy regions can be selected in which compositional contrast dominates, effectively enabling mapping of domains of interest for macroscopic properties such as tensile performance. The good compatibility of secondary electron microscopy and low–voltage SEM make for a promising microanalysis tool for nanostructured natural materials, and significant advances in the theoretical and practical understanding of this technique have been achieved in the past 5 years.

2.6   Data Analysis Strategies

When recording spectral images on a microscope, the resulting data can be imagined as a volume with one energy and two space dimensions in the case of electron spectroscopy. Depending on the number, and file size of acquired the images, the overall data volume can become quite large. This is a big opportunity, as significant nano–scale information can be corelated to energy information over a representative field of view. However, large data volumes also bring challenges: they require higher processing power for their manipulation, simple data analysis techniques become increasingly laborious and the interpretation and presentation of results may become complex. For efficient analysis one may limit the analysis to a point of interest, i.e. an energy peak throughout the image or the spectra of a small region compared to another. However, this would disregard significant portions of the data volume. Another way of reducing the dimensionality of 3D data sets while taking the entirety of the recorded data into account is through the use of multivariate component analysis (MVA) algorithms [119]. These statistical processes have been applied to mathematical and geometrical problems for more than a century [120], were first applied to electron energy loss spectroscopy (EELS) data in 1990 [121], and have become increasingly important for the processing of multivariate image data [65,119,122–125]. Secondary electron spectroscopy can build upon previous methods developed in the EELS community, where multivariate component analysis, mostly in the form of a principal component analysis (PCA), is now routinely performed and offered as part of analysis software packages [125].

Alongside the rise of PCA, other algorithms have been suggested and applied successfully. Peña et al. suggest that the independent component analysis (ICA) is superior to PCA in its reduced sensitivity to the background signal [122], while Dobigeon and Brun see improvements compared to both PCA and ICA in their analysis using yet

another algorithm which they call spectral unmixing [123]. The differences between multivariate analysis algorithms are subtle to the non–statistician. A highly technical yet application driven treatment of the limitations and common pitfalls of PCA and ICA have been discussed by Potapov [126], who also points out that data pre–treatment can be crucial to obtaining accurate results. Other considerations when selecting an algorithm for a data set is the processing power required and the sensitivity of the respective algorithm to noise; some successful applications of ICA require the results of an initial PCA to eliminate noise before executing the more resource intensive ICA [122].

The subtle differences between published MVA processes and their implications for the required input data and resulting outputs are perhaps the reason why there is currently no consensus as to which algorithm is best suited for EELS data. It follows that the effectiveness of different algorithms will ideally have to be investigated and optimised for the successful use of multivariate analysis on secondary electron spectral image data. For now, however, the analysis results can always be evaluated against expectation even in complex systems where not all component locations are reliably known, as the extrapolated components can be mapped within the field of view. An example of the successful application of a non–negative matrix factorization on secondary electron spectroscopic data is given by Masters et al. [111], where the local component loadings successfully mapped regions of increased and decreased nanoscale order in a polymer blend, allowing a tentative quantification, and highlighting the potential which MVA methods hold for SE spectroscopic analysis of nanostructured polymer systems.

2.7   References

1.   G.H. Michler: Electron microscopy of polymers, (Springer Science & Business Media, 2008).

2.   P. Atkins and J. de Paula: Atkins' Physical Chemistry, (OUP Oxford, 2010), https://books.google.co.uk/books?id=BV6cAQAAQBAJ.

3.   J.L. Yarger, B.R. Cherry and A. Van Der Vaart: *Uncovering the structure–function relationship in spider silk*. Nat. Rev. Mater. **3**, 18008 (2018).

4.   A. Gandini and M.N. Belgacem: *Chapter 1 – The State of the Art*, in: M.N. Belgacem, A.B.T.-M. Gandini Polymers and Composites from Renewable Resources (Eds.): (Elsevier, Amsterdam, 2008), pp. 1–16, doi:https://doi.org/10.1016/B978-0-08-045316-3.00001-6.

5.   U.G.K. Wegst, H. Bai, E. Saiz, A.P. Tomsia and R.O. Ritchie: *Bioinspired structural materials*. Nat. Mater. **14**, 23 (2014), https://doi.org/10.1038/nmat4089.

6.   F. Vollrath and D.P. Knight: *Liquid crystalline spinning of spider silk*. Nature **410**, 541–548 (2001).

7.   X.-X. Xia, Z.-G. Qian, C.S. Ki, Y.H. Park, D.L. Kaplan and S.Y. Lee: *Native-sized recombinant spider silk protein produced in metabolically engineered Escherichia coli results in a strong fiber*. Proc. Natl. Acad. Sci. **107**, 14059–14063 (2010).

8.   O. Tokareva, V.A. Michalczechen-Lacerda, E.L. Rech and D.L. Kaplan: *Recombinant DNA production of spider silk proteins*. Microb. Biotechnol. **6**, 651–663 (2013), doi:10.1111/1751-7915.12081.

9.   A. Rising, M. Widhe and J. Johansson: *Spider silk proteins: recent advances in recombinant production, structure–function relationships and biomedical applications*. Cell. Mol. Life Sci. **68**, 169–184 (2011).

10.   M. Andersson, Q. Jia, A. Abella, X.-Y. Lee, M. Landreh, P. Purhonen, H. Hebert, M. Tenje, C. V Robinson and Q. Meng: *Biomimetic spinning of artificial spider silk from a chimeric minispidroin*. Nat. Chem. Biol. **13**, 262 (2017).

11.   S. Rammensee, U. Slotta, T. Scheibel and A.R. Bausch: *Assembly mechanism of recombinant spider silk proteins*. Proc. Natl. Acad. Sci. **105**, 6590–6595 (2008).

12.   Q. Peng, Y. Zhang, L. Lu, H. Shao, K. Qin, X. Hu and X. Xia: *Recombinant spider silk from aqueous solutions via a bio-inspired microfluidic chip*. Sci. Rep. **6**, 36473 (2016).

13.   H. Chung, T.Y. Kim and S.Y. Lee: *Recent advances in production of recombinant spider silk proteins*. Curr. Opin. Biotechnol. **23**, 957–964 (2012).

14.   M. Heim, D. Keerl and T. Scheibel: *Spider silk: from soluble protein to extraordinary fiber*. Angew. Chemie Int. Ed. **48**, 3584–3596 (2009).

15.   G. V Guinea, M. Elices, J. Pérez-Rigueiro and G.R. Plaza: *Stretching of supercontracted fibers: a link between spinning and the variability of spider silk*. J. Exp. Biol. **208**, 25 (2004), http://jeb.biologists.org/content/208/1/25.abstract.

16.   D.P. Knight, M.M. Knight and F. Vollrath: *Beta transition and stress-induced phase separation in the spinning of spider dragline silk*. Int. J. Biol. Macromol. **27**, 205–210 (2000).

17.   G. Li, P. Zhou, Z. Shao, X. Xie, X. Chen, H. Wang, L. Chunyu and T. Yu: *The natural silk spinning process*. Eur. J. Biochem. **268**, 6600–6606 (2001), doi:10.1046/j.0014-2956.2001.02614.x.

18.   G. Askarieh, M. Hedhammar, K. Nordling, A. Saenz, C. Casals, A. Rising, J. Johansson and S.D. Knight: *Self-assembly of spider silk proteins is controlled by a pH-sensitive relay*. Nature **465**, 236 (2010).

19.   F. Hagn, C. Thamm, T. Scheibel and H. Kessler: *pH-Dependent Dimerization and Salt-Dependent Stabilization of the N-terminal Domain of Spider Dragline Silk—Implications for Fiber Formation*. Angew. Chemie Int. Ed. **50**, 310–313 (2011).

20.   N.A. Oktaviani, A. Matsugami, F. Hayashi and K. Numata: *Ion effects on the conformation and dynamics of repetitive domains of a spider silk protein: implications for solubility and β-sheet formation*. Chem. Commun. (2019).

21.   M. Hronska, J.D. Van Beek, P.T.F. Williamson, F. Vollrath and B.H. Meier: *NMR characterization of native liquid spider dragline silk from Nephila edulis*. Biomacromolecules **5**, 834–839 (2004).

22.   J.E. Jenkins, G.P. Holland and J.L. Yarger: *High resolution magic angle spinning NMR investigation of silk protein structure within major ampullate glands of orb weaving*

spiders. Soft Matter **8**, 1947–1954 (2012).

23.   L.R. Parent, D. Onofrei, D. Xu, D. Stengel, J.D. Roehling, J.B. Addison, C. Forman, S.A. Amin, B.R. Cherry, J.L. Yarger, N.C. Gianneschi and G.P. Holland: *Hierarchical spidroin micellar nanoparticles as the fundamental precursors of spider silks*. Proc. Natl. Acad. Sci. U. S. A. **115**, 11507–11512 (2018), doi:10.1073/pnas.1810203115.

24.   F. Hagn, L. Eisoldt, J.G. Hardy, C. Vendrely, M. Coles, T. Scheibel and H. Kessler: *A conserved spider silk domain acts as a molecular switch that controls fibre assembly*. Nature **465**, 239 (2010).

25.   T.-Y. Lin, H. Masunaga, R. Sato, A.D. Malay, K. Toyooka, T. Hikima and K. Numata: *Liquid crystalline granules align in a hierarchical structure to produce spider dragline microfibrils*. Biomacromolecules **18**, 1350–1355 (2017).

26.   H.-J. Jin and D.L. Kaplan: *Mechanism of silk processing in insects and spiders*. Nature **424**, 1057–1061 (2003), doi:10.1038/nature01809.

27.   L. Eisoldt, A. Smith and T. Scheibel: *Decoding the secrets of spider silk*. Mater. Today **14**, 80–86 (2011), doi:https://doi.org/10.1016/S1369-7021(11)70057-8.

28.   O. Tokareva, M. Jacobsen, M. Buehler, J. Wong and D.L. Kaplan: *Structure–function–property–design interplay in biopolymers: Spider silk*. Acta Biomater. **10**, 1612–1626 (2014).

29.   M. Xu and R. V Lewis: *Structure of a protein superfiber: spider dragline silk*. Proc. Natl. Acad. Sci. **87**, 7120–7124 (1990).

30.   R. V Lewis: *Spider silk: the unraveling of a mystery*. Acc. Chem. Res. **25**, 392–398 (1992).

31.   M.B. Hinman and R. V Lewis: *Isolation of a clone encoding a second dragline silk fibroin. Nephila clavipes dragline silk is a two-protein fiber*. J. Biol. Chem. **267**, 19320–19324 (1992).

32.   Y. Liu, Z. Shao and F. Vollrath: *Relationships between supercontraction and mechanical properties of spider silk*. Nat Mater **4**, 901–905 (2005), doi:doi:10.1038/nmat1534.

33.   Y. Liu, A. Sponner, D. Porter and F. Vollrath: *Proline and processing of spider silks*. Biomacromolecules **9**, 116–121 (2007).

34.   S.F. Li, A.J. McGhie and S.L. Tang: *New internal structure of spider dragline silk revealed by atomic force microscopy*. Biophys. J. **66**, 1209–1212 (1994), doi:http://dx.doi.org/10.1016/S0006-3495(94)80903-8.

35.   T. Giesa, M. Arslan, N.M. Pugno and M.J. Buehler: *Nanoconfinement of spider silk fibrils begets superior strength, extensibility, and toughness*. Nano Lett. **11**, 5038–5046 (2011).

36.   N. Du, X.Y. Liu, J. Narayanan, L. Li, M.L.M. Lim and D. Li: *Design of Superior Spider Silk: From Nanostructure to Mechanical Properties*. Biophys. J. **91**, 4528–4535 (2006), doi:http://dx.doi.org/10.1529/biophysj.106.089144.

37.   P. Poza, J. Perez-Rigueiro, M. Elices and J. Llorca: *Fractographic analysis of silkworm and spider silk*. Eng. Fract. Mech. **69**, 1035–1048 (2002).

38.   L.D. Miller, S. Putthanarat, R.K. Eby and W.W. Adams: *Investigation of the nanofibrillar morphology in silk fibers by small angle X-ray scattering and atomic force microscopy*. Int. J. Biol. Macromol. **24**, 159–165 (1999), doi:http://dx.doi.org/10.1016/S0141-8130(99)00024-0.

39.   Q. Wang and H.C. Schniepp: *Nanofibrils as Building Blocks of Silk Fibers: Critical Review of the Experimental Evidence*. Jom (2019), doi:10.1007/s11837-019-03340-y.

40.   A. Sponner, W. Vater, S. Monajembashi, E. Unger, F. Grosse and K. Weisshart: *Composition and hierarchical organisation of a spider silk*. PLoS One **2**, e998 (2007).

41.   A. Nova, S. Keten, N.M. Pugno, A. Redaelli and M.J. Buehler: *Molecular and nanostructural mechanisms of deformation, strength and toughness of spider silk fibrils*. Nano Lett. **10**, 2626–2634 (2010).

42.   S. Keten, Z. Xu, B. Ihle and M.J. Buehler: *Nanoconfinement controls stiffness, strength and mechanical toughness of [beta]-sheet crystals in silk*. Nat. Mater. **9**, 359–367 (2010).

43.   Y. Termonia: *Molecular Modeling of Spider Silk Elasticity*. Macromolecules **27**, 7378–7381 (1994), doi:10.1021/ma00103a018.

44.   I. Su and M.J. Buehler: *Nanomechanics of silk: the fundamentals of a strong, tough and versatile material*. Nanotechnology **27**, 302001 (2016).

45.   P. Colomban, H.M. Dinh, J. Riand, L.C. Prinsloo and B. Mauchamp: *Nanomechanics of single silkworm and spider fibres: a Raman and micro-mechanical in situ study of the conformation change with stress*. J. Raman Spectrosc. **39**, 1749–1764 (2008).

46.   N.A. Stehling, K.J. Abrams, C. Holland and C. Rodenburg: *Revealing spider silk's 3D*

nanostructure through low temperature plasma etching and advanced low-voltage SEM. Front. Mater. **5**, 84 (2018).

47.   F. Vollrath, B. Madsen and Z. Shao: *The effect of spinning conditions on the mechanics of a spider's dragline silk*. Proc. R. Soc. London B Biol. Sci. **268**, 2339–2346 (2001).

48.   N. Du, Z. Yang, X.Y. Liu, Y. Li and H.Y. Xu: *Structural Origin of the Strain-Hardening of Spider Silk*. Adv. Funct. Mater. **21**, 772–778 (2011), doi:10.1002/adfm.201001397.

49.   B. Madsen, Z.Z. Shao and F. Vollrath: *Variability in the mechanical properties of spider silks on three levels: interspecific, intraspecific and intraindividual*. Int. J. Biol. Macromol. **24**, 301–306 (1999).

50.   F. Vollrath: *Biology of spider silk*. Int. J. Biol. Macromol. **24**, 81–88 (1999).

51.   M. McGill, G.P. Holland and D.L. Kaplan: *Experimental Methods for Characterizing the Secondary Structure and Thermal Properties of Silk Proteins*. Macromol. Rapid Commun. **0**, 1800390 (2018), doi:10.1002/marc.201800390.

52.   K.B. Guess and C. Viney: *Thermal analysis of major ampullate (drag line) spider silk: the effect of spinning rate on tensile modulus1Presented at TAC 97, Oxford, UK, 14–15 April 1997.1*. Thermochim. Acta **315**, 61–66 (1998), doi:https://doi.org/10.1016/S0040-6031(98)00277-9.

53.   Y. Yang, X. Chen, Z. Shao, P. Zhou, D. Porter, D.P. Knight and F. Vollrath: *Toughness of spider silk at high and low temperatures*. Adv. Mater. **17**, 84–88 (2005).

54.   E.M. Pogozelski, W.L. Becker, B.D. See and C.M. Kieffer: *Mechanical testing of spider silk at cryogenic temperatures*. Int. J. Biol. Macromol. **48**, 27–31 (2011).

55.   J. Guan, Y.Y. Wang, B. Mortimer, C. Holland, Z. Shao, D. Porter and F. Vollrath: *Glass transitions in native silk fibres studied by dynamic mechanical thermal analysis*. Soft Matter **12**, 5926–5936 (2016), doi:10.1039/C6SM00019C.

56.   G.R. Plaza, G. V Guinea, J. Pérez-Rigueiro and M. Elices: *Thermo-hygro-mechanical behavior of spider dragline silk: Glassy and rubbery states*. J. Polym. Sci. Part B Polym. Phys. **44**, 994–999 (2006), doi:10.1002/polb.20751.

57.   H.-S. Sheu, K.W. Phyu, Y.-C. Jean, Y.-P. Chiang, I.-M. Tso, H.-C. Wu, J.-C. Yang and S.-L. Ferng: *Lattice deformation and thermal stability of crystals in spider silk*. Int. J. Biol. Macromol. **34**, 267–273 (2004), doi:https://doi.org/10.1016/j.ijbiomac.2004.09.004.

58.   Z. Shao, F. Vollrath, J. Sirichaisit and R.J. Young: *Analysis of spider silk in native and supercontracted states using Raman spectroscopy*. Polymer (Guildf). **40**, 2493–2500 (1999).

59.   D.B. Gillespie, C. Viney and P. Yager: *Raman Spectroscopic Analysis of the Secondary Structure of Spider Silk Fiber*, in: *Silk Polymers*, (American Chemical Society, 2016), pp. 155–167, doi:doi:10.1021/bk-1994-0544.ch014 10.1021/bk-1994-0544.ch014.

60.   M.-E. Rousseau, T. Lefèvre, L. Beaulieu, T. Asakura and M. Pézolet: *Study of Protein Conformation and Orientation in Silkworm and Spider Silk Fibers Using Raman Microspectroscopy*. Biomacromolecules **5**, 2247–2257 (2004), doi:10.1021/bm049717v.

61.   J. Sirichaisit, V.L. Brookes, R.J. Young and F. Vollrath: *Analysis of Structure/Property Relationships in Silkworm (Bombyx mori) and Spider Dragline (Nephila edulis) Silks Using Raman Spectroscopy*. Biomacromolecules **4**, 387–394 (2003), doi:10.1021/bm0256956.

62.   F. Paquet-Mercier, T. Lefevre, M. Auger and M. Pezolet: *Evidence by infrared spectroscopy of the presence of two types of [small beta]-sheets in major ampullate spider silk and silkworm silk*. Soft Matter **9**, 208–215 (2013), doi:10.1039/C2SM26657A.

63.   T. Lefèvre, F. Paquet-Mercier, J. Rioux-Dubé and M. Pézolet: *Structure of silk by Raman spectromicroscopy: From the spinning glands to the fibers*. Biopolymers **97**, 322–336 (2012).

64.   M. Boulet-Audet, F. Vollrath and C. Holland: *Identification and classification of silks using infrared spectroscopy*. J. Exp. Biol. **218**, (2015), doi:10.1242/jeb.128306.

65.   X. Chen, D.P. Knight, Z. Shao and F. Vollrath: *Conformation Transition in Silk Protein Films Monitored by Time-Resolved Fourier Transform Infrared Spectroscopy: Effect of Potassium Ions on Nephila Spidroin Films*. Biochemistry **41**, 14944–14950 (2002), doi:10.1021/bi026550m.

66.   O. Hollricher, U. Schmidt and S. Breuninger: *RISE microscopy: correlative Raman-SEM imaging*. Micros. Today **22**, 36–39 (2014).

67.   A.A. van Apeldoorn, Y. Aksenov, M. Stigter, I. Hofland, J.D. de Bruijn, H.K. Koerten, C. Otto,

J. Greve and C.A. van Blitterswijk: *Parallel high-resolution confocal Raman SEM analysis of inorganic and organic bone matrix constituents*. J. R. Soc. Interface **2**, 39–45 (2005), doi:10.1098/rsif.2004.0018.

68. D.M. Chow, K.H. Tow, F. Vollrath, I. Dicaire, T. Gheysens and L. Thévenaz: *Shedding light on the optical properties of spider silk fiber*. 2015 IEEE Photonics Conf. 333–334 (2015).

69. T.A. Blackledge, R.A. Cardullo and C.Y. Hayashi: *Polarized light microscopy, variability in spider silk diameters, and the mechanical characterization of spider silk*. Invertebr. Biol. **124**, 165–173 (2005).

70. D.C. Lin, E.K. Dimitriadis and F. Horkay: *Robust strategies for automated AFM force curve analysis—I. Non-adhesive indentation of soft, inhomogeneous materials*. J. Biomech. Eng. **129**, 430–440 (2007).

71. A. Schäfer, T. Vehoff, A. Glišović and T. Salditt: *Spider silk softening by water uptake: an AFM study*. Eur. Biophys. J. **37**, 197–204 (2008).

72. C.P. Brown, J. MacLeod, H. Amenitsch, F. Cacho-Nerin, H.S. Gill, A.J. Price, E. Traversa, S. Licoccia and F. Rosei: *The critical role of water in spider silk and its consequence for protein mechanics*. Nanoscale **3**, 3805–3811 (2011).

73. A. Sponner, E. Unger, F. Grosse and K. Weisshart: *Conserved C-termini of spidroins are secreted by the major ampullate glands and retained in the silk thread*. Biomacromolecules **5**, 840–845 (2004).

74. Frische, Maunsbach and Vollrath: *Elongate cavities and skin–core structure in Nephila spider silk observed by electron microscopy*. J. Microsc. **189**, 64–70 (2002), doi:10.1046/j.1365-2818.1998.00285.x.

75. K. Augsten, P. Muehlig and C. Herrmann: *Glycoproteins and skin-core structure in Nephila clavipes spider silk observed by light and electron microscopy*. Scanning **22**, 12–15 (2000).

76. B.L. Thiel, D.D. Kunkel and C. Viney: *Physical and chemical microstructure of spider dragline: a study by analytical transmission electron microscopy*. Biopolym. Orig. Res. Biomol. **34**, 1089–1097 (1994).

77. S. Sampath, T. Isdebski, J.E. Jenkins, J. V Ayon, R.W. Henning, J.P.R.O. Orgel, O. Antipoa and J.L. Yarger: *X-ray diffraction study of nanocrystalline and amorphous structure within major and minor ampullate dragline spider silks*. Soft Matter **8**, 6713–6722 (2012), doi:10.1039/C2SM25373A.

78. Z. Shao, R.J. Young and F. Vollrath: *The effect of solvents on spider silk studied by mechanical testing and single-fibre Raman spectroscopy*. Int. J. Biol. Macromol. **24**, 295–300 (1999).

79. N. Stehling, R. Masters, Y. Zhou, R. O'Connell, C. Holland, H. Zhang and C. Rodenburg: *New perspectives on nano-engineering by secondary electron spectroscopy in the helium ion and scanning electron microscope*. MRS Commun. **8**, 226–240 (2018), doi:10.1557/mrc.2018.75.

80. M. Knoll and E. Ruska: *Das Elektronenmikroskop*. Zeitschrift Für Phys. **78**, 318–339 (1932), doi:10.1007/BF01342199.

81. E. Ruska: *The development of the electron microscope and of electron microscopy*. Rev. Mod. Phys. **59**, 627 (1987).

82. A. Bogner, P.-H. Jouneau, G. Thollet, D. Basset and C. Gauthier: *A history of scanning electron microscopy developments: towards "wet-STEM" imaging*. Micron **38**, 390–401 (2007).

83. M. Pilhofer, M.S. Ladinsky, A.W. McDowall and G.J. Jensen: *Bacterial TEM: new insights from cryo-microscopy*, in: *Methods in Cell Biology*, (Elsevier, 2010), pp. 21–45.

84. S.R. Adams, M.R. Mackey, R. Ramachandra, S.F. Palida Lemieux, P. Steinbach, E.A. Bushong, M.T. Butko, B.N.G. Giepmans, M.H. Ellisman and R.Y. Tsien: *Multicolor Electron Microscopy for Simultaneous Visualization of Multiple Molecular Species*. Cell Chem. Biol. **23**, 1417–1427 (2016), doi:10.1016/j.chembiol.2016.10.006.

85. M. Suga, S. Asahina, Y. Sakuda, H. Kazumori, H. Nishiyama, T. Nokuo, V. Alfredsson, T. Kjellman, S.M. Stevens, H.S. Cho, M. Cho, L. Han, S. Che, M.W. Anderson, F. Schüth, H. Deng, O.M. Yaghi, Z. Liu, H.Y. Jeong, A. Stein, K. Sakamoto, R. Ryoo and O. Terasaki: *Recent progress in scanning electron microscopy for the characterization of fine structural details of nano materials*. Prog. Solid State Chem. **42**, 1–21 (2014), doi:http://dx.doi.org/10.1016/j.progsolidstchem.2014.02.001.

86. J. Cazaux: *Recent developments and new strategies in scanning electron microscopy*. J.

Microsc. **217**, 16–35 (2005).

87.   D.C. Joy and C.S. Joy: *Low voltage scanning electron microscopy*. Micron **27**, 247–263 (1996), doi:10.1016/0968-4328(96)00023-6.

88.   J.H. Butler, D.C. Joy, G.F. Bradley and S.J. Krause: *Low-voltage scanning electron microscopy of polymers*. Polymer (Guildf). **36**, 1781–1790 (1995).

89.   J.B. Pawley: *LVSEM for Biology BT - Biological Low-Voltage Scanning Electron Microscopy*, in: H. Schatten, J.B. Pawley (Eds.): (Springer New York, New York, NY, 2008), pp. 27–106, doi:10.1007/978-0-387-72972-5_2.

90.   J. Pawley: *Low voltage scanning electron microscopy*. J. Microsc. **136**, 45–68 (1984).

91.   R.F. Egerton, P. Li and M. Malac: *Radiation damage in the TEM and SEM*. Micron **35**, 399–409 (2004).

92.   S. Ning, T. Fujita, A. Nie, Z. Wang, X. Xu, J. Chen, M. Chen, S. Yao and T.-Y. Zhang: *Scanning distortion correction in STEM images*. Ultramicroscopy **184**, 274–283 (2018), doi:https://doi.org/10.1016/j.ultramic.2017.09.003.

93.   M. Schaffer, B. Schaffer and Q. Ramasse: *Sample preparation for atomic-resolution STEM at low voltages by FIB*. Ultramicroscopy **114**, 62–71 (2012), doi:https://doi.org/10.1016/j.ultramic.2012.01.005.

94.   J. Cazaux: *Some considerations on the secondary electron emission, δ, from e⁻ irradiated insulators*. J. Appl. Phys. **85**, 1137–1147 (1999).

95.   E.I. Rau, E.N. Evstaf'eva and M. V Andrianov: *Mechanisms of charging of insulators under irradiation with medium-energy electron beams*. Phys. Solid State **50**, 621–630 (2008).

96.   D.C. Joy: *Control of charging in low-voltage SEM*. Scanning **11**, 1–4 (1989).

97.   D.C. Joy and C.S. Joy: *Dynamic charging in the low voltage SEM*. Microsc. Microanal. **1**, 109–112 (1995).

98.   H. Schatten: *Low voltage high-resolution SEM (LVHRSEM) for biological structural and molecular analysis*. Micron **42**, 175–185 (2011), doi:https://doi.org/10.1016/j.micron.2010.08.008.

99.   G.P. Lopez, H.A. Biebuyck and G.M. Whitesides: *Scanning electron microscopy can form images of patterns in self-assembled monolayers*. Langmuir **9**, 1513–1516 (1993).

100.   B.J. Griffin: *A comparison of conventional Everhart-Thornley style and in-lens secondary electron detectors—a further variable in scanning electron microscopy*. Scanning **33**, 162–173 (2011).

101.   O.L. Krivanek, T.C. Lovejoy, N. Dellby, T. Aoki, R.W. Carpenter, P. Rez, E. Soignard, J. Zhu, P.E. Batson and M.J. Lagos: *Vibrational spectroscopy in the electron microscope*. Nature **514**, 209–212 (2014).

102.   P. Rez, T. Aoki, K. March, D. Gur, O.L. Krivanek, N. Dellby, T.C. Lovejoy, S.G. Wolf and H. Cohen: *Damage-free vibrational spectroscopy of biological materials in the electron microscope*. Nat. Commun. **7**, 1–8 (2016).

103.   F.S. Hage, R.J. Nicholls, J.R. Yates, D.G. McCulloch, T.C. Lovejoy, N. Dellby, O.L. Krivanek, K. Refson and Q.M. Ramasse: *Nanoscale momentum-resolved vibrational spectroscopy*. Sci. Adv. **4**, eaar7495 (2018).

104.   M. Nagoshi, T. Aoyama and K. Sato: *Extraction of topographic and material contrasts on surfaces from SEM images obtained by energy filtering detection with low-energy primary electrons*. Ultramicroscopy **124**, 20–25 (2013).

105.   M. Nagoshi, T. Kawano and K. Sato: *Simple separations of topographic and material contrasts using one annular type in-lens detector of low-voltage SEM*. Surf. Interface Anal. (2015).

106.   R. Rasch, A. Stricher and R.W. Truss: *Energy filtered low voltage "in lens detector" SEM and XPS of natural fiber surfaces*. J. Appl. Polym. Sci. **131**, (2014).

107.   Q. Wan, R.C. Masters, D. Lidzey, K.J. Abrams, M. Dapor, R.A. Plenderleith, S. Rimmer, F. Claeyssens and C. Rodenburg: *Angle selective backscattered electron contrast in the low-voltage scanning electron microscope: Simulation and experiment for polymers*. Ultramicroscopy **171**, 126–138 (2016), doi:http://dx.doi.org/10.1016/j.ultramic.2016.09.006.

108.   J. Cazaux, N. Kuwano and K. Sato: *Backscattered electron imaging at low emerging angles: A physical approach to contrast in LVSEM*. Ultramicroscopy **135**, 43–49 (2013).

109.   V. Kumar, W.L. Schmidt, G. Schileo, R.C. Masters, M. Wong-Stringer, D.C. Sinclair, I.M. Reaney, D. Lidzey and C. Rodenburg: *Nanoscale Mapping of Bromide Segregation on the Cross Sections of Complex Hybrid Perovskite Photovoltaic Films Using Secondary*

Electron Hyperspectral Imaging in a Scanning Electron Microscope. ACS Omega **2**, 2126–2133 (2017).

110.   M. Dapor, R.C. Masters, I. Ross, D.G. Lidzey, A. Pearson, I. Abril, R. Garcia-Molina, J. Sharp, M. Unčovský, T. Vystavel, F. Mika and C. Rodenburg: *"Secondary electron spectra of semi-crystalline polymers – A novel polymer characterisation tool?"* J. Electron Spectros. Relat. Phenomena **222**, 95–105 (2018), doi:10.1016/j.elspec.2017.08.001.

111.   R.C. Masters, N.A. Stehling, K.J. Abrams, V. Kumar, M. Azzolini, N.M. Pugno, M. Dapor, A. Huber, P. Schäfer, D.G. Lidzey and C. Rodenburg: *Mapping Polymer Molecular Order in the SEM with Secondary Electron Hyperspectral Imaging*. Adv. Sci. (2019).

112.   M. Azzolini, T. Morresi, K. Abrams, R. Masters, N. Stehling, C. Rodenburg, N.M. Pugno, S. Taioli and M. Dapor: An Anisotropic Approach for Simulating Electron Transport in Layered Materials: Computational and Experimental Study of Highly Oriented Pyrolitic Graphite, 2018), doi:10.1021/acs.jpcc.8b02256.

113.   K.J. Abrams, M. Dapor, N. Stehling, M. Azzolini, S.J. Kyle, J.S. Schäfer, A. Quade, F. Mika, S. Kratky and Z. Pokorna: *Making Sense of Complex Carbon and Metal/Carbon Systems by Secondary Electron Hyperspectral Imaging*. Adv. Sci. 1900719 (2019).

114.   C. Li, S.F. Mao and Z.J. Ding: *Time-dependent characteristics of secondary electron emission*. J. Appl. Phys. **125**, 24902 (2019), doi:10.1063/1.5080264.

115.   C. Li, S.F. Mao, Y.B. Zou, Y.G. Li, P. Zhang, H.M. Li and Z.J. Ding: *A Monte Carlo modeling on charging effect for structures with arbitrary geometries*. J. Phys. D. Appl. Phys. **51**, 165301 (2018), doi:10.1088/1361-6463/aab2cf.

116.   A. Khursheed: Scanning electron microscope optics and spectrometers, 1st ed., (World Scientific Co Pte, Singapore, 2010).

117.   W. Han, A. Srinivasan, A. Banerjee, M. Chew and A. Khursheed: *Beyond conventional secondary electron imaging using spectromicroscopy and its applications in dopant profiling*. Mater. Today Adv. **2**, 100012 (2019), doi:https://doi.org/10.1016/j.mtadv.2019.100012.

118.   I. Konvalina, F. Mika, S. Krátký, E. Materna Mikmeková and I. Müllerová: *In-Lens Band-Pass Filter for Secondary Electrons in Ultrahigh Resolution SEM*. Materials (Basel). **12**, 2307 (2019).

119.   M.W. Berry, M. Browne, A.N. Langville, V.P. Pauca and R.J. Plemmons: *Algorithms and applications for approximate nonnegative matrix factorization*. Comput. Stat. Data Anal. **52**, 155–173 (2007).

120.   K. Pearson: *LIII. On lines and planes of closest fit to systems of points in space*. London, Edinburgh, Dublin Philos. Mag. J. Sci. **2**, 559–572 (1901), doi:10.1080/14786440109462720.

121.   P. Trebbia and N. Bonnet: *EELS elemental mapping with unconventional methods I. Theoretical basis: Image analysis with multivariate statistics and entropy concepts*. Ultramicroscopy **34**, 165–178 (1990).

122.   F. de la Peña, M.-H.H. Berger, J.-F.F. Hochepied, F. Dynys, O. Stephan and M. Walls: *Mapping titanium and tin oxide phases using EELS: An application of independent component analysis*. Ultramicroscopy **111**, 169–176 (2011), https://www.sciencedirect.com/science/article/pii/S030439911000255X (accessed September 11, 2019).

123.   N. Dobigeon and N. Brun: *Spectral mixture analysis of EELS spectrum-images*. Ultramicroscopy **120**, 25–34 (2012), https://www.sciencedirect.com/science/article/pii/S0304399112001088 (accessed September 11, 2019).

124.   N. Bonnet and D. Nuzillard: *Independent component analysis: A new possibility for analysing series of electron energy loss spectra*. Ultramicroscopy **102**, 327–337 (2005).

125.   F.I. Allen, M. Watanabe, Z. Lee, N.P. Balsara and A.M. Minor: *Chemical mapping of a block copolymer electrolyte by low-loss EFTEM spectrum-imaging and principal component analysis*. Ultramicroscopy (2011), doi:10.1016/j.ultramic.2010.11.035.

126.   P. Potapov: *Why Principal Component Analysis of STEM spectrum-images results in "abstract", uninterpretable loadings?* Ultramicroscopy (2016), doi:10.1016/j.ultramic.2015.10.020.

3 Materials and Methods

3.1 Instruments and Methods

3.1.1 SEM

SEM images and secondary electron spectra presented in this thesis were acquired using two different instruments.

3.1.1.1 Imaging

FEI Nova NanoSEM450

The FEI Nova NanoSEM450 (Thermo Fisher Scientific, **Figure 3.1 a**) is a dedicated scanning electron microscope, and although it is the older generation its low–voltage SEM capabilities make it suitable for the observation of uncoated insulators at high spatial resolution. Unless otherwise specified, images were acquired at 1 keV primary beam voltage 16 pA beam current, a working distance of 3 mm and vacuum pressures below 5 x 10^{-5} mbar.

FEI Helios NanoLab G3 UC

The FEI Helios NanoLab G3 UC (Thermo Fisher Scientific, **Figure 3.1 b**) is a dual beam microscope (electron and ion beam), but was used exclusively for its high–specification low–voltage SEM capabilities in this project. Unless otherwise specified images were collected at 1 keV primary beam voltage, a working distance at the eucentric height of 4.1 mm, and vacuums below 3 x 10^{-5} mbar.
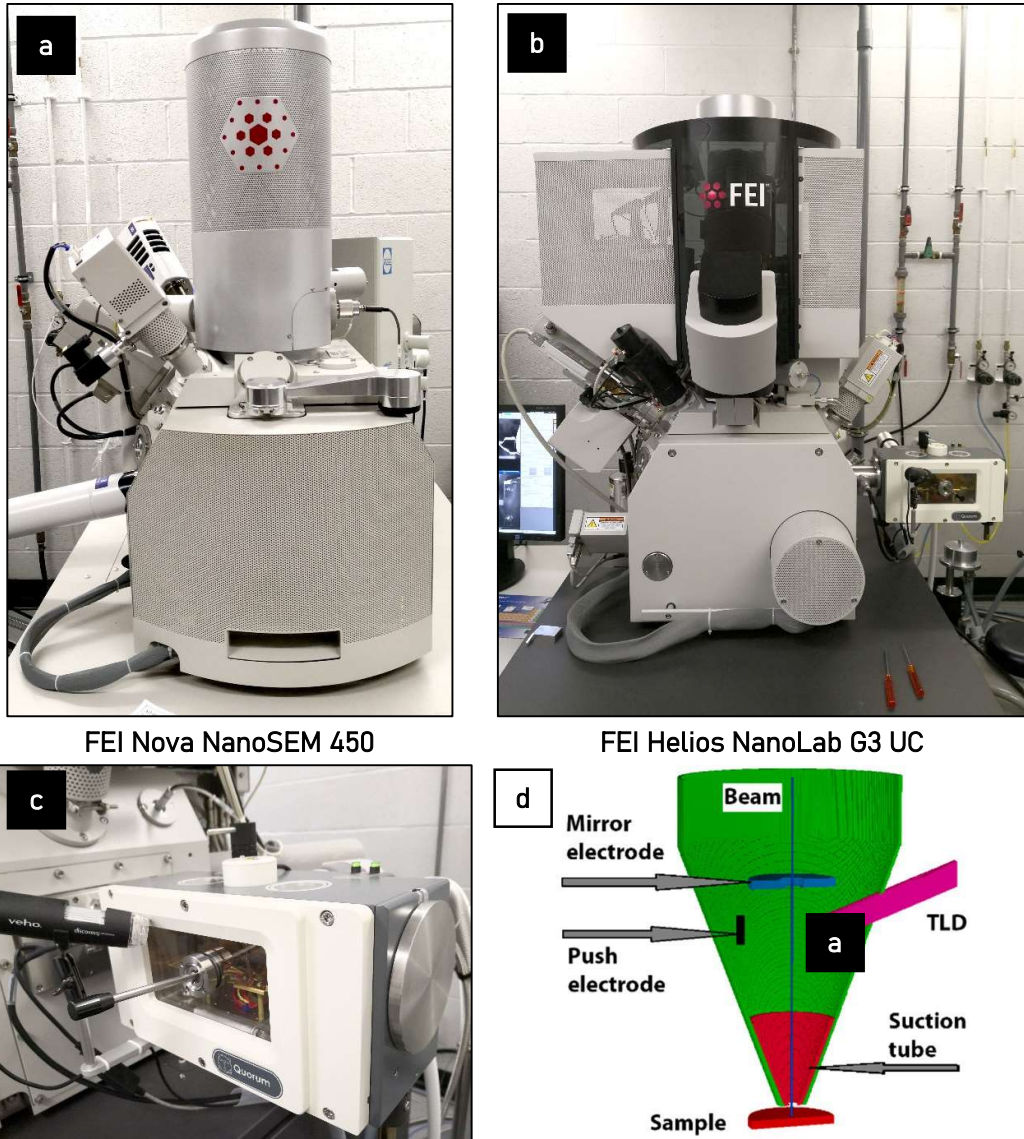
Figure 3.1: Depictions of the SEM instruments a) Nova NanoSEM450 b) Helios NanoLab G3 UC c) Quorum PP3010T preparation system on the Helios d) Secondary electron energy filter set-up on the Helios (TLD stands for through-lens detector), reproduced from [1] under a CC BY 4.0 licence (https://creativecommons.org/licenses/by/4.0/)

Helios Cryo-SEM

The Helios SEM has cryo-SEM capabilities through a dedicated Quorum PP3010T system attachment (Quorum Technologies Ltd, **Figure 3.1 c**), which allows preparation and observation of samples down to -180 °C. The respective sample preparation protocol is specified in section 3.2. For imaging, the sample was held at -180 °C with the cold finger

(or anti-contaminator) kept at –190 °C in order to capture volatile species in the chamber. All other imaging parameters were as specified for room temperature imaging in the Helios.

Helium Ion Microscope

Within chapter 4 results from two helium ion microscopes are presented: the Zeiss Orion plus and the Zeiss Orion NanoFAB. The instruments were accessed through collaboration with the University of Dublin Trinity College School of Physics (Dublin, IE) under a Royal Society International Exchange grant (IE140211). Unless otherwise specified images were collected using the Everhart Thornley detector with 30 keV He^+ beam energy and a chamber vacuum of approximately 5×10^{-7} mbar.

3.1.1.2   *Spectral acquisition*

Spectra in the helium ion microscope were collected using a retarding grid—effectively a TEM grid on a nanomanipulator arm—as described in detail by Zhou et al. [2], and further discussed in chapter 4. The retarding grid is increasingly negatively biased while a series of images is collected. Thus, the grid acts as a high pass filter for secondary electrons, as lower energy electrons are deflected away from the grid and only higher energy electrons make it to the detector. The charge-neutralising electron flood gun was not used during the collection of spectra shown in chapter 4.

Both the Helios and Nova SEMs have column and detector designs which allow energy filtering of secondary electrons and the collection of secondary electron spectra through serial acquisition. No stage bias or beam deceleration was used in this project.

FEI Helios NanoLab SEM spectra were acquired using the through-lens detector in 'Custom' mode, applying a 150 V suction tube voltage and scanning the mirror electrode voltages in the range of –20 to 20 V). The column is shown schematically in **Figure 3.1 d**.

The Nova energy filter set-up is shown in Chapter 4. Secondary electron energy differentiation is performed in the through-lens detection in immersion mode with a suction tube voltage of 250 V. Deflector voltages are scanned from 0 to 50 V.

By scanning the voltage on the mirror (Helios) or deflector electrode (Nova) over a range and generating an image for each voltage setting, the energy range of collected SEs is controlled by a low- or high-pass filtration. Spectra and hyperspectral images are obtained through differentiation and post-processing of the spectral image series, further detailed in section 3.1.2.1.

The energy calibration of this process is performed through stage bias experiments [3]: the secondary electron spectrum of a conductive sample (in this case gold) is measured as a function of a voltage applied on the stage and thus also the interaction volume. The spectrum shifts to higher energies with negative stage biases and to lower energies with positive stage biases, as the bias influences the secondary electron emission energies. A stage bias of –1 V increases the emission energy of an electron by 1 eV, and thus the energy scale can be calibrated by considering that a stage bias of –1 V shifts the spectrum to the right by 1 eV. For a detailed discussion of the detector designs of the Nova and Helios please refer to Chapter 4 [4].

3.1.2   Data analysis

3.1.2.1   *Image processing*

The steps required for spectral analysis of the data acquired on both SEMs include making a continuous stack and aligning all images using a template matching procedure based on the normalised correlation coefficient of the images to be aligned. A region of interest is then selected and the average brightness with energy in form of an S-curve is plotted. As the S-curve describes a cumulative collection of SE energies,

the SE spectrum is obtained through differentiation of the data. The processes are illustrated in the flow chart shown in **Figure 3.2**.

On the microscope

- Find object
- Adjust focus and imaging parameters
- Select spectral collection parameters
- Set E = Emin
- Take image
- Increment E
- E > Emax?
  - No
  - Yes
- Spectral image series complete

Transfer data from microscope

Post-processing

- Bundle spectral images into one 'stack'
- Align images
- Select ROI in stack
- plot average ROI brightness as function of E
- further ROI?
  - Yes
  - No
- S-curve of ROI
- Differentiate
- Spectrum of ROI
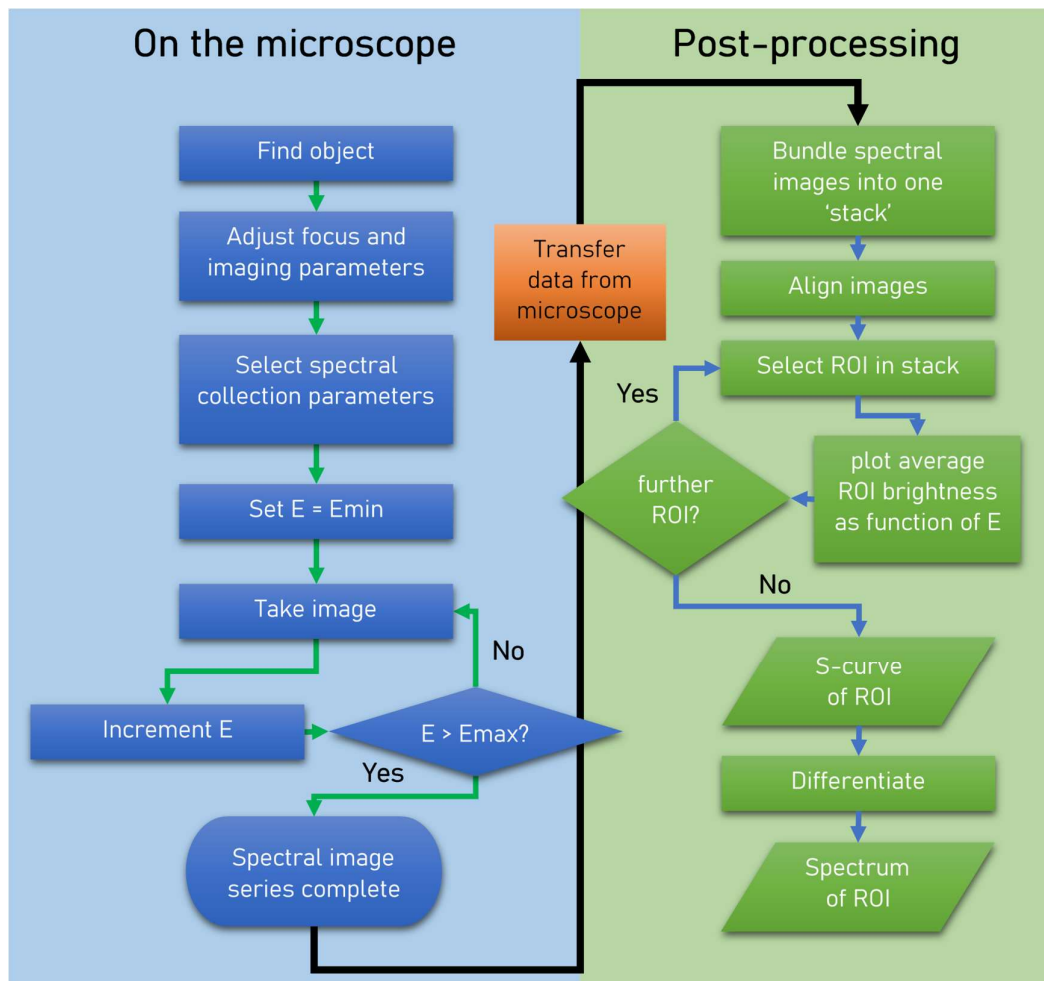
Figure 3.2: Flowchart illustrating the data collection and data processing on the microscope and on an external computer

Where appropriate, these steps were automated using a Matlab script initially created by Robert Masters and further refined throughout this project. For the more specific manipulation and analysis of image and spectral data sets FIJI (ImageJ 1.52p) was used [5].

3.1.2.2   Multivariate analysis—non-negative matrix factorisation

Multivariate analysis (MVA) was performed in Matlab 2017b for a 64-bit Windows operation system, the code of which is included in the Appendix. As negative emission values are unphysical in the case of the spectral data used, the non-negative matrix factorisation (NMF) algorithm was used to process the data [6]. The data was prepared for analysis by producing a stack in ImageJ and aligning all images where required. To reduce the sensitivity of the algorithm to noise present in the data set, a three-dimensional point spread function was applied to the data volume, with sigma values which are specified in the figure captions of the relevant chapter. Multiple stacks—acquired under different conditions—were loaded into the MVA in order to observe trends across a larger data set.

3.1.3   Mechanical testing

The details of spider silk single fibre tensile tests are detailed in Chapter 7. An image of the set-up and an exemplary tensile curve are shown in **Figure 3.3 b**. The reader is also kindly directed to a video of a sample tensile test, available at https://www.frontiersin.org/articles/10.3389/fmats.2018.00084/full#supplementary-material.
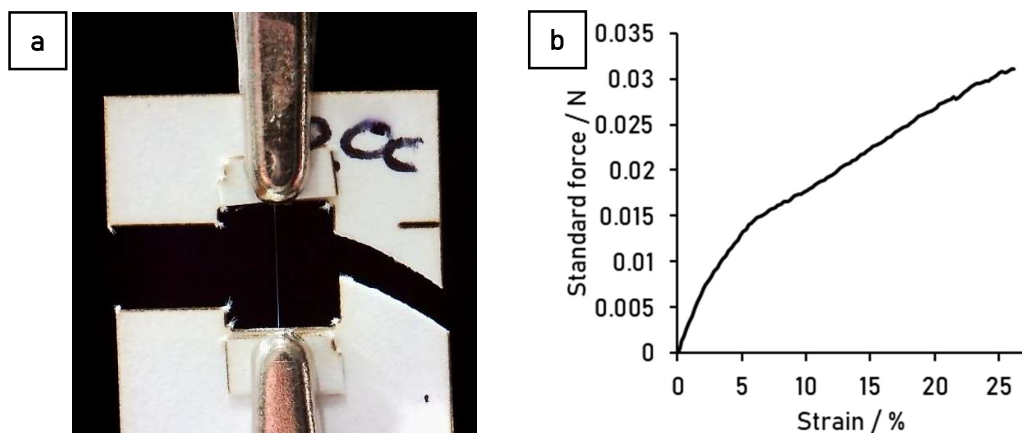
Figure 3.3: a) Paper card frame with single *Nephila inaurata* dragline fibre b) Exemplary tensile curve

3.2　Materials and sample preparation

HOPG

Highly oriented pyrolytic graphite (HOPG) was used as a reference carbon material for investigations into the effect of dose and dose rate on the growth of a contamination layer (Chapter 5, section 5.1.2.4). It is also used as a reference carbon material to compare HeIM SE spectra to those collected in the SEM (Chapter 4).

It was purchased from Agar Scientific with a mosaic spread of 3.5 ± 1.5° as a 20 x 20 mm square with approximately 4 mm thickness. For SEM observation, it was applied to an aluminium SEM stub using silver adhesive paint. To obtain a fresh surface it was renewed by applying Sellotape and removing the top layer in a rolling motion around a cylindrical pen. Specific imaging parameters are listed in the figure captions of the respective results.

Carbon fibre

Carbon fibre was used as a reference carbon fibre in Chapter 5 to find optimal imaging parameters for LV-SEM observation of fibres and their cryofracture cross-sections. Its diameter is on the same scale as that of *Nephila* dragline silk.

A bundle of carbon fibre was kindly supplied by Simon Hayes and Matthew Collinson of the Department of Materials Science and Engineering at the University of Sheffield (**Figure 3.4 a**). The polyacrylonitrile-based carbon fibres used were Toho Tenax Besfight® G30-500 12k HTA 7C EP03. The diameter is 7 μm and the electrical resistivity is specified at 1.50 x 10^{-3} Ω cm^{-2}. For cryo-fracture two thin rectangular silicon wafer fragments (approximately 5 mm x 2 mm) were pre-cleaved with a diamond scribe in the middle of their length to control where they fracture. A bundle was cut to 20 mm and applied to a silicon wafer fragment using silver adhesive paint (Agar Scientific). Silver adhesive paint was applied to the second rectangular Si fragment and applied on top, to result in a Si-carbon fibre-Si sandwich with silver paint as the matrix. The conductive paint was left to dry overnight. For cryo-fracture, the 'sandwich' was immersed in liquid nitrogen, left to reach temperature until the boiling of the liquid nitrogen had subsided, and then snapped using forceps. The fracture surfaces of both halves were prepared for SEM observation by attaching the non-fractured edge of the Si rectangle to an aluminium stub and fixing it in place using silver adhesive paint, so that the fractured edges were observable top-down in the SEM. There was visible pull-out of the silver and carbon fibre from in between the silicon, however the carbon fibres themselves fractured cleanly to result in circular cross-sections.

| Carbon fibre | Ramie plant fibre (*Boehmeria nivea*) |

Figure 3.4: a) Carbon fibre and b) Ramie plant fibre (*Boehmeria nivea*) reproduced from [7] under a CC BY 4.0 licence (https://creativecommons.org/licenses/by/4.0/)

Ramie plant fibres

Ramie nettle plant fibres are significantly larger than spider silk but exhibit similar charging behaviours and beam-sensitivity compared to spider silk. It may also be considered a complex hierarchical polymer due to its multi-scale structuring. In this work, SEM observations of Ramie fibres demonstrate the importance of scanning patterns in Chapter 5, section 5.1.2.3.

Ramie nettle plant fibres (*Boehmeria nivea*) were kindly supplied by Sameer Hamad of the Department of Materials Science and Engineering here at the University of Sheffield and were originally purchased from Wild Fibers store (Birmingham, UK) and were used as received (**Figure 3.4 b**). Individual fibres were mounted on an aluminium SEM stub by attaching both ends with silver adhesive paint at the edge of the stub. SEM observation took place in the Nova NanoSEM450 using imaging parameters as specified in the relevant figure captions.

Spider silk

The spider silk investigated in this work comes from two species in the *Nephila* genus, which are tropical orb-weaving spiders. There is a significant body of research on *Nephila* silk, in part because it is known that the dragline silk used in their orb-webs has favourable mechanical properties. In addition, the females of this genus can grow to the size of a human palm (including the legs), which makes handling of the spider and identification of the different silk glands under the microscope significantly easier, compared to smaller native orb-weavers.

***Nephila inaurata* dragline silk**

Nephila inaurata dragline silk was used for the investigation of tensile mechanical properties variation with different reeling speeds, and its further relation to nanostructure size and distribution (Chapter 7).

A *Nephila inaurata* female (**Figure 3.5 a**) was purchased as a juvenile form an arachnids breeder (Polyped, Germany). The specimen was kept in the lab environment, watered and fed brown crickets and waxworms. Once mature, force reeled dragline silk was collected as follows: the spider was transferred into a closed but not sealed plastic box. A flask of dry ice was submerged in water and the subliming CO_2 gas was fed into the spider's box through a tube to sedate the spider. The spider was exposed to the CO_2 environment for approximately 5 min before it was taken out and gently fixed to a Styrofoam block using pins as brackets to restrict the movement of the legs without harming the spider (**Figure 3.5 b**). The spider was left to come to, and any potential aftereffects of the CO_2 exposure were allowed to dissipate by letting 30 minutes pass before the first silk was collected onto a speed-controlled reeling frame [8].
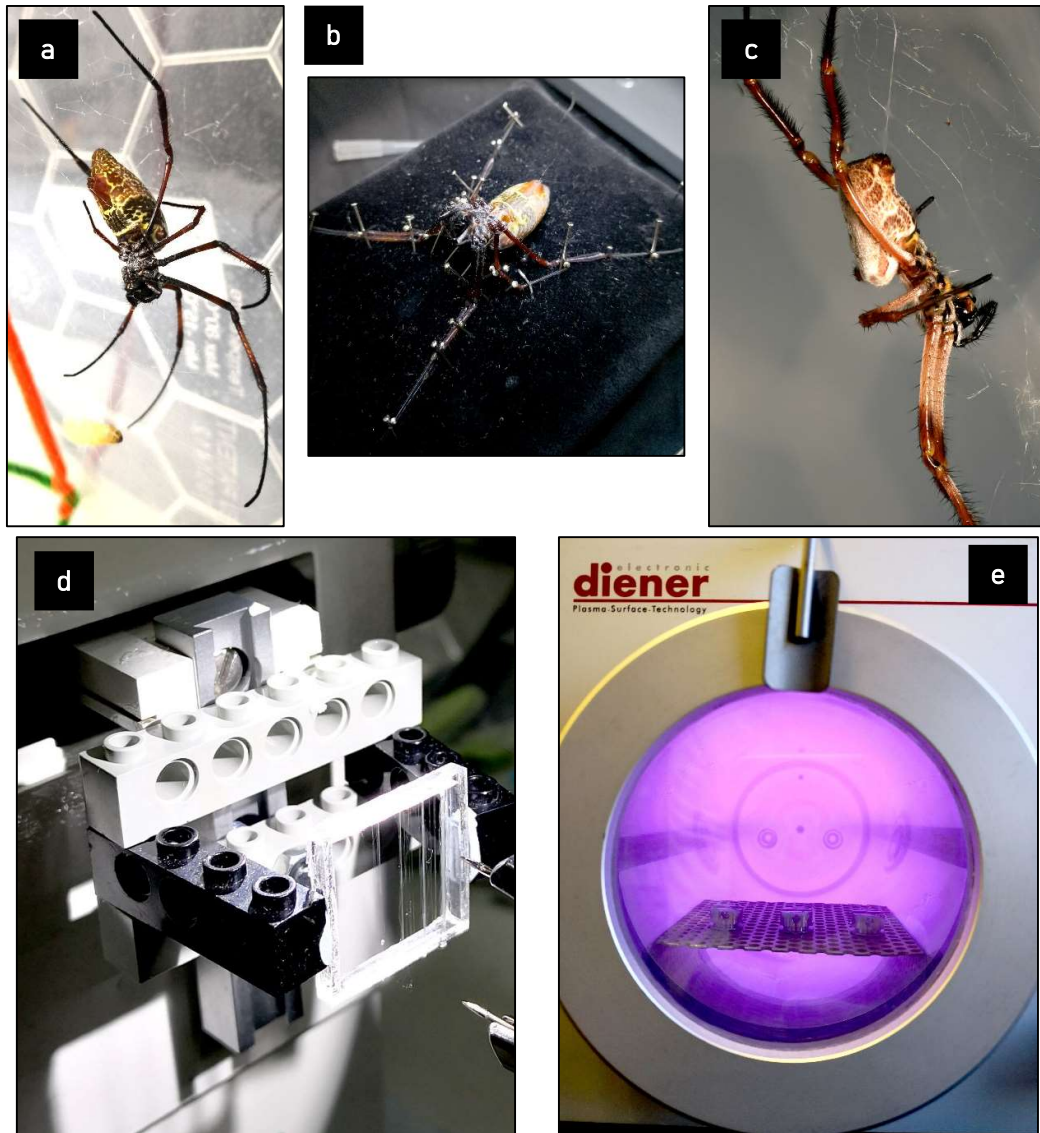
Figure 3.5: Spider silk collection and preparation. a) Mature *Nephila inaurata* female b) Fixated *Nephila inaurata* female ready for forced reeling of dragline silk c) Mature *Nephila edulis* female courtesy of Fritz Vollrath and Alex Greenhalgh of the University of Oxford Zoological Department Silk group d) *Nephila* dragline silk on a 20 x 20 mm polyacrylic frame e) *Nephila* silk on SEM stubs subject to ex-situ non-thermal atmospheric plasma treatment

Nephila edulis dragline silk

Nephila edulis silk was to establish a workable set of SEM imaging parameters as detailed in Chapter 5 and was furthermore used when trying to expose cross-sections of the silk fibres by different methods of fracture, detailed below and further discussed in Chapter 6.

Force reeled female *Nephila edulis* (**Figure 3.5 c**) dragline silk was collected by the Oxford Silk Group courtesy of Fritz Vollrath and Alexander Greenhalgh using the process described above. The silk was reeled onto 20 x 20 mm polyacrylic frames for further sample preparation as required (**Figure 3.5 d**).

In the process of optimising imaging and sample preparation some *Nephila edulis* fibres were cryo-fractured and subsequently imaged at room-temperature, while other samples were both fractured and imaged at liquid nitrogen temperatures in the specialised cryo-SEM system described in section 3.1.1.1.

Cryo-SEM preparation of spider silk

The spider silk cryo-SEM samples were prepared using the Quorum PP3010T preparation system, which is an attachment to the Helios SEM supplied by Quorum Technologies Ltd. A *Nephila* silk bundle of a defined reeling speed kept under tension by a polyacrylic frame (**Figure 3.5 d**) was applied along a thin rectangular silicon wafer fragment (approx. 2 x 5 mm) with carbon adhesive tape on both ends as a support. A conductive cryofracture matrix was prepared by mixing a 1 to 1 volume ratio suspension of cryo-glue (Tissue-Plus optimal cutting temperature compound, Scigen Scientific, CA, USA) and colloidal graphite (G303, Agar Scientific). The silk bundle (approx. 50 fibres) on the silicon support was covered in a thin layer of cryo-glue/graphite suspension before another silicon rectangle was applied to sandwich the silk bundle. The fibre ends were cut using a scalpel and the sample was mounted upright into a cross-sectional aluminium SEM sample holder before submerging in a liquid nitrogen slush, letting the sample equilibrate until the liquid nitrogen reservoir went placid. The sample was transferred to the evacuated cryo-preparation chamber (kept at -180 °C) through a vacuum lock and was cleaved using a knife in the preparation chamber (**Figure 3.1 c**). A subliming procedure was performed in the preparation chamber, in which the sample was warmed to -70 °C while a cold-finger (or anti-contaminator) was kept at -190 °C to

remove any surface ice which could interfere with imaging, before letting the sample return to –180 °C once again and directly transferring the sample into the SEM chamber for imaging (also held at –180 °C by the Quorum cryo–SEM system) through another vacuum lock.

To enhance adhesion between the cryo–glue/graphite matrix and the silk fibres, some fibre bundles were exposed to reactive oxygen plasma before embedding and cryo–fracturing as described above. The fibre bundles were plasma treated in a 40 kHz, 100 W and 0.3 mbar air plasma using a Zepto plasma cleaner (Diener electronic, **Figure 3.5 e**). The plasma treatment time totalled 8 minutes in 2 minutes stages to allow cooling between treatments. The effect of this plasma on the surface morphology and etching of the fibre is discussed further in Chapters 6 and 7 [9].
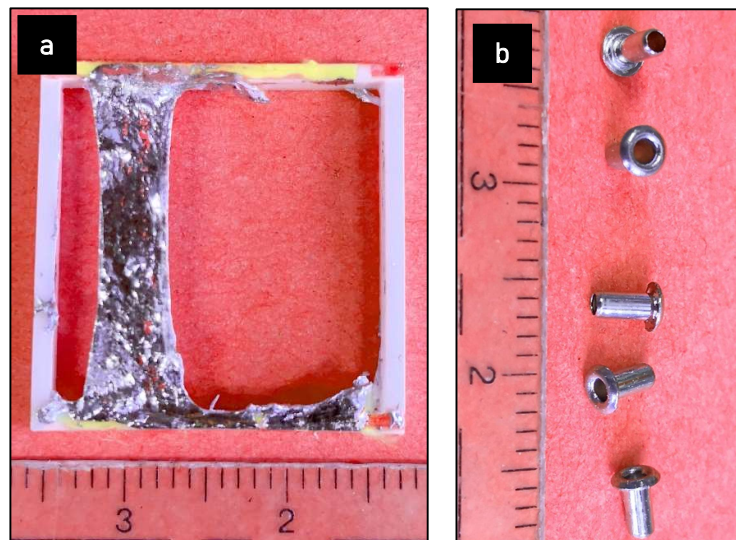

Figure 3.6: a) Acrylic frame with Field's metal encased *Nephila edulis* spider silk b) eyelets used in cryofracture.

Cryo-snapping for room temperature imaging of spider silk

For cryo-fracture with subsequent room temperature imaging fibre bundles were embedded into low melting point Field's metal [10] (Agar scientific, melting point = 62 °C) on a hotplate set at 70 °C (**Figure 3.6 a**). After solidification the encased fibre bundles could be cut away from the polyacrylic support frames into approximately 10 mm rods and were easily handled. For cryo-fracture, the metal coated fibre bundle was threaded through two copper eyelets with an inner diameter of 2.5 mm and a rim of approximately 4 mm diameter (**Figure 3.6 b**), with the rims touching each other. The eyelet was filled with silver adhesive paint to serve as a matrix to the metal encased bundle within the eyelet and to attach both eyelets to one another. The silver paint was left to dry overnight. The eyelets were immersed into liquid nitrogen using forceps and left to reach equilibrate until the boiling had subsided. The two eyelets were snapped apart and retrieved separately from the liquid nitrogen, immediately exposing them to a stream of dry argon gas to prevent condensation forming on the fracture surface. The eyelets were applied to an aluminium SEM stub using silver adhesive paint to allow top-down observation of the fracture surface at room temperature.

Peacock feather sections

Feathers are a further example of a complex natural hierarchical polymer. The main structural protein keratin makes for a more brittle and higher modulus structure compared to silk, which lends itself better to simple sectioning techniques, such as the one detailed below. The iridescent barbules of male peacock feathers were chosen due to their distinct position and arrangement of melanosomes at the edge of the barbule. Chapter 6 investigates the possibility of distinguishing the melanin-rich outer edge of the barbule from the keratin-dominated centre using secondary electron spectroscopy and spectral imaging.

Male *Pavo cristatus* decorative tail feathers were purchased from a homecrafts store (Hobbycraft Sheffield, **Figure 3.7 a**). Below the eye where the feather is an iridescent blue, brown and green, an approximately 20 x 10 mm section was cut with the feather shaft in the middle using a sharp blade (**Figure 3.7 b**).

A conductive sectioning matrix was produced as follows: Silver adhesive paint (Agar scientific) was dissolved in acetone and Büchner filtrated to isolate the resulting silver powder on a filter paper. The powder was dried at 60 ˚C and weighed for reference. Polycaprolactone (PCL), a low-melting point thermoplastic, was melted in a petri dish at 70 ˚C before adding 10 % wt./wt. of silver powder and mixing well into a homogenous suspension with a wooden toothpick.
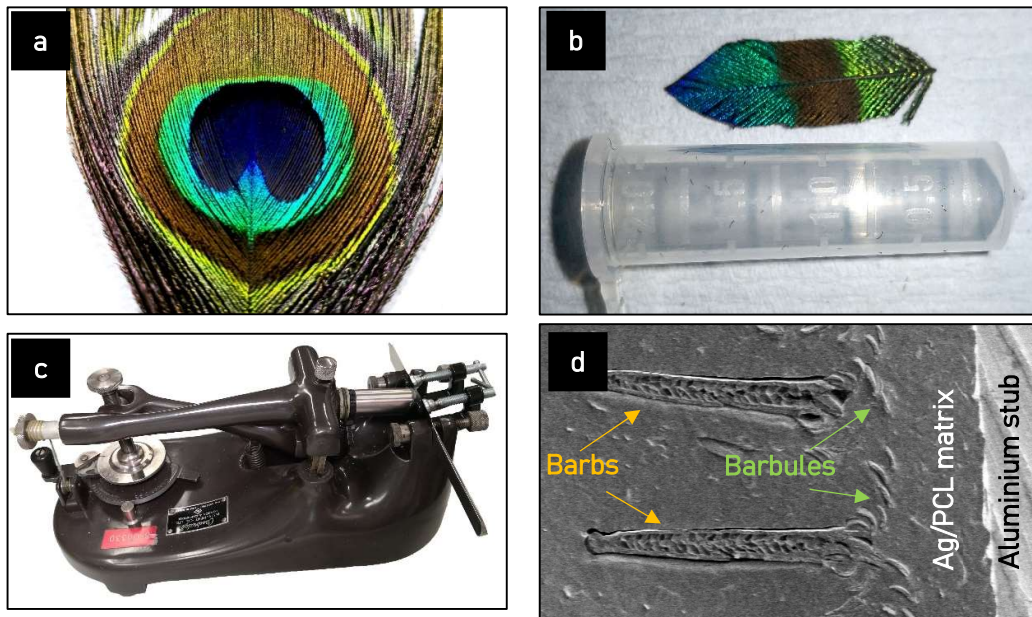
Figure 3.7: a) Eye of a decorative male peacock feather (*Pavo cristatus*) b) cut iridescent section of eye with 2 ml centrifuge tube for PCL embedding c) Bench microtome d) SEM overview of sections showing feather barbs (large horizontal structures) and iridescent barbules (smaller crescents to the left of the barbs)

The feather section was placed inside a 2 ml centrifuge tube (**Figure 3.7 b**) and the solid PCL/Ag mixture was added. The thermoplastic was melted in a vacuum oven at 70 ˚C for approximately 1 h to cover the feather section, and the oven was evacuated to

eliminate air-bubbles inside the thermoplastic for approximately 4 h. Once removed from the oven and cooled, the centrifuge tube was cut away to yield the feather embedded in the solid PCL/Ag in a cylindrical pellet. The pellet end was carefully attached onto the sample holder of a rocking bench microtome (Cambridge Instrument Co,, Ltd., **Figure 3.7 c**) by partially melting on one end, and sections of approximately 65 μm thickness were cut using a fresh razor blade. The circular sections were applied to an aluminium SEM stub ready for observation, of which an SEM overview is shown in **Figure 3.7 d**: the iridescent pigmented structures of interest are situated within the feather' barbules, which extend from the feather's barbs.

Where specified, the feather sections were subject to 3 minutes of an in-situ plasma cleaning procedure within the Helios SEM chamber. According to the manufacturer's specifications, the plasma source generates a reactive oxygen plasma at approximately 0.5 mbar. It removes hydrocarbon layers on samples and vacuum parts by generating gaseous CO, CO_2 and H_2O species, which can be pumped away.

3.3 References

1.   I. Konvalina, F. Mika, S. Krátký, E. Materna Mikmeková and I. Müllerová: *In-Lens Band-Pass Filter for Secondary Electrons in Ultrahigh Resolution SEM*. Materials (Basel). **12**, 2307 (2019).

2.   Y. Zhou, D.S. Fox, P. Maguire, R. O'Connell, R. Masters, C. Rodenburg, H. Wu, M. Dapor, Y. Chen and H. Zhang: *Quantitative secondary electron imaging for work function extraction at atomic level and layer identification of graphene*. Sci. Rep. **6**, 21045 (2016).

3.   P. Kazemian, S.A.M. Mentink, C. Rodenburg and C.J. Humphreys: *Quantitative secondary electron energy filtering in a scanning electron microscope and its applications*. Ultramicroscopy **107**, 140–150 (2007).

4.   N. Stehling, R. Masters, Y. Zhou, R. O'Connell, C. Holland, H. Zhang and C. Rodenburg: *New perspectives on nano-engineering by secondary electron spectroscopy in the helium ion and scanning electron microscope*. MRS Commun. **8**, 226–240 (2018), doi:10.1557/mrc.2018.75.

5.   J. Schindelin, I. Arganda-Carreras, E. Frise, V. Kaynig, M. Longair, T. Pietzsch, S. Preibisch, C. Rueden, S. Saalfeld and B. Schmid: *Fiji: an open-source platform for biological-image analysis*. Nat. Methods **9**, 676 (2012).

6.   M.W. Berry, M. Browne, A.N. Langville, V.P. Pauca and R.J. Plemmons: *Algorithms and applications for approximate nonnegative matrix factorization*. Comput. Stat. Data Anal. **52**, 155–173 (2007).

7.   S.F. Hamad, N. Stehling, S.A. Hayes, J.P. Foreman and C. Rodenburg: *Exploiting Plasma Exposed, Natural Surface Nanostructures in Ramie Fibers for Polymer Composite Applications*. Materials (Basel). **12**, 1631 (2019), doi:10.3390/ma12101631.

8.   C. Riekel, M. Rössle, D. Sapede and F. Vollrath: *Influence of CO2 on the micro-structural properties of spider dragline silk: X-ray microdiffraction results*. Naturwissenschaften **91**, 30–33 (2004), doi:10.1007/s00114-003-0482-8.

9.   N.A. Stehling, K.J. Abrams, C. Holland and C. Rodenburg: *Revealing spider silk's 3D nanostructure through low temperature plasma etching and advanced low-voltage SEM*. Front. Mater. **5**, 84 (2018).

10.   S.Q. Field: Gonzo gizmos: Projects & devices to channel your inner geek, (Chicago Review Press, 2002).

4 New Perspectives on Nano-engineering by Secondary Electron Spectroscopy in the Helium Ion and Scanning Electron Microscope

Nicola Stehling[1], Robert Masters[1], Yangbo Zhou[2], Robert O'Connell[3], Chris Holland[1], Hongzhou Zhang[3], Cornelia Rodenburg[1]

[1] University of Sheffield Faculty of Engineering, Material Science and Engineering, Sheffield, S1 3JD, UK
[2] Nanchang University, School of Material Science and Engineering, Nanchang, Jiangxi, 330031, China
[3] University of Dublin Trinity College, School of Physics, Dublin 2, Ireland

4.1   Contributions

This publication was an invited contribution in response to a request for a forward-looking 'prospective' review to the journal MRS Communications. As the first author I conducted a comprehensive literature review of past and recent developments in line with the specification of the article type. I wrote all drafts and thus the majority of text and I coordinated receiving my co-author's feedback and incorporating their comments into the final version. I handled submission and review of the paper on the publisher's online system.

Of the novel data presented figures 2, 4, 6b, 6d, 7b and 7d present results of experiments which I designed in close collaboration with Conny Rodenburg and conducted independently. Figures 1c, 3, 5, 6a, 6c, 7a, 7c and 8 are the result of Robert Masters work, whereby I actively contributed to incorporating these results into a coherent discussion within the text and within the context of existing literature.

I produced all figures, except for figure 5 which was produced by Robert Masters. Where figures and images have been taken from other sources, this has been indicated accordingly in the figure captions.

The copyright lies with the publisher; however, the copyright agreement states that I "may reproduce the article or an adapted version of it in any volume of which you are editor or author. Permission will automatically be given to the publisher of such a volume, subject to normal acknowledgement."

Please see overleaf for the published paper.

New Perspectives on Nano-Engineering by Secondary Electron Spectroscopy in the Helium Ion and Scanning Electron Microscope

Nicola Stehling[1], Robert Masters[1], Yangbo Zhou[2], Robert O'Connell[3], Chris Holland[1], Hongzhou Zhang[3], Cornelia Rodenburg[1,]*

[1] University of Sheffield Faculty of Engineering, Material Science and Engineering, Sheffield, S1 3JD, UK

[2] Nanchang University, School of Material Science and Engineering
Nanchang, Jiangxi, 330031, CN

[3] University of Dublin Trinity College, School of Physics, Dublin 2, IE

[*] C.Rodenburg@sheffield.ac.uk

Abstract

The helium ion microscope (HeIM) holds immense promise for nano-engineering and imaging with scope for in-situ chemical analysis. Here we will examine the potential of Secondary Electron Hyperspectral Imaging (SEHI) as a new route to exploring chemical variations in both two and three dimensions. We present a range of early applications in the context of image interpretation in wider materials science and process control in ion beam based nano-engineering. Necessary steps for SEHI in the HeIM to evolve into a reliable technique which can be fully embedded into nano-engineering workflows are considered.

Introduction

The HeIM as a Ground-breaking Focused Ion Beam Microscope

As early as 1948 an ion microscope mass-spectrometer for the in-situ observation of chemical processes at very low magnifications was proposed [1] and the vast potential for helium (He) ions for the generation of patterns with high aspect ratio was reported in the 1979 [2]. In spite of demand from the characterisation and patterning communities, the first commercial HeIM with a high brightness source and high-resolution imaging became available to the scientific community only in 2006. This may be surprisingly late considering that charged particle guns and lenses can be considered mature technologies with decades of application in scanning electron microscope (SEM) and focused ion beam (FIB) instruments among others. While the gas field ionisation source (GFIS) and liquid metal ionisation source (LMIS) were both pioneered around the mid-1970s [3–6], the LMIS enabled the development of microscopes with ion-milling and microscale machining capabilities, which rather quickly found application within the semiconductor industry and were subsequently developed as a commercial technology. The prevalence of SEMs and FIBs utilising LMISs meant that there was initially little benefit

in developing GFIS microscopes, as they were inferior to SEMs in resolution and microanalysis tools and had no obvious advantage for micromachining due to the low sputter yield of lighter noble gas ions compared to the commonly used Ga$^+$ FIBs.

An exciting new chapter in the development and use of ion microscopes began with the availability of a new type of HeIM gas field ionisation source, which is sometimes called ALIS after the corporation which initially developed it. It is the key innovation which enables imaging resolution and nano-engineering precision superior to SEM and FIB microscopes. In a process proprietary to Carl Zeiss a metal tip used to ionise the surrounding He gas can be shaped in situ into a sharp three-atom tip, reducing the number of He$^+$ beams arising from the tip to three and greatly increasing brightness compared to a spherical tip. One of the three He$^+$ beams is selected to result in a bright He$^+$ beam with an origin confined to the angstrom scale, resulting in a very low convergence angle, low energy spread and sub-nanometre lateral resolution [7]. As in FIBs, the different signals arising from beam-sample interactions allow scanning HeIM imaging, and while there is potential for sub-nanometre resolution, the need to limit dose effects such as sample modification by the He$^+$ beam may in some cases be the resolution limiting factor. The beam current can be readily controlled by the feed gas pressure. More recently, the feed gas can be exchanged from He to Ne to produce a focused Ne$^+$ beam for nanoscale fabrication and imaging in the same instrument [8,9], allowing more versatile nanofabrication.

Nanofabrication Capabilities

He$^+$ and Ne$^+$ Milling

With the HeIM currently offering the most highly focused scanning ion beam, nanomanipulation experiments with ever smaller resolution and nanoscale control have been trialled. Nanoscale milling has been successful especially for thinned and 2D materials: It has been shown that high incidence angle He$^+$ polishing of Ga$^+$ FIB prepared TEM lamella leads to a reduction of the surface roughness and a decrease in the Ga$^+$ contamination while keeping the Si crystal structure intact, which is promising for applications in which the Ga$^+$ implantation would pose a problem [10]. Furthermore, nanoscale milling has been successful for graphene [11–13] and molybdenum sulfide (MoS$_2$) [14]. In studies where a bulk material or a substrate is present, Ne$^+$ is usually the ion of choice due to its higher sputtering yield and smaller implantation depth [15]. It has successfully been used in the milling of soft (**FIG. 1**) [16] and semiconductor materials [17]. While Rzeznik *et al.* point out that polymers, and therefore presumably other soft materials, have a density small enough for implanted He, Ne or Ar to escape, preferential sputtering of certain atoms can lead to a change in the surface chemistry if beam exposures are too high [18]. Hence, a chemical analysis tool could monitor surface chemistry in-situ to allow control over undesired modifications that could be detrimental to the final application.
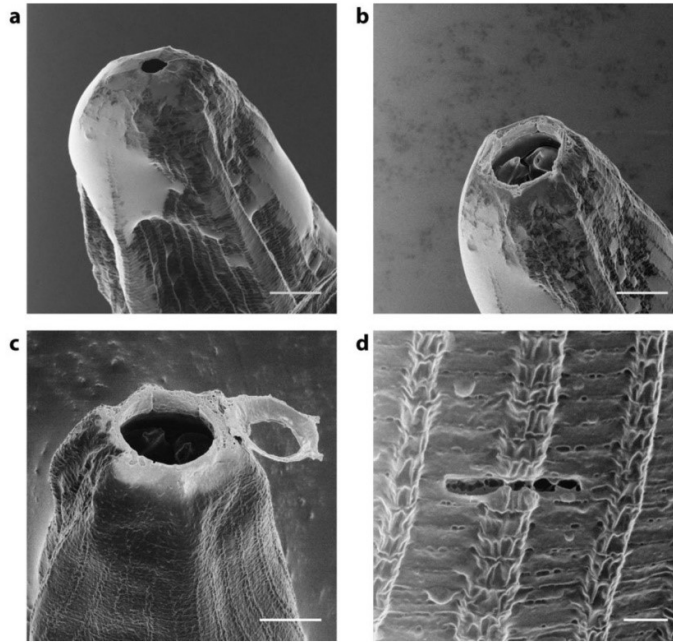
FIG. 1: Ne+ milling of uncoated Pristionchus pacificus **(a)**, a predatory worm with teeth which are only revealed trough Ne+ milling **(b, c, d)**. Scalebars represent 5 μm **(a-c)** and 1 μm **(d)**. Reprinted by permission from Ref. 16 (Springer Customer Service Centre GmbH: Springer Nature, Scientific Reports, 2013)

Sample Modification and Defect Engineering

While there are limitations to the milling ability of He$^+$ ions, the high lateral resolution opens new opportunities for other beam-controlled manipulations of a sample: The control over defects in 2D materials holds great promise in tuning the properties of such materials. Maguire *et al.* have probed defect sizes arising in 2D materials after He$^+$ and Ne$^+$ impact and found that the presence of a substrate greatly influences defect sizes [19]. This suggests that the available volume for ion-sample interaction should be considered as an important factor not only for defect generation, but other beam-sample processes as well. It has been shown that the ion beam can modify resistivity behaviour of MoS$_2$, although the resistivity measurement had to be performed ex-situ [14]. The ability to monitor local electric properties in-situ could ensure precise control or automated feedback loops for such processes, essential for high throughput applications such as patterning.

Resist Patterning and Editing of Nanocircuitry

The benefits of gas ion beams for resist patterning were identified decades ago [2,20]. The large number of secondary electrons emitted from polymers as a result of keV gas ion impact allowed for very fast exposure times. In addition, a much reduced pattern proximity effect compared to electron beam lithography was found [20], enabling high density patterning with lines below 10 nm [21]. Likewise, helium ion beams can be used for nanocircuitry editing as the fabrication of low resistivity 10 nm lines by HeIM has been demonstrated [22].

Outlook for Nanofabrication

Nanofabrication using He^{+} and Ne[+] ions is a very active field and only a handful of examples can be mentioned within the scope of this review. Comprehensive reviews of the potential of gas ion beams for nano-engineering can be found elsewhere [23,24]. The potential for nano-engineered deposited structures for plasmonics, magnetics and sensor applications has been demonstrated in the SEM [25], although challenges remain in dedicated precursor design, avoidance of undesired deposits and slow deposit growth rates. A solution to the latter two challenges could be the replacement of the electron beam by gas ion beams, which would likewise benefit from the development of dedicated precursors. In-situ imaging of local chemical reactions could aid in the surveying of precursors with regards to deposition mechanisms and rates of favourable and unfavourable processes.

Imaging and Microanalysis Capabilities

The high precision of the He^{+} beam has opened doors not only for nanofabrication applications, but also for imaging and microanalysis at ever smaller lateral resolution.

The potential of the HeIM as a microanalysis tool was summarised excellently in 2011 by Joy and Griffin [26]. Compared with FIBs and SEMs, the HeIM has some limitations: Energy dispersive X-ray spectroscopy cannot be performed in the HeIM, due to the increased mass of He^{+} compared to electrons. The He[+] beam voltage would have to be more than three orders of magnitude larger than that required from an electron beam to excite a certain X-ray line for X-ray spectroscopy, which is out of the question for existing HeIM instruments. Furthermore, ion induced secondary electron (iSE) emission total yields cannot quantifiably be assigned to specific elements due to scatter in the relationship between atomic number and total iSE yield [27]. Finally, the increase in lateral resolution achievable for iSEs is not available for backscattered He (BSHe) signal due to its larger lateral spread in the interaction volume [28]. While the analysis of BSHe within Rutherford backscatter spectroscopy (RBS) offers energy and angular resolution in some HeIM instruments suitable for elemental mapping [29,30], it does not serve to exploit the benefit in lateral resolution given by the superbly focused He^{+} beam.

These limitations have spurred on efforts to explore and develop other microanalysis tools in the HeIM. One advantage of BSHe over backscattered electrons (BSE) is their sensitivity to the ion channelling effect within crystalline samples. Veligura *et al.* have demonstrated that the ion channelling effect visible in both iSE and BSHe imaging within the HeIM can be used in polycrystalline samples to map crystal orientation as a method in direct competition with EBSD, without the need for complex mathematics to interpret the signal [31] (**FIG. 2**).
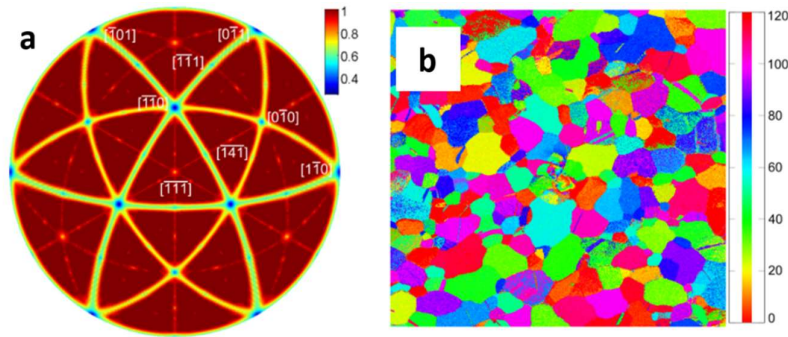
FIG 2: Simulated map of backscatter probability of He$^+$ atoms by crystallographic orientation in gold (**a**) and orientation map of Au grains (**b**). Resized from [31] under a CC BY 2.0 licence (https://creativecommons.org/licenses/by/2.0/)

When considering how to further develop microanalysis tools in the HeIM, secondary ion mass spectrometry (SIMS) must be considered. The mass analysis of secondary ions generated from ion impact is developed as a microscopic technique with very high sensitivity, depth resolution and the opportunity to map secondary ion species, while simultaneously sputtering the surface to extract 3D information [32]. SIMS detects secondary ion fragments by their mass to charge ratio and can thus be used for mapping of elements and chemical species if characteristic fragment ions are known. The development of the GFIS used in the HeIM holds the promise of higher lateral resolution for SIMS microscopy due to the smaller ion spot size [33]. HeIM-SIMS capable instruments are currently realised by extracting the secondary ions from the chamber through a transfer tube into the mass spectrometer using a 500 V extraction field [34]. Ideally, a SIMS mass analyser within a HeIM would allow iSE, RBS and SIMS measurements from the same area to allow correlative spectroscopy and gain the maximum data volume from a HeIM experiment. At present, sequential acquisition of iSEs and secondary ions is possible, yielding elemental SIMS maps overlaid on iSE images with significantly higher resolution than EDX elemental maps obtainable in the SEM [34,35]. The imaging mode can be changed to rapidly switch between iSE and SIMS imaging, however optimal resolution SIMS-iSE maps are only possible when exchanging the feed gas, which takes significantly longer. This is because on one hand SIMS favours the higher secondary ion yield associated with Ne$^+$ bombardment and on the other hand higher resolution iSE images can be achieved with the He$^+$ beam. Simulations by Wirtz *et al.* suggest working parameters based on sputter yields for He$^+$ and Ne$^+$ SIMS experiments and propose that Ne$^+$ ions may be used for depth profiling to gain access to 3D SIMS maps while using the extreme surface sensitivity of SIMS to an advantage [15,33]. While the elemental mapping of inorganic species has been realised [36,37], the mapping of local chemistry on the nanoscale for materials of complex shapes and structures has yet to be demonstrated and may be ultimately limited by the relatively low secondary ion yields, or the need for reactive gases such as oxygen to increase yields.

Secondary Electrons in the Helium Ion Microscope

SE emission in the HeIM is the signal with the highest yield and spatial resolution. The detection is routinely performed using an Everhart-Thornley detector (ETD), which has decades of application in SEMs [38].

Long before the emergence of the HeIM as a precision tool, ion induced secondary electron emissions were studied from the 1970s with applications of ion-beam milling and secondary ion mass spectrometry (SIMS) imaging in mind [39]. A comprehensive review by Lai *et al.* summarises the theoretical models developed up to 1986 [39]. While Parilis and Kishinevskii suggested that SE emission occurred through kinetic excitation of the substrate with subsequent relaxation through Auger electron emission, Baragiola *et al.* contested the theory with experimental evidence and suggested a direct excitation of valence electrons arising from impact of the incident ions [40,41]. While the semi-empirical SE emission theories summarised by Liu are still in use today, more modern approaches commonly use Monte-Carlo simulations to extract spatial information about the emitted SEs [27].

Ramachandra *et al.* point out that the stopping power dependence on particle incident velocity is very similar when comparing electrons and He^+ ions. However, while He^+ ions and electrons have equal and opposite charge, they have a significantly different mass which means that the stopping power of a 30 keV He^+ beam is significantly larger than that of a 1 keV electron beam (ca. 20 and 7 eV $Å^{-1}$ respectively) [27]. This is at the base of the high secondary electron yields (SEYs) achievable in the HeIM compared to the SEM. SEMs are usually operated above the maximum stopping power voltage of 0.1 keV and thus reducing accelerating voltage increases stopping power and SEY – a principle utilised in LV-SEM. Conversely, HeIM ion energies lie below the maximum stopping power of about 900 keV and so even higher SEYs can be expected as higher energy He^+ beams become available to the community [27].

In efforts to benchmark the HeIM against the SEM with regards to their SE signal, various materials have been studied to assess whether known limitations of current systems can be overcome in the HeIM.

Lateral Resolution

With the HeIM's potential to produce He^+ spot sizes as small as 0.25 nm [42], the spatial origin of the iSE signal has been investigated in more recent studies. Notte *et al.* use Monte-Carlo simulations to compare the interaction volume geometries of Ga^+, He^+ and electron beams [43]. In comparison, the He^+ beam stays more confined while travelling further into the sample. Most remarkably, the interaction volume is highly localised within the SE escape depth. The favourable geometry of the interaction volume of He^+ ions is due to the absence of strong electron-electron scattering events which lead to fraying of the electron beam interaction volume close to the surface [43].

The increase in lateral resolution compared to the SEM is exciting especially for uncoated insulators. In studies of mammalian cells, it was shown that metal coatings obscure important surface detail both in the HeIM and SEM, while HeIM of uncoated samples at 25-35 kV offers superior lateral resolution without charge build-up and artefacts which prohibit high resolution SEM imaging of such materials [16,44–48]. The absence of a conductive coating for the imaging of insulators reveals previously unobservable surface structure [47] and contrast [44] which allows further insight into the nanostructure of complex materials through high resolution imaging. Additionally, the absence of a conductive coating unlocks access to the real sample surface and may lead to new systematic investigations of such materials if suitable in-situ chemical analysis tools are available.

Depth Resolution

Like SEM, HeIM must be considered a surface sensitive technique due to the small escape depth of SEs. However this can also be used to an advantage: HeIM SE imaging has shown improvements in the interpretation of image data collected from carbon-chromium nanocomposite due to a higher depth resolution of 4.8 nm compared to a scanning transmission electron microscopy (STEM) depth resolution of about 13 nm [49]. In this case the higher lateral resolution available in the HeIM allows it to compete with high resolution bulk probing techniques, such as STEM or transmission electron microscopy (TEM).

Charging Behaviour

Sample charging behaviour of insulators under charged particle beams can be rather complex. Not only the current of the beam determines sample charge build-up, but also the charge dissipation mechanisms into ground, as well as the total yield of charged secondary particles emitted into vacuum, i.e. secondary electron or ion yields. Depending on the incident beam energy, negative as well as positive charging can be observed in the SEM [50,51]. In an effort to manage charging, crossover primary beam energies are sought in which positive and negative charging are in balance. However, charging is not always homogenous over the field of view and a dynamic charge balance may be unattainable resulting in degradation of image quality. In the HeIM the low secondary ion yield of the beam means that charging of insulating samples is generally positive [33]. HeIMs are fitted with an electron flood gun, which provides a charge compensation mechanism without introducing any additional chemical species during imaging. The electron flood gun is used in imaging of uncoated insulating samples [48], and has also been shown to counteract gradual positive charge build up in doped silicon samples [52,53]. This is important as a positive charge build-up will otherwise reduce the SE yield and counteract the favourable high SE signal output in the HeIM. While unfavourable for iSE imaging, this iSE signal reduction with increase positive charge build-up was exploited by Iberi *et al*. to assess the magnitude of charge compensation possible through HeIM machined nanoscale contacts, and thus their conductivity [54].

Secondary Electron Energy Distribution

While much attention has been paid to the high total iSE yield, the iSE energy distribution has been investigated relatively little. In separate studies Petrov *et al.* and Ohya *et al.* have compared the iSE spectra of metals in the HeIM and SEM and noted a difference in the position and width of the most intense peak [55–58]. This difference is attributed to a different material response to the impinging He$^+$ ions compared to electrons, as external environmental factors, specifically pressure, are comparable between HeIMs and SEMs. In a study of different metals within an Ar$^+$ beam microscope it was shown that the iSE energy distribution of different metals are distinct and repeatable [59], making mapping of pure elements and also mixed phases possible in certain energy windows if reference spectra are known, as previously demonstrated in the SEM [60].

In-Situ Secondary Electron Spectroscopy: Experimental Considerations

Electron spectroscopy is widely performed to obtain compositional and electronic information about a sample. Most techniques, such as Auger spectroscopy (AS), electron energy loss spectroscopy (EELS), photoelectron spectroscopy (PES) and low electron energy spectroscopy (LEES) are available as microscopic techniques with varying lateral and energy resolution. The idea of secondary electron spectroscopy (SES) within charged particle microscopes is as old as the microscopes themselves, however it was recognised very early that contamination layers greatly influence the secondary electron energy distribution and complicate any qualitative or quantitative evaluation of the spectra [61]. Nevertheless, its potential usefulness to materials science was demonstrated by linking spectral features to the degree of ordering in carbon fibres to modulus and treatment regime [62]. Furthermore, Joy *et al.* demonstrated that the effects of contamination in secondary electron spectra could be managed in an Auger microprobe under SEM conditions on a wide range of inorganic materials [63]. The study also demonstrated that there is fine structure in the SE spectra which is not accurately modelled by the Chung and Everhart model for SE emission of metals [64], and could have potential in SEM microanalysis. Another promising application of SE spectroscopy was found in the enhancement of dopant contrast of doped silicon. In experiments directly relevant to the semiconductor industry the use of secondary electron hyperspectral imaging (SEHI) has shown to enhance the dopant contrast to an extent where the dopant concentration is directly quantifiable by the SE emission within a certain energy range [65,66]. The ability to capture multiple doped areas of certain concentrations in one image makes the technique efficient. This approach has been shown to be successful not only in the SEM, but also in the HeIM if the electron flood gun is used to control sample charging effects [52,53,67,68].

While SE micrographs are intuitively understood by the human eye in the presence of edge contrast and shadowing, quantitative analysis of SE images remains a challenge even today. To better understand the make-up of a SE image, SEs have been classified as to the process from which they have emerged [51]: SE1 are the result of the first inelastic interaction of the incident beam, be it He$^+$ or electrons, with the sample electrons. Due to the absence of a cascade of interactions before the SE1 is generated, this is the signal with the highest spatial resolution. SE2 arise from backscattered electrons or ions which by following along a cascade of interactions undergo an inelastic scattering event close to the sample surface, but at a distance from the incident beam. All SEs which arise from BSE or BSHe scattering off the instrument, i.e. the chamber or the pole-piece, are classified as SE3. The ratios of said SE categories directly influence spatial resolution of the SE signal and noise levels, whereby obtaining a pure SE1 signal would be the ideal. However, separation of the different signals to achieve an image more suitable for quantitative analysis is challenging, not least because the relative fractions of the different SEs seems to vary significantly for both in-chamber ETD and in-lens detection between SEM manufacturers and models, as demonstrated in a comparative study by Griffin [69]. Encouragingly the study did confirm that it is possible for some in-lens detection systems to collect a signal dominated by SE1 based on angular and energy selection, and hence depending on the exact detector design. In the further development of HeIMs and SEMs this need for a better understanding of the SE signal will require investigations to look beyond total yields and at the SE energy distribution collected by the detector. If the detector is well characterised, instrument parameters such as working distance, beam voltage or incident beam angle can be selected for their

influence on the detected SE energy distribution and controlled by the user to reduce instrument variability and select the information that is sought. For example, by selecting low energy SEs, it is possible to exclude the signal arising predominantly from a contamination layer on doped silicon, revealing the dopant contrast underneath [70].
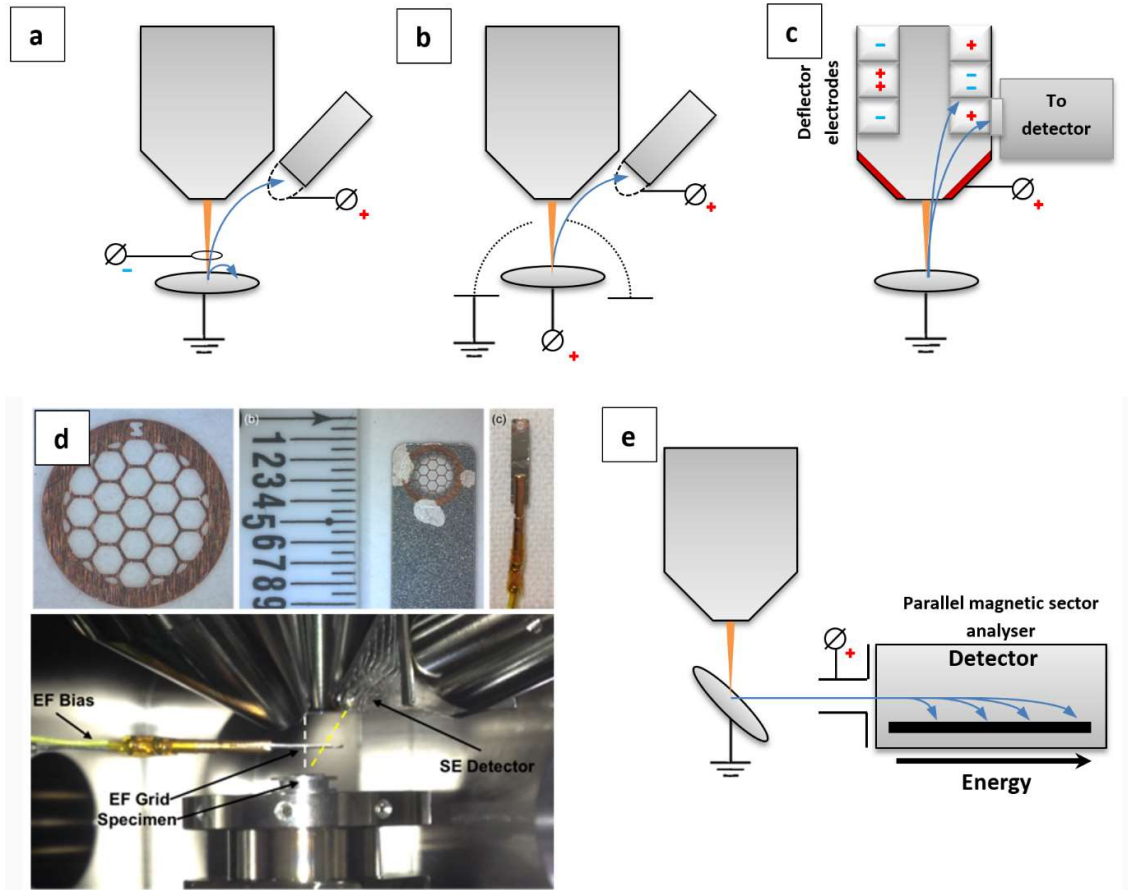

FIG. 3: Energy analyser set-ups. **a)** Schematic of the HeIM set-up used in Zhou *et al.* [71] and this work **b)** Schematic HeIM set-up described by Mikhailovskii *et al.*, adapted from [56] **c)** Schematic of SEM in-lens energy analyser as described by Kazemian *et al.* [72] and used in this work **d)** Image of the HeIM energy analyser set-up represented in schematic a **e)** A parallel magnetic sector electron energy analyser as proposed by Khursheed for use in SE spectroscopy, adapted from [76]

If secondary electron spectroscopy within charged particle microscopes is to be developed as a microanalysis tool, the energy analyser characteristics must be understood. **Fig. 3** illustrates currently used and proposed SE analyser set-ups. **FIG. 3 a** and **b** illustrate high pass analysers employed in HeIMs in which the voltage difference between the sample and an inserted grid can be varied to only allow SE above a certain energy to reach the Everhart Thornley detector [56,71]. Conversely, the Nova and Sirion SEM energy analyser illustrated in **c** is a low pass filter, in which a voltage can be applied to electrodes within the pole piece to divert electrons below a threshold energy to an in-lens detector [72]. In the in-lens detection system a suction tube voltage is applied to maximise the yield and angular detection efficiency of SEs, while also excluding SE3.
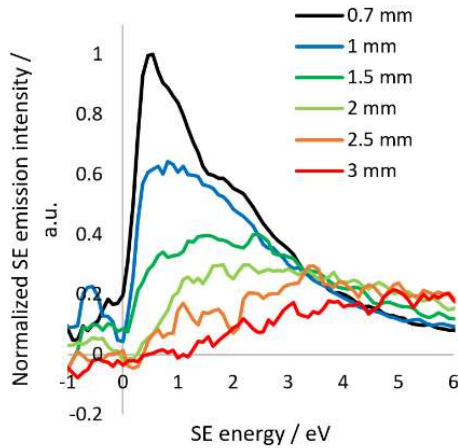
FIG. 4: Influence of sample-grid separation on spectral shape in the Orion NanoFab HeIM on the example of a highly oriented graphite surface. The different spectra are recorded at 30 keV He⁺ and normalised to the dataset.

A limitation of current SE analysers within HeIMs and SEMs is the incomplete understanding of operating parameters which are independent of the sample such as energy resolution, angular collection efficiencies and energy collection efficiencies. Furthermore, these may change with user-controlled parameters, such as working distance and in the case of the detectors illustrated in **FIG. 3 a** the grid-sample separation. The energy filtering grid is mounted on a nanomanipulator arm, whereby the distance between the grid and pole-piece is kept constant for consistency. While moving the nanomanipulator arm with the grid in x and y to obtain the desired field of view, the distances between the components can be determined by focusing on the grid and sample respectively and obtaining the focal length for each at high magnification. The sample stage is translated in z to change the sample-grid separation. It is shown in **FIG. 4** that the sample-grid separation is a critical parameter for spectral acquisition. This effect has also been observed when altering the sample-pole piece separation in the SEM set-up shown in **FIG. 3 b** [73]. However, in the HeIM the sensitivity is much more pronounced in the low energy SE emissions, and furthermore distance measurements using the He⁺ beam can be expected to have a larger uncertainty due its large depth of focus. It is clear that instrumental and working parameters must be known and controlled, as it would be expected from other electron spectrometers such as those used for photoelectron spectroscopy and Auger spectroscopy. A better understanding of these factors in SE energy analysis in HeIMs and SEMs would ensure easier image and data interpretation and reproducibility of measurements.
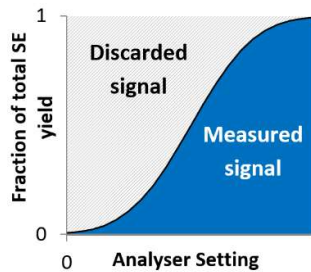

FIG. 5: Schematic of detection efficiency for an energy scanning analyser

A further limitation of the analysers presented in **a-d** is their high or low-pass SE collection. In a spectral acquisition the analyser voltage is scanned to cumulatively collect SEs up to or from an energy threshold. As illustrated schematically in **FIG. 5**, this collection strategy leaves 50% of the SE signal undetected when using a normal distribution as a rough approximation for a SE spectrum. Furthermore, only the image brightness differential contains information about the SE emission at a specific energy, meaning that the fraction of the signal contributing to the measurement can be very small. As a result, the sample is subject to significant beam exposure during a single spectral acquisition, which must be taken into account especially where dose effects such as the He$^+$ beam invasiveness on device structures is of concern [74], or in beam-sensitive biomaterials where high spatial and energy resolution is required for nanoscale analysis [75]. A parallel detection rather than an energy-scanning SE energy analyser would significantly increase detection efficiency and allow the same signal-to-noise ratio of the hyperspectral images at a considerably lower overall beam exposure. Some parallel SE spectrometers for the SEM have been proposed by Khursheed as illustrated in **FIG. 3 e** [76], and the designs would be equally valid for HeIMs.

The integration of microanalysis tools such as a parallel SE spectrometer poses a practical and design challenge. This was noted by Joy and Griffin with regards to SIMS capabilities in the HeIM [26]. However, it has been shown that a SIMS analyser can be coupled to a HeIM by adding the SIMS analyser to the existing hardware of the HeIM using a 500 V extraction field [34]. The same is conceivable for SE spectroscopy, especially since extraction potentials for secondary electrons would be significantly reduced compared to those required to collect secondary ions.

Despite the challenges to be overcome if SE spectroscopy is to be established as a microanalysis tool in HeIMs, it has the potential to augment the analytical tools within the HeIM and allow access to new valuable information and novel experiments.

Applications

Chemical Analysis

Microanalysis for Biological and Insulating Materials

SE spectroscopy in the SEM is an opportunity for microanalysis of soft materials where other tools fall short. For soft and insulating materials, such as uncoated polymers and biological materials the beam sensitivity complicates common analytical tools such as energy dispersive X-ray spectroscopy (EDX) or BSE imaging in the SEM. In the HeIM, EDX is unavailable due to the insufficient velocity of the incident He$^+$ ions [26], and if yields are sufficient the information content and lateral resolution of RBS imaging is limited. In this respect the HeIM has advantages over the SEM; firstly, as discussed above uncoated insulating specimens are more easily imaged at higher magnification and secondly the HeIM boasts higher SE yields than SEM enabling lower dose imaging of beam sensitive materials.

Within HeIMs and SEMs with energy filtering capabilities the SE emission spectrum can be measured for each pixel, although analysing a group of pixels in the area of interest is more favourable with regards to the signal to noise ratio. Thus, differences in the micro and nanostructure can be revealed

through the local SE emission spectrum. However, the resulting spectral dataset comes together from tens to hundreds of images and the dose the sample is subject to during a serial acquisition may be prohibitive to the analysis if the overall dose has damaged or otherwise manipulated the sample. By comparing the SE spectra of different material phases, the energy window giving rise to the highest material contrast between the phases can be determined, and subsequently imaged at high resolution but relatively low dose [77]. This approach of secondary electron hyperspectral imaging (SEHI) has the advantage of reducing overall beam exposure of the sample while maximising the desired contrast and resolution in the selected energy window. With the same goal of reducing overall beam exposure, Kazemian *et al.* have modulated the SE analyser setting in phase with the line scan duration to perform the desired measurement from a single image [66]. Other data collection strategies are conceivable to optimise energy differential SE collection while controlling dose in SEM and HeIM where suitable user control is given. SEHI has been applied to great success in SEMs on materials of various properties and applications; from inorganic perovskite photovoltaic materials [60], over organic photovoltaic blends [77] to fully insulating microporous polypropylene [78] and silk biopolymer [75] and so SEHI holds great potential for the HeIM as well.
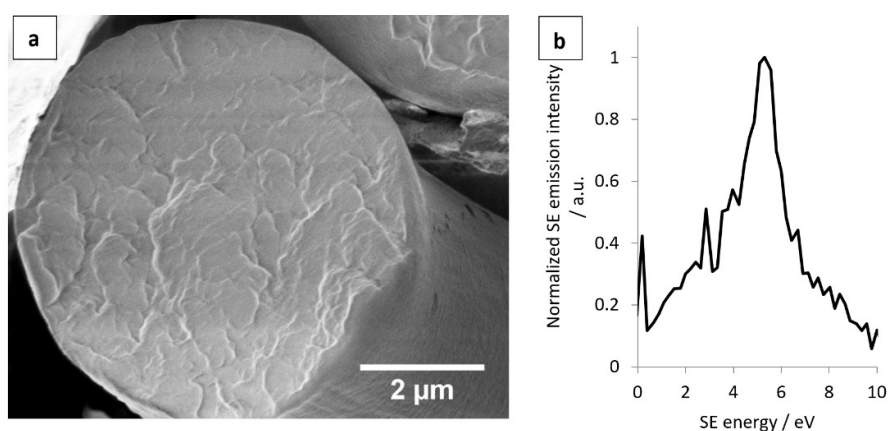

FIG. 6: SEM image of a cryo-snapped cross section of a Nephila edulis spider dragline silk and accompanying SE emission spectrum recorded in a FEI Helios SEM at 700 V.

A sample spectrum collected from a cross-section of cryo-snapped *Nephila edulis* spider dragline silk in an FEI Helios SEM at 700 V accelerating voltage is shown in **FIG. 6.** There is banding visible in the total yield SE image which is caused by sample charging of the uncoated surface, and which makes obtaining higher resolution hyperspectral images a challenge. Yet in order to understand the nanostructural features of such remarkable biopolymers, higher resolution hyperspectral images are required. This challenge has already been met with slightly larger silkworm silks where nanoscale differences in protein order and disorder within the fibre have been identified [75], but spider silk remains a challenge. In particular, more work needs to be done to assess the repeatability of spectra from such challenging materials and their response to differences within the material. To this date no HeIM SE spectra have been reported for biological and natural structural materials, although charging can be expected to be more manageable. Thus, higher resolution studies utilising hyperspectral imaging may be more easily realised in the HeIM than the SEM.

In determining how comparable SE spectra are between different SEM and HeIM instruments, a PffBT4T film was investigated as a polymer used in promising organic photovoltaic blends [79]. Despite all the differences in energy analyser design and the charged particle beam, some features of the

spectral fine structure align when the onsets are set at 0 eV, notably a peak at 3.4 eV. This peak is reproduceable in different instruments and thus there can be confidence that the dominant signal at low energy is due to SE1 emissions characteristic of the material, which has previously been confirmed in SEHI studies in the Nova NanoSEM [60].The high stopping power of He$^+$ ions in the interaction volume has been simulated to result in a high SE1 to SE2 ratio in low z materials [27], whereas the use of the in-lens detector in the SEMs excludes any significant contribution of SE3 within the energy range shown [69]. The similarities between SEM in-lens and HeIM Everhart-Thornley SE detection shown here have also been observed by Bell in total yield iSE imaging studies of inorganic nano-rods [80].

The calibration of the SE energy can be performed by the sample-biasing procedure reported elsewhere [72]. While the energy scale is straightforward, the location of the onset and thus determining the 0 eV SE energy point is a little more challenging. Onsets may be shifted from the expected 0 eV energy due to unwanted fields such as charging, or by material properties such as changes in the work function [81]. In the data presented in **FIG. 7** the onset was set as the first local minimum emission value at lower energy than the highest positive gradient – i.e. the base of the steep increase in emission associated with the spectral onset. However frequently there are artefacts below the onset energy whose origin and significance are not understood, and which can confuse the assignment of the onset.
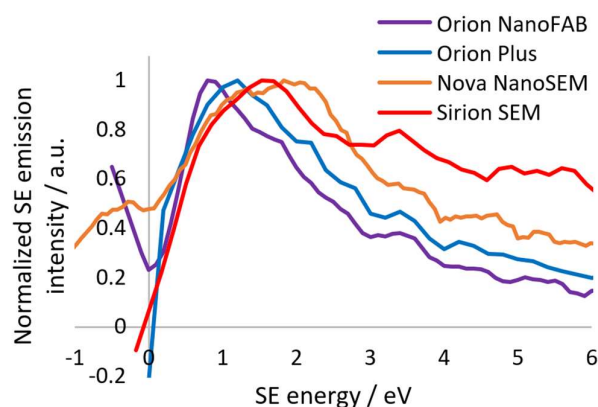

FIG. 7: PffBT4T SE spectra compared between HeIM and SEM instruments. The HeIM spectra were recorded at 30 keV and the SEM spectra at 1 kV.

In separate iSE electron energy distribution studies of metals Ohya *et al.* and Petrov *et al.* have noted the lower energy maximum and a more rapid emission drop off at energies above the maximum leading to a sharper peak in the HeIM compared to the SEM [55–58]. In principal, this observation is consistent with the data presented; however, no definite differences in the intensities between the iSE and eSE spectra can be described meaningfully if the collection efficiencies of the different SE analysers are not known.

Despite the challenges in understanding the differences in detector characteristics, **FIG. 7** demonstrates that principally the same sample can have spectral features which appear independently of the instrument. This is the basis for comparable studies and progress in better understanding the significance of SE spectral features with regards to in-situ microanalysis and its potential applications.

Suppression of Topography for Rough Samples

Some materials of scientific and commercial interest are inherently rough. The study of such samples is difficult with regards to SE analysis, as it is widely known that SEs contain topographical information. However, if a high collection efficiency over a wide angular range is given, for example by an in-lens detection using a high suction tube voltage, it may be expected that low energy SE1s arising from highly localised excitation events may contain little topographical information. **FIG. 8** demonstrates that suppression of topographical information in SEs is indeed possible: Plasma treated cellulosic fibres exhibit surface nanostructure, which is expected to protrude topographically, but also be of different composition compared to the matrix. In total yield SE imaging it is not clear whether the enhanced brightness of the nano-features is purely topographical, or whether chemical differences play a role (see **FIG. 8 a**). The different dominant contrast mechanisms within different energy windows are clearly shown in **FIG. 8 c** and **d**. When considering how the detected electrons respond to the topographical feature indicated by the arrow it is clear that the main contrast mechanism for the lower energy SEs in **c** is the difference in chemistry, whereas within the higher energy SEs shown in **d** the edge effect and hence topography is by far the dominant contrast mechanism. A similar SE energy cut-off for the separation of chemical and topographical SE information has been reported to map compositional contrast in caterpillar silk and perovskite photovoltaic material and in the same SEM instrument [60,75].
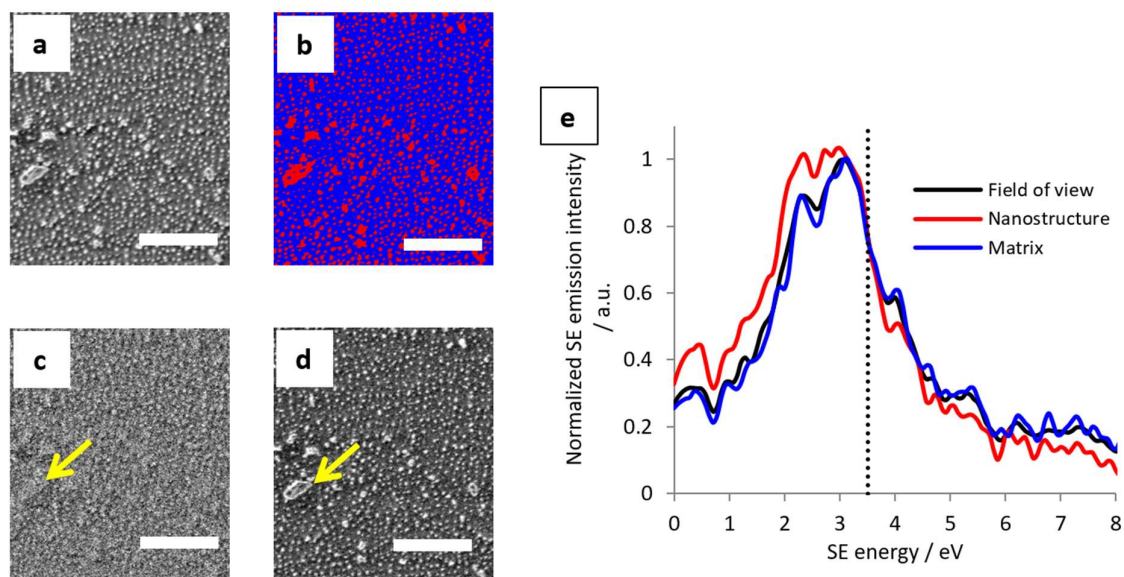

FIG. 8: Hyperspectral imaging and SE spectroscopy for ramie plant fibre using SEHI recorded in a Nova NanoSEM at 1 kV **a)** Field of view of the standard SE image, **b)** visualisation of the thresholding used to separate emissions from the matrix and nanostructure in blue and red respectively, **c)** SEHI image representing the SE emissions in the energy window of 0-3.5 eV showing the suppression of the edge effect to reveal chemical contrast, **d)** SEHI image representing the SE emissions in the energy window of 3.5-8 eV showing the edge effect and hence topography as the dominant contrast mechanism, **e)** SE spectrum of the surface shown in the images **a-d** showing increased low-energy SE emission of the nanostructure. Scale bars show 1 μm.

In this analysis thresholding was used to separate the spectrum of the matrix (blue) from the spectrum of the nanostructure (red) (**FIG. 8 b**). Notably, the nano structure emits more SEs than the amorphous matrix in the lower energy region below 3.5 eV, indicated by the dotted line. Thus, the chemical

contrast revealed in **FIG. 8 c** arises from differences in the SE emission between the nanostructure and matrix in this energy region.

The HeIM has already been shown to deliver superior lateral resolution and image stability for insulating and biological materials. The realisation of topography suppression within the iSE signal in the HeIM has the potential of unlocking new structural analysis tools for soft and rough samples – which include some of nature's most exciting materials.

Process Control for Chemically Complex Samples

While many microanalysis tools such as RBS and SIMS are concerned with determining atomic and molecular composition, there are other material properties such as molecular orientation, order and local variation which govern the success or failure of many modern materials, especially those widely used in electronics or tissue engineering.

P3HT is a conductive polymer with immense significance to the field of organic electronics and the organic photovoltaic (OPV) industry. It is commonly used with fullerenes in a blend to make organic solar cells. The processing parameters of the pure films and the OPV blends have a significant effect on important material parameters, especially molecular and long-range order, which in turn directly affect charge transport [82]. Thus, these processing parameters must be optimised and controlled.
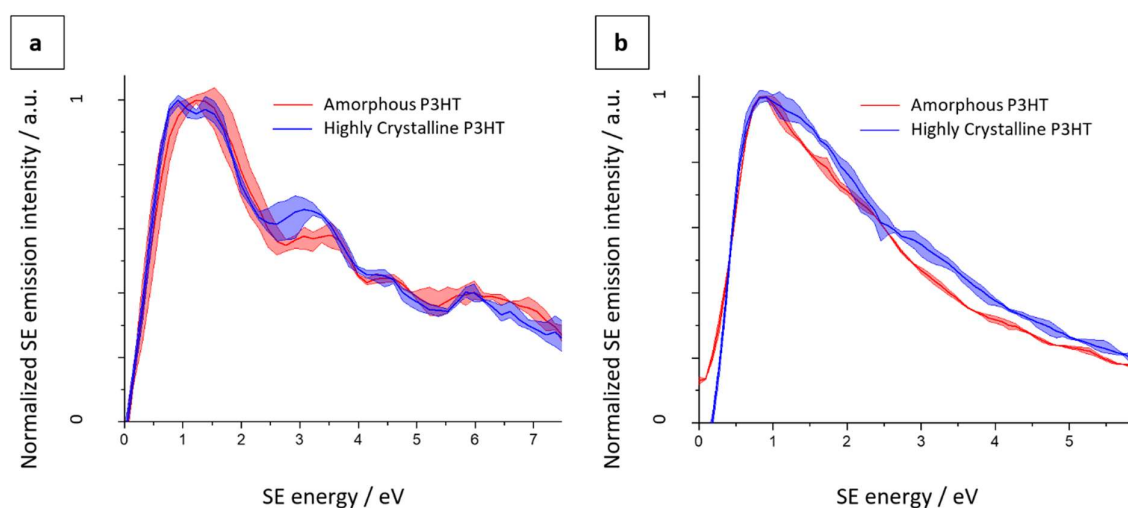

FIG. 9: SE spectra of high order annealed regioregular and low order regiorandom P3HT recorded at 1 keV in the SEM **(a)** and 30 keV in the HeIM **(b)**. The solid line represents the average signal from three different areas, whereas the transparent coloured background of the represents the minimum and maximum range within the three acquisitions.

After it was shown that hyperspectral imaging within SE energy windows can dramatically enhance morphological contrast in OPV blends [77], the underlying SE emission mechanisms were further investigated in the pure polymer system [73]. **FIG. 9 a** shows the comparison between amorphous and highly crystalline P3HT spectra in the FEI Sirion SEM. The difference in crystallinity arises from the polymerisation conditions and the processing of the P3HT: The highly crystalline sample is made by annealing a regioregular P3HT polymer, whereas the amorphous P3HT is an unannealed regiorandom polymer film. The difference in SE electron distribution due to the order inherent to the polymer is evident, for example in the most intense peak at low energy the SE distribution of the highly crystalline

sample exhibits a double peak which manifests as a single broad peak in the amorphous sample. The processing and polymerisation conditions are clearly encoded in the SE emission behaviour through the presence or absence of order, and thus there is potential for it to be mapped [73]. Furthermore, the samples exhibit different variation of certain spectral features: While the lowest energy peak of the highly crystalline sample has a highly conserved peak width, the same peak in the amorphous sample diverges significantly from the average in repeat spectra. It can be proposed that in a favourable sample the variability of spectra reflects inherent property fluctuations, such as order and disorder, and that this could be exploited to explore multi-scale variability of material properties using SE spectroscopy within charged particle microscopes. The same experiment performed in the HeIM is shown in **FIG. 9 b**, with markedly less distinct features present in the spectra, potentially because collection parameters are not optimal. However, as in the SEM data the peak of the highly crystalline P3HT appears as a double peak, and a weak shoulder is present at 3 eV where the SEM spectrum exhibits a more prominent peak. While analysis based on spectral features may be difficult to realise with the spectra presented in **FIG. 9 b**, the two spectra are very distinct in their surface potentials: Consistently within the dataset the amorphous sample was shifted by 0.64 eV to set the spectral onset at 0 eV, whereas the highly crystalline sample was shifted by 0.91 eV. Such shifts in the spectral onset are exciting for mapping regions of high and low crystallinity in a semi-crystalline sample, as phase contrast can be enhanced dramatically if an energy window is chosen systematically [77]. Such differences in the surface potential were not observed in the SEM, presumably due to the difference in polarity of the impinging charged particle.

It is noteworthy that the distinction between the two materials in both instruments is best made at low SE energies below 4 eV, which is a SE energy range which is usually poorly resolved in early SE spectroscopy work. Further work understanding low energy SE emissions promises novel ways of analysing material surfaces and mapping critical properties.

Nano-Engineering Applications

Nano-Engineering Control

In understanding and quantifying the effects of ion beam exposure on various samples, in-situ analysis tools besides the contrast in total yield SE imaging are sought. Fox *et al.* have reported the controlled manipulation of few-layer MoS_2 electrical properties using the HeIM, and have related the dose to semiconductor or metal-like resistivity behaviour [14]. In the study the resistivity had to be measured ex-situ, but as the secondary electron emission signatures are expected to change with the electronic structure there is scope for SE spectroscopy to be developed as a technique to understand the ion beam induced modification of electronic properties live and in-situ. This has been proposed as early as 2004 by Joy *et al.* [63] and work by Zhou *et al.* showcases the feasibility of this approach on graphene [71].

To save time and raise efficiency of small-scale but big impact nano-engineering applications, automation is paramount. While Joe *et al.* demonstrated that automated image processing of the total yield iSE signal can be used to direct a FIB to stop at material interfaces [83], the beam could be set to respond to various sample properties, such as phase composition, if such sample properties are defined in specific SE energy windows. For example, this could ensure selective machining of nanostructured samples in which the different phases respond differently to the beam.

While some nanofabrication methods actively seek the chemical modification of the sample by the beam, it must be minimised for other applications such as the preparation of electron-thin TEM samples. In this work highly oriented pyrolytic graphite (HOPG) was studied under electron and ion beam irradiation as a suitable model graphite sample. The low angular spread of its graphite sheets leads to a well-defined orientation of the crystal structure relative to the beam and thus its SE emission from various excitation sources have been studied decades ago: The SE emission spectra of HOPG from low voltage He⁺ beams and ultraviolet excitation have been compared by Ferrón *et al.*, whereby there is a clear change in peak shape with progressing damage of the 5 keV He⁺ beam to the HOPG surface [84]. Thus, the influence of beam exposure on the sample surface is reflected in the SE spectrum and can be followed in situ by a series of spectral acquisitions. In this work the evolution of the spectra with increasing total beam exposure differs between the HeIM and the SEM: In the SEM the SE spectrum of HOPG changes within a single acquisition, and AFM data shows that this is due to a rapid formation of electron beam induced deposition (EBID) (**FIG. 10 d**). After three spectra the measurement is dominated by the EBID, and it is clear that this poses a limitation to a technique as surface sensitive as SE spectroscopy in a low voltage SEM (LV-SEM).
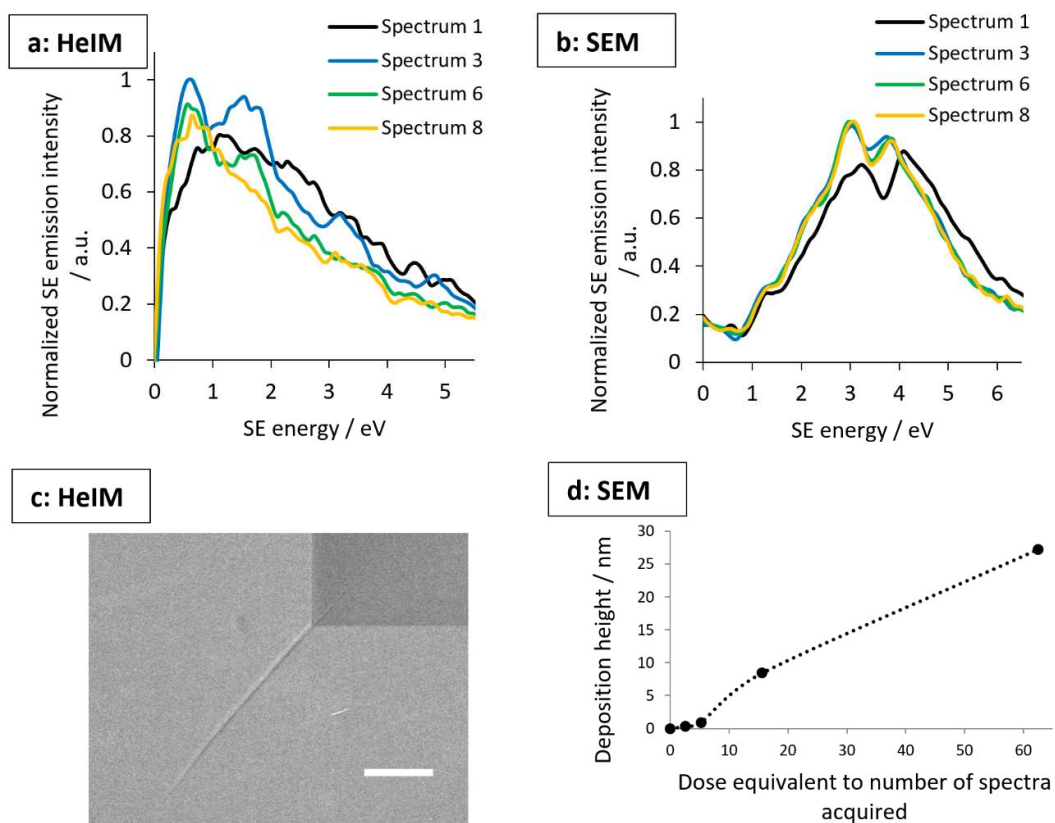
FIG. 10: Evolution of spectra and sample surface with ion or electron dose **a)** 30 keV HeIM SE spectra of HOPG imaged consecutively in the same field of view recorded in the Orion NanoFAB **b)** 1 kV SEM SE spectra of HOPG imaged consecutively in the same field of view recorded in the FEI Nova NanoSEM **c)** cracking at the corner of the spectral field of view (dark square) due to helium implantation after 8 spectral acquisitions in the HeIM, scalebar 2 μm **d)** Accumulation of electron-beam induced deposition (EBID) in the SEM as measured by AFM

Like LV-SEM, HeIM is very surface sensitive to the point where the SE spectra in this work were affected by the previous use and the cleanliness of the chamber, which must be kept in mind for nanofabrication applications. In the example of HOPG, a chamber in which PffBT4T had been milled prior to SE spectral collection lead to a spectrum dominated by a potential PffBT4T contamination layer as represented in spectrum 1 in **FIG. 10 a**. With increasing ion dose, spectral fine structure emerges, which is most prominent in spectrum 3. While the origin of this fine structure requires further validation in this work, it may represent the bulk HOPG spectrum if the He^+ beam has sputtered the contamination layer. In either case, in both the SEM and the HeIM surface sensitivity can be a complicating factor, however the HeIM has a clear advantage due to the availability of micromachining He^+ and Ne^+ beams to polish the surface and access bulk information.

With further He^+ beam exposure the fine structure in spectrum 3 fades again due to continuous He^+ damage of the HOPG surface, but the overall spectrum shape differs to that of the contamination dominated spectrum 1. The total yield SE images become progressively darker with each acquisition, but do not capture this multi-stage evolution under beam exposure and could lead to uncertainty as to whether the sample is covered in a contamination layer or has been significantly damaged by He^+ ion exposure. Conventionally the acceptable doses would have to be validated ex-situ, for example by Raman spectroscopy [85]. Here, SE spectroscopy could be an effective way to monitor both the polishing of the contamination layer and the increasing beam damage in situ, making it possible to seize any window of opportunity between the two processes to obtain bulk information. Monitoring the surface condition in situ by the use of SE spectroscopy or SEHI can allow in-situ optimisation of procedures such as He^+ polishing for electron-thin TEM samples when mitigation of beam damage is crucial.

The continuous measurement of the same area does not only damage the surface through beam exposure, but also leads to He implantation. **FIG. 10 c** clearly shows the evolution of cracks radiating from the stress-concentrated corners of the spectral field of view due to implantation of He gas, which becomes visible after six spectral acquisitions. This is consistent with accounts of bubble formation of silicon and graphene in literature [10]. In the case of HOPG the layered structure seems to allow bubbles to connect across the exposed area to delaminate the HOPG layers below the surface and result in such cracking at the corner of the spectral field of view.

Besides tracking the effect of ion beam irradiation on carbon samples, the ability to distinguish between different carbon species on a surface can be useful in tracking contamination. For example, it may be valuable to track amorphous carbon char caused by unfavourable reactions of a precursor gas under ion beam irradiation, or it may serve to monitor resistance channels caused by contamination when making carbon nanotube devices [86]. The sensitivity of SE spectra to the electronic structure governed by the nature of the carbon-carbon bonding was shown in a study in 1994 using a 1 keV electron gun and an Auger electron energy analyser [87]. In this work, the spectra of features on the surface of the HOPG sample which appeared to be graphene-like (**FIG. 11 c**) were compared to the spectra of the bulk surface (**FIG. 11 a** and **b**). While the differences between bulk and flakes are present in both instruments, the difference in the HeIM spectra is a lot less pronounced, perhaps because the graphene–like surface flakes are less free-standing compared to the flake analysed in the SEM, allowing bulk signal to pass through.
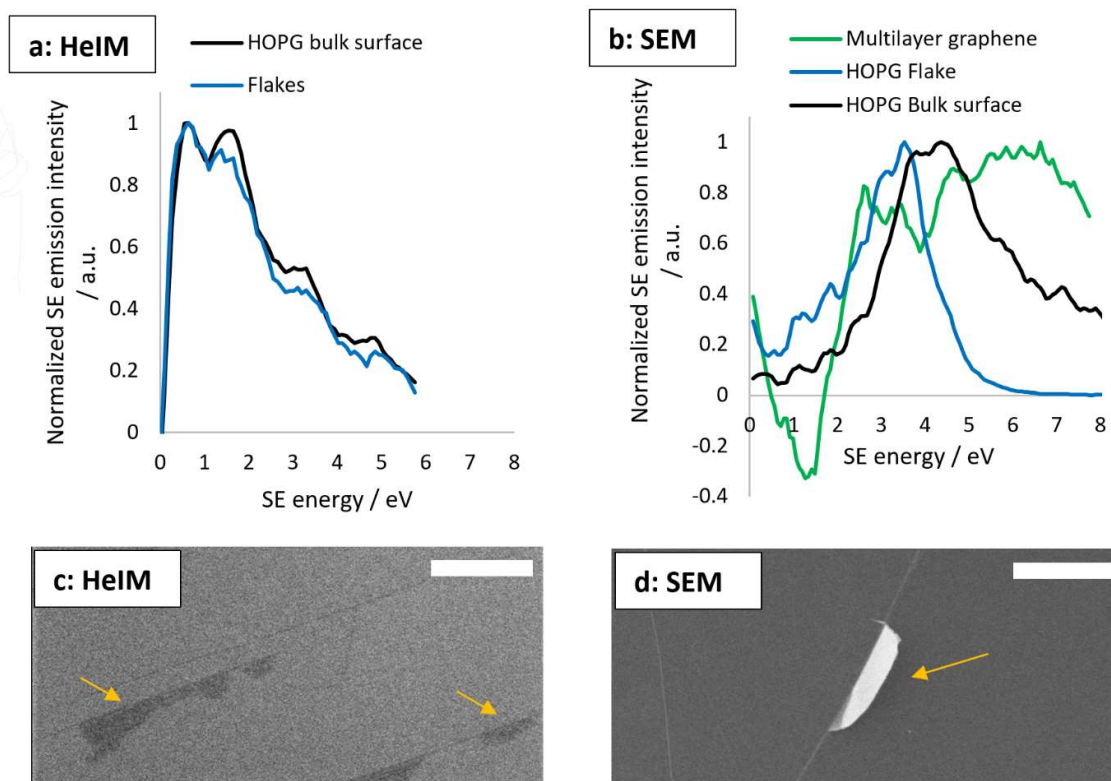
FIG. 11: Spectral comparison of graphene and graphite like surface structures. **a)** 30 keV Orion NanoFAB HeIM spectra **b)** 1 kV Nova NanoSEM spectra, including multilayer graphene (n > 10) **c)** images illustrating graphene-like flakes in the HeIM and **d)** SEM, scalebars represent 2 μm.

In the Nova NanoSEM data from multilayer graphene is available to demonstrate that with increasing bulk graphite characteristic of the carbon species the dominant peak appears at higher energy. Zhou *et al.* have used this effect to quantify the number of graphene layers using SE spectra in SEMs and HeIMs [71] and other reference studies to distinguish between different carbon states could be performed.

Understanding and Managing Damage

The reduced sputter- and damage rate of He$^+$ ions compared to Ga$^+$ ions is an opportunity for in-situ modification and imaging of beam sensitive materials such as polymers. As mentioned previously, organic photovoltaic blend morphology is important for device performance, and the top-down blend morphology of a PffBT4T-2OD:PC$_{70}$BM organic photovoltaic blend is shown in **FIG. 12 a**. However, a top-down image of the phase structure is superficial and may not be representative of the 3D phase structure of such blends. Thus, in an attempt to reveal the transverse phase-structure the blend was cryo-snapped, and the cross-section is shown in **FIG. 12 b**. Unfortunately the phase-structure in the cross-section is not as clear as in the top-down view due to cleaving artefacts obscuring the picture. **FIG. 12 c** illustrates how a He$^+$ beam at glancing incidence to the cross-section has been used to polish these cleaving artefacts after cryo-fracture. The He$^+$ beam irradiation does result in damage which manifests in a featureless surface, and so in this work the blend morphology has been recovered by 20 s of O$_2$/Ar plasma treatment analogously to approaches described in literature [88]. Note that the cross-sectional features are protected by a capping layer of PEDOT:PSS polymer to avoid damage

towards the top of the cross section where the polishing He$^+$ beam impinges the sample. The images showcase the versatility of the HeIM as a nanofabrication and imaging tool, if damage effects are understood and managed. Future work will lie in the further optimisation of such sample preparation protocols by incorporating SE spectroscopy and energy selective imaging as a tool to quantify damage and increase phase contrast.
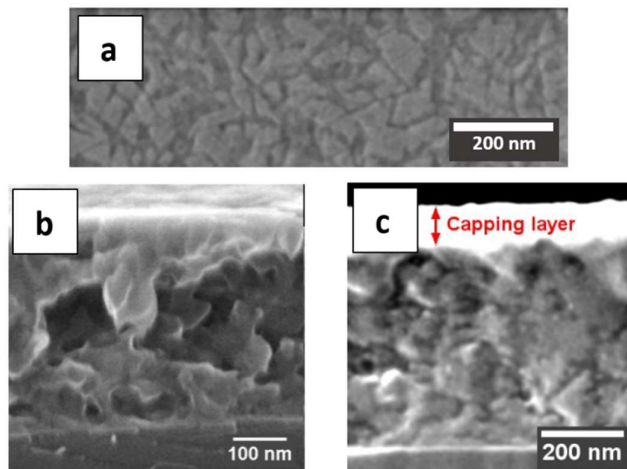

FIG. 12: PffBT4T-2OD:PC$_{70}$BM organic photovoltatic blend **a)** top-down view showing phase-structure **b)** cross-section in the HeIM after cryo-snapping with topographical cleaving artefacts obscuring phase-structure **c)** The same blend protected with a PEDOT:PSS capping layer and then subject to He$^+$ polishing of the cross-section at glancing incidence. The damage layer caused by the He$^+$ polishing was removed by a O$_2$/Ar plasma to reveal the blend morphology

Conclusions & Future Outlook

The integration of secondary electron spectroscopy has the potential to be a key enabling technology in the HeIM for the development and optimisation of nano-engineering processes. Understanding SE contrast beyond the total yield and analysing SE emission characteristics can reveal chemical and structural information on the nanoscale, and promises an in-situ understanding of cleanliness, beam induced damage, modification and deposition. To become a reliable technique which can be embedded into nano-engineering workflows, new SE energy detectors must emerge with defined characteristics and parallel SE measurement. Besides increasing the understanding of beam-sample interactions and enhancing process control, a refined low energy SE spectrometer within charged particle microscopes can open doors to nanoscale studies of sensitive and complex samples, such as natural nanocomposites, and will allow novel experiments at unprecedented resolution.

Acknowledgements

References

1. N. Sasaki: *An Ion Microscope with a Transverse Magnetic Field*. J. Appl. Phys. **19**, 1050–1053 (1948), doi:10.1063/1.1698008.

2. M. Komuro, N. Atoda and H. Kawakatsu: *Ion beam exposure of resist materials*. J. Electrochem. Soc. **126**, 483–490 (1979).

3. V.E. Krohn and G.R. Ringo: *Ion source of high brightness using liquid metal*. Appl. Phys. Lett. **27**, 479–481 (1975).

4. R. Levi-Setti: *Proton scanning microscopy: feasibility and promise*, in: O. Johari (Ed.): *Scanning Electron Microscopy*, 1st ed. (IITRI, Chicago, USA, 1974), pp. 125–135.

5. R.L. Seliger, J.W. Ward, V. Wang and R.L. Kubena: *A high-intensity scanning ion probe with submicrometer spot size*. Appl. Phys. Lett. **34**, 310–312 (1979).

6. L.W. Swanson: *Liquid metal ion sources: Mechanism and applications*. Nucl. Instruments Methods Phys. Res. **218**, 347–353 (1983).

7. B.W. Ward, J.A. Notte and N.P. Economou: *Helium ion microscope: A new tool for nanoscale microscopy and metrology*. J. Vac. Sci. Technol. B Microelectron. Nanom. Struct. Process. Meas. Phenom. **24**, 2871–2874 (2006).

8. R.H. Livengood, S. Tan, R. Hallstein, J. Notte, S. McVey and F.H.M. Faridur Rahman: *The neon gas field ion source—a first characterization of neon nanomachining properties*. Nucl. Instruments Methods Phys. Res. Sect. A Accel. Spectrometers, Detect. Assoc. Equip. **645**, 136–140 (2011), doi:https://doi.org/10.1016/j.nima.2010.12.220.

9. F.H.M. Rahman, S. McVey, L. Farkas, J.A. Notte, S. Tan and R.H. Livengood: *The Prospects of a Subnanometer Focused Neon Ion Beam*. Scanning **34**, 129–134 (2012), doi:10.1002/sca.20268.

10. D. Fox, Y. Chen, C.C. Faulkner and H. Zhang: *Nano-structuring, surface and bulk modification with a focused helium ion beam*. Beilstein J. Nanotechnol. **3**, 579 (2012).

11. Y. Zhou, P. Maguire, J. Jadwiszczak, M. Muruganathan, H. Mizuta and H. Zhang: *Precise milling of nano-gap chains in graphene with a focused helium ion beam*. Nanotechnology **27**, 325302 (2016).

12. M.C. Lemme, D.C. Bell, J.R. Williams, L.A. Stern, B.W.H. Baugher, P. Jarillo-Herrero and C.M. Marcus: *Etching of graphene devices with a helium ion beam*. ACS Nano **3**, 2674–2676 (2009).

13. D.C. Bell, M.C. Lemme, L.A. Stern, J.R. Williams and C.M. Marcus: *Precision cutting and*

patterning of graphene with helium ions. Nanotechnology **20**, 455301 (2009).

14. D.S. Fox, Y. Zhou, P. Maguire, A. O'Neill, C. Ó'Coileáin, R. Gatensby, A.M. Glushenkov, T. Tao, G.S. Duesberg and I. V Shvets: *Nanopatterning and electrical tuning of MoS2 layers with a subnanometer helium ion beam*. Nano Lett. **15**, 5307–5313 (2015).

15. P. Philipp, L. Rzeznik and T. Wirtz: *Numerical investigation of depth profiling capabilities of helium and neon ions in ion microscopy*. Beilstein J. Nanotechnol. **7**, 1749 (2016).

16. M.S. Joens, C. Huynh, J.M. Kasuboski, D. Ferranti, Y.J. Sigal, F. Zeitvogel, M. Obst, C.J. Burkhardt, K.P. Curran and S.H. Chalasani: *Helium Ion Microscopy (HIM) for the imaging of biological samples at sub-nanometer resolution*. Sci. Rep. **3**, 3514 (2013).

17. S. Tan, R. Livengood, P. Hack, R. Hallstein, D. Shima, J. Notte and S. McVey: *Nanomachining with a focused neon beam: A preliminary investigation for semiconductor circuit editing and failure analysis*. J. Vac. Sci. Technol. B, Nanotechnol. Microelectron. Mater. Process. Meas. Phenom. **29**, 06F604 (2011).

18. L. Rzeznik, Y. Fleming, T. Wirtz and P. Philipp: *Experimental and simulation-based investigation of He, Ne and Ar irradiation of polymers for ion microscopy*. Beilstein J. Nanotechnol. **7**, 1113 (2016).

19. P. Maguire, D.S. Fox, Y. Zhou, Q. Wang, M. O'Brien, J. Jadwiszczak, J. McManus, N. McEvoy, G.S. Duesberg and H. Zhang: *Defect Sizing, Distance and Substrate Effects in Ion-Irradiated Monolayer 2D Materials*. arXiv (2017), http://arxiv.org/abs/1707.08893.

20. J. Melngailis: *Focused ion beam lithography*. Nucl. Instruments Methods Phys. Res. Sect. B Beam Interact. with Mater. Atoms **80**, 1271–1280 (1993).

21. X. Shi, P. Prewett, E. Huq, D.M. Bagnall, A.P.G. Robinson and S.A. Boden: *Helium ion beam lithography on fullerene molecular resists for sub-10nm patterning*. Microelectron. Eng. **155**, 74–78 (2016).

22. H. Wu, L.A. Stern, D. Xia, D. Ferranti, B. Thompson, K.L. Klein, C.M. Gonzalez and P.D. Rack: *Focused helium ion beam deposited low resistivity cobalt metal lines with 10 nm resolution: implications for advanced circuit editing*. J. Mater. Sci. Mater. Electron. **25**, 587–595 (2014).

23. M.G. Stanford, B.B. Lewis, K. Mahady, J.D. Fowlkes and P.D. Rack: *Advanced nanoscale patterning and material synthesis with gas field helium and neon ion beams*. J. Vac. Sci. Technol. B, Nanotechnol. Microelectron. Mater. Process. Meas. Phenom. **35**, 30802 (2017).

24. A. Belianinov, M.J. Burch, S. Kim, S. Tan, G. Hlawacek and O.S. Ovchinnikova: *Noble gas ion beams in materials science for future applications and devices*. MRS Bull. **42**, 660–666 (2017), doi:10.1557/mrs.2017.185.

25. M. Huth, F. Porrati, C. Schwalb, M. Winhold, R. Sachser, M. Dukic, J. Adams and G. Fantner: *Focused electron beam induced deposition: A perspective*. Beilstein J. Nanotechnol. **3**, 597 (2012).

26. D.C. Joy and B.J. Griffin: *Is microanalysis possible in the helium ion microscope?*. Microsc. Microanal. **17**, 643–649 (2011).

27. R. Ramachandra, B. Griffin and D. Joy: *A model of secondary electron imaging in the helium ion scanning microscope*. Ultramicroscopy **109**, 748–757 (2009).

28. L. Scipioni, C.A. Sanford, J. Notte, B. Thompson and S. McVey: *Understanding imaging modes in the helium ion microscope*. J. Vac. Sci. Technol. B Microelectron. Nanom. Struct. Process. Meas. Phenom. **27**, 3250–3255 (2009), doi:10.1116/1.3258634.

29. S. Sijbrandij, B. Thompson, J. Notte, B.W. Ward and N.P. Economou: *Elemental analysis with the helium ion microscope*. J. Vac. Sci. Technol. B Microelectron. Nanom. Struct. Process. Meas. Phenom. **26**, 2103–2106 (2008).

30. N. Klingner, R. Heller, G. Hlawacek, J. von Borany, J. Notte, J. Huang and S. Facsko: *Nanometer scale elemental analysis in the helium ion microscope using time of flight spectrometry*. Ultramicroscopy **162**, 91–97 (2016), doi:10.1016/j.ultramic.2015.12.005.

31. V. Veligura, G. Hlawacek, R. van Gastel, H.J.W. Zandvliet and B. Poelsema: *Channeling in helium ion microscopy: Mapping of crystal orientation*. Beilstein J. Nanotechnol. **3**, 501 (2012).

32. T. Wirtz, P. Philipp, J.N. Audinot, D. Dowsett and S. Eswara: *High-resolution high-sensitivity elemental imaging by secondary ion mass spectrometry: from traditional 2D and 3D imaging to correlative microscopy*. Nanotechnology **26**, 434001 (2015).

33. T. Wirtz, N. Vanhove, L. Pillatsch, D. Dowsett, S. Sijbrandij and J. Notte: *Towards secondary ion mass spectrometry on the helium ion microscope: An experimental and simulation based feasibility study with He+ and Ne+ bombardment*. Appl. Phys. Lett. **101**, 41601 (2012).

34. D. Dowsett and T. Wirtz: *Co-Registered In Situ Secondary Electron and Mass Spectral Imaging on the Helium Ion Microscope Demonstrated Using Lithium Titanate and Magnesium Oxide Nanoparticles*. Anal. Chem. **89**, 8957–8965 (2017).

35. F. Vollnhals, J.-N. Audinot, T. Wirtz, M. Mercier-Bonin, I. Fourquaux, B. Schroeppel, U. Kraushaar, V. Lev-Ram, M.H. Ellisman and S. Eswara: *Correlative Microscopy Combining Secondary Ion Mass Spectrometry and Electron Microscopy: Comparison of Intensity–Hue–Saturation and Laplacian Pyramid Methods for Image Fusion*. Anal. Chem. **89**, 10702–10710 (2017).

36. P. Gratia, G. Grancini, J.-N. Audinot, X. Jeanbourquin, E. Mosconi, I. Zimmermann, D. Dowsett, Y. Lee, M. Grätzel and F. De Angelis: *Intrinsic halide segregation at nanometer scale determines the high efficiency of mixed cation/mixed halide perovskite solar cells*. J. Am. Chem. Soc. **138**, 15821–15824 (2016).

37. P. Gratia, I. Zimmermann, P. Schouwink, J.-H. Yum, J.-N. Audinot, K. Sivula, T. Wirtz and M.K. Nazeeruddin: *The Many Faces of Mixed Ion Perovskites: Unraveling and Understanding the Crystallization Process*. ACS Energy Lett. **2**, 2686–2693 (2017), doi:10.1021/acsenergylett.7b00981.

38. T.E. Everhart and R.F.M. Thornley: *Wide-band detector for micro-microampere low-energy electron currents*. J. Sci. Instrum. **37**, 246 (1960).

39. S.Y. Lai, A. Brown, J.C. Vickerman and D. Briggs: *The relationship between electron and ion induced secondary electron imaging: A review with new experimental observations*. Surf. Interface Anal. **8**, 93–111 (1986).

40. R.A. Baragiola, E. V Alonso, J. Ferron and A. Oliva-Florio: *Ion-induced electron emission from clean metals*. Surf. Sci. **90**, 240–255 (1979).

41. J. Ferron, E. V Alonso, R.A. Baragiola and A. Oliva-Florio: *Electron emission from molybdenum*

under ion bombardment. J. Phys. D. Appl. Phys. **14**, 1707 (1981).

42. R. Hill and F.H.M.F. Rahman: *Advances in helium ion microscopy*. Nucl. Instruments Methods Phys. Res. Sect. A Accel. Spectrometers, Detect. Assoc. Equip. **645**, 96–101 (2011).

43. J. Notte, B. Ward, N. Economou, R. Hill, R. Percival, L. Farkas and S. McVey: *An introduction to the helium ion microscope*. AIP Conf. Proc. **931**, 489–496 (2007).

44. C. Rodenburg, P. Viswanathan, M.A.E. Jepson, X. Liu and G. Battaglia: *Helium ion microscopy based wall thickness and surface roughness analysis of polymer foams obtained from high internal phase emulsion*. Ultramicroscopy **139**, 13–19 (2014).

45. K. Tsuji, H. Suleiman, J.H. Miner, J.M. Daley, D.E. Capen, T.G. Păunescu and H.A.J. Lu: *Ultrastructural characterization of the glomerulopathy in Alport mice by helium ion scanning microscopy (HIM)*. Sci. Rep. **7**, 11696 (2017).

46. K. Tsuji, T.G. Păunescu, H. Suleiman, D. Xie, F.A. Mamuya, J.H. Miner and H.A.J. Lu: *Re-characterization of the glomerulopathy in CD2AP deficient mice by high-resolution helium ion scanning microscopy*. Sci. Rep. **7**, 8321 (2017).

47. W.L. Rice, A.N. Van Hoek, T.G. Păunescu, C. Huynh, B. Goetze, B. Singh, L. Scipioni, L.A. Stern and D. Brown: *High resolution helium ion scanning microscopy of the rat kidney*. PLoS One **8**, e57051 (2013), doi:10.1371/journal.pone.0057051.

48. D. Bazou, G. Behan, C. Reid, J.J. Boland and H.Z. Zhang: *Imaging of human colon cancer cells using He-Ion scanning microscopy*. J. Microsc. **242**, 290–294 (2011).

49. C. Rodenburg, X. Liu, M.A.E. Jepson, Z. Zhou, W.M. Rainforth and J.M. Rodenburg: *The role of helium ion microscopy in the characterisation of complex three-dimensional nanostructures*. Ultramicroscopy **110**, 1178–1184 (2010).

50. D.C. Joy and C.S. Joy: *Low voltage scanning electron microscopy*. Micron **27**, 247–263 (1996).

51. D.C. Joy: *Control of charging in low-voltage SEM*. Scanning **11**, 1–4 (1989).

52. M.A.E. Jepson, B.J. Inkson, C. Rodenburg and D.C. Bell: *Dopant contrast in the helium ion microscope*. Europhys. Lett. **85**, 46001 (2009).

53. C. Rodenburg, M.A.E. Jepson, B.J. Inkson and X. Liu: *Dopant contrast in the helium ion microscope: contrast mechanism*. J. Phys. Conf. Ser. **241**, 12076 (2010).

54. V. Iberi, I. Vlassiouk, X.G. Zhang, B. Matola, A. Linn, D.C. Joy and A.J. Rondinone: *Maskless Lithography and in situ Visualization of Conductivity of Graphene using Helium Ion Microscopy*. Sci. Rep. **5**, 11952 (2015), doi:10.1038/srep11952.

55. Y. V Petrov, O.F. Vyvenko and A.S. Bondarenko: *Scanning helium ion microscope: Distribution of secondary electrons and ion channeling*. J. Surf. Investig. X-Ray, Synchrotron Neutron Tech. **4**, 792–795 (2010).

56. V.Y. Mikhailovskii, Y. V Petrov and O.F. Vyvenko: *Energy filtration of secondary and backscattered electrons by the method of the retarding potential in scanning electron and ion microscopy*. J. Surf. Investig. X-Ray, Synchrotron Neutron Tech. **9**, 196–202 (2015), doi:10.1134/S1027451014060378.

57. Y. V Petrov and O.F. Vyvenko: *Secondary Electron Generation in the Helium Ion Microscope:*

Basics and Imaging, in: G. Hlawacek, A. Gölzhäuser (Eds.): *Helium Ion Microscopy*, 1st ed. (Springer International Publishing, Cham, Switzerland, 2016), pp. 119–146, doi:10.1007/978-3-319-41990-9_5.

58. K. Ohya, T. Yamanaka, K. Inai and T. Ishitani: *Comparison of secondary electron emission in helium ion microscope with gallium ion and electron microscopes*. Nucl. Instruments Methods Phys. Res. Sect. B Beam Interact. with Mater. Atoms **267**, 584–589 (2009).

59. M.K. T. Suzuki Y. Sakai, T. Ichinokawa: *Material Contrast of Scanning Electron and Ion Microscope Images of Metals*. Micros. Today **16**, 6–10 (2008).

60. V. Kumar, W.L. Schmidt, G. Schileo, R.C. Masters, M. Wong-Stringer, D.C. Sinclair, I.M. Reaney, D. Lidzey and C. Rodenburg: *Nanoscale Mapping of Bromide Segregation on the Cross Sections of Complex Hybrid Perovskite Photovoltaic Films Using Secondary Electron Hyperspectral Imaging in a Scanning Electron Microscope*. ACS Omega **2**, 2126–2133 (2017).

61. D.H. Bruining: *5 - Variation of Secondary Emission Yield Caused by The External Adsorption of Ions and Atoms*, in: *Physics and Applications of Secondary Electron Emission*, 2nd ed. (Pergamon Press, London, England, 1962), pp. 69–77, doi:10.1016/B978-0-08-009014-6.50008-9.

62. R.F. Willis, B. Fitton and D.K. Skinner: *Study of carbon-fiber surfaces using Auger and secondary electron emission spectroscopy*. J. Appl. Phys. **43**, 4412–4419 (1972).

63. D.C. Joy, M.S. Prasad and H.M. Meyer: *Experimental secondary electron spectra under SEM conditions*. J. Microsc. **215**, 77–85 (2004).

64. M.S. Chung and T.E. Everhart: *Simple calculation of energy distribution of low-energy secondary electrons emitted from metals under electron bombardment*. J. Appl. Phys. **45**, 707–709 (1974).

65. C. Schönjahn, C.J. Humphreys and M. Glick: *Energy-filtered imaging in a field-emission scanning electron microscope for dopant mapping in semiconductors*. J. Appl. Phys. **92**, 7667–7671 (2002), doi:10.1063/1.1525862.

66. P. Kazemian, S.A.M. Mentink, C. Rodenburg and C.J. Humphreys: *High resolution quantitative two-dimensional dopant mapping using energy-filtered secondary electron imaging*. J. Appl. Phys. **100**, 54901 (2006).

67. M.A.E. Jepson, B.J. Inkson, X. Liu, L. Scipioni and C. Rodenburg: *Quantitative dopant contrast in the helium ion microscope*. Europhys. Lett. **86**, 26005 (2009).

68. R. O'Connell, Y. Chen, H. Zhang, Y. Zhou, D. Fox, P. Maguire, J.J. Wang and C. Rodenburg: *Comparative study of image contrast in scanning electron microscope and helium ion microscope*. J. Microsc. **268**, 313–320 (2017).

69. B.J. Griffin: *A comparison of conventional Everhart-Thornley style and in-lens secondary electron detectors—a further variable in scanning electron microscopy*. Scanning **33**, 162–173 (2011).

70. C. Rodenburg, M.A.E. Jepson, E.G.T. Bosch and M. Dapor: *Energy selective scanning electron microscopy to reduce the effect of contamination layers on scanning electron microscope dopant mapping*. Ultramicroscopy **110**, 1185–1191 (2010).

71. Y. Zhou, D.S. Fox, P. Maguire, R. O'Connell, R. Masters, C. Rodenburg, H. Wu, M. Dapor, Y.

Chen and H. Zhang: *Quantitative secondary electron imaging for work function extraction at atomic level and layer identification of graphene*. Sci. Rep. **6**, 21045 (2016).

72. P. Kazemian, S.A.M. Mentink, C. Rodenburg and C.J. Humphreys: *Quantitative secondary electron energy filtering in a scanning electron microscope and its applications*. Ultramicroscopy **107**, 140–150 (2007).

73. M. Dapor, R.C. Masters, I. Ross, D.G. Lidzey, A. Pearson, I. Abril, R. Garcia-Molina, J. Sharp, M. Unčovský, T. Vystavel, F. Mika and C. Rodenburg: *"Secondary electron spectra of semi-crystalline polymers – A novel polymer characterisation tool?"* J. Electron Spectros. Relat. Phenomena **222**, 95–105 (2018), doi:10.1016/j.elspec.2017.08.001.

74. R.H. Livengood, Y. Greenzweig, T. Liang and M. Grumski: *Helium ion microscope invasiveness and imaging study for semiconductor applications*. J. Vac. Sci. Technol. B Microelectron. Nanom. Struct. Process. Meas. Phenom. **25**, 2547–2552 (2007), doi:10.1116/1.2794319.

75. Q. Wan, K.J. Abrams, R.C. Masters, A. Talari, I.U. Rehman, F. Claeyssens, C. Holland and C. Rodenburg: *Mapping Nanostructural Variations in Silk by Secondary Electron Hyperspectral Imaging*. Adv. Mater. **29**, 1703510 (2017), doi:10.1002/adma.201703510.

76. A. Khursheed: Scanning electron microscope optics and spectrometers, 1st ed., (World Scientific Co Pte, Singapore, 2010).

77. R.C. Masters, A.J. Pearson, T.S. Glen, F.-C. Sasam, L. Li, M. Dapor, A.M. Donald, D.G. Lidzey and C. Rodenburg: *Sub-nanometre resolution imaging of polymer-fullerene photovoltaic blends using energy-filtered scanning electron microscopy*. Nat. Commun. **6**, (2015).

78. K.J. Abrams, Q. Wan, N.A. Stehling, C. Jiao, A.C.S. Talari, I. Rehman and C. Rodenburg: *Nanoscale Mapping of Semi-Crystalline Polypropylene*. Phys. Status Solidi **14**, 1700153 (2017).

79. Y. Liu, J. Zhao, Z. Li, C. Mu, W. Ma, H. Hu, K. Jiang, H. Lin, H. Ade and H. Yan: *Aggregation and morphology control enables multiple cases of high-efficiency polymer solar cells*. Nat. Commun. **5**, 5293 (2014), doi:10.1038/ncomms6293.

80. D.C. Bell: *Contrast mechanisms and image formation in helium ion microscopy*. Microsc. Microanal. **15**, 147–153 (2009).

81. D. Hasselkamp: *Kinetic electron emission from solid surfaces under ion bombardment*, in: D. Hasselkamp, H. Rothard, K.-O. Groeneveld, J. Kemmler, P. Varga, H. Winter (Eds.): *Particle Induced Electron Emission II*, (Springer, Berlin, Germany, 1992), pp. 1–95, doi:10.1007/BFb0038298.

82. R. Noriega, J. Rivnay, K. Vandewal, F.P. V Koch, N. Stingelin, P. Smith, M.F. Toney and A. Salleo: *A general relationship between disorder, aggregation and charge transport in conjugated polymers*. Nat. Mater. **12**, 1038 (2013), doi:10.1038/nmat3722.

83. H.-E. Joe, W.-S. Lee, M.B.G. Jun, N.-C. Park and B.-K. Min: *Material interface detection based on secondary electron images for focused ion beam machining*. Ultramicroscopy **184**, 37–43 (2018), doi:10.1016/j.ultramic.2017.10.012.

84. J. Ferrón, R.A. Vidal, N. Bajales, L. Cristina and R.A. Baragiola: *Role of HOPG density of empty electronic states above vacuum on electron emission spectra induced by ions and UV photons*. Surf. Sci. **622**, 83–86 (2014).

85. D. Fox, Y.B. Zhou, A. O'Neill, S. Kumar, J.J. Wang, J.N. Coleman, G.S. Duesberg, J.F. Donegan

and H.Z. Zhang: *Helium ion microscopy of graphene: beam damage, image quality and edge contrast*. Nanotechnology **24**, 335702 (2013).

86. C.J. Barnett, C.E. Gowenlock, K. Welsby, A. Orbaek White and A.R. Barron: *Spatial and Contamination-Dependent Electrical Properties of Carbon Nanotubes*. Nano Lett. **18**, 695–700 (2017), doi:10.1021/acs.nanolett.7b03390.

87. A. Hoffman: *Fine structure in the secondary electron emission spectrum as a spectroscopic tool for carbon surface characterization*. Diam. Relat. Mater. **3**, 691–695 (1994).

88. A.J. Pearson, S.A. Boden, D.M. Bagnall, D.G. Lidzey and C. Rodenburg: *Imaging the bulk nanoscale morphology of organic solar cell blends using helium ion microscopy*. Nano Lett. **11**, 4275–4281 (2011).

5 Instrument parameterisation and sample preparation and data analysis for successful spectral imaging

In the course of this project, many practical hurdles were encountered and resolved. In the following chapter the results of this instrument and imaging optimisation process are presented as a guide for future projects, and perhaps more generally to demonstrate the theoretical and practical significance of the optimisation results, and the effectiveness of some of the methods developed in the process.

This chapter first reports the findings of the instrument parameterisation on model materials. As discussed in detail in the introduction, special care needs to be taken when choosing parameters for low-voltage SEM [1–5], even more so when samples are exposed to higher doses during SE spectral acquisition. Various imaging parameters have been observed to affect imaging and spectra of uncoated insulators, and in the following these parameters are varied systematically to elucidate their significance and further recommend optimal settings. Besides the materials of interest to the project aims, model materials with known properties were investigated. Here, highly oriented pyrolytic graphite (HOPG) was chosen as a well-studied conductive carbon allotrope [6], and carbon fibre was chosen for its geometry and dimensions akin to spider silk, while its conducting properties make it more stable under the electron beam.

The chapter concludes with its key result—a recommended workflow for modern high-resolution low-voltage scanning electron microscopy and secondary electron spectroscopy of insulating polymers.

5.1   Instrument Parameterisation

The importance of the SEM instrument parameters on the beam–sample interaction and the resulting image were recognised in the early days of low–voltage SEM, even before the user was given easy control over all such parameters [1–5]. They include the primary electron beam accelerating voltage (E_0), the electron beam current (I_0) and the resulting electron dose to the sample, the working distance, and the sample topography and orientation. Recommendations for optimum image quality have been made in the past [3], but their effect on the secondary electron spectrum is not sufficiently characterised. A further parameter of specific interest to this project is the secondary electron spectral acquisition method, which has direct impact on the sample dose.

5.1.1   The primary electron beam accelerating voltage—E_0

As discussed in detail in the introduction and literature (Chapter 2), it is desirable to adjust the primary beam accelerating energy (E_0) to be close to the second crossover energy (E_2) for insulating samples where the injected, emitted and conducted charge are in balance and the minimum amount of charging occurs. The secondary electron spectrum reveals energy dependent differences in SE yield with E_0, as shown in **Figure 5.1.**
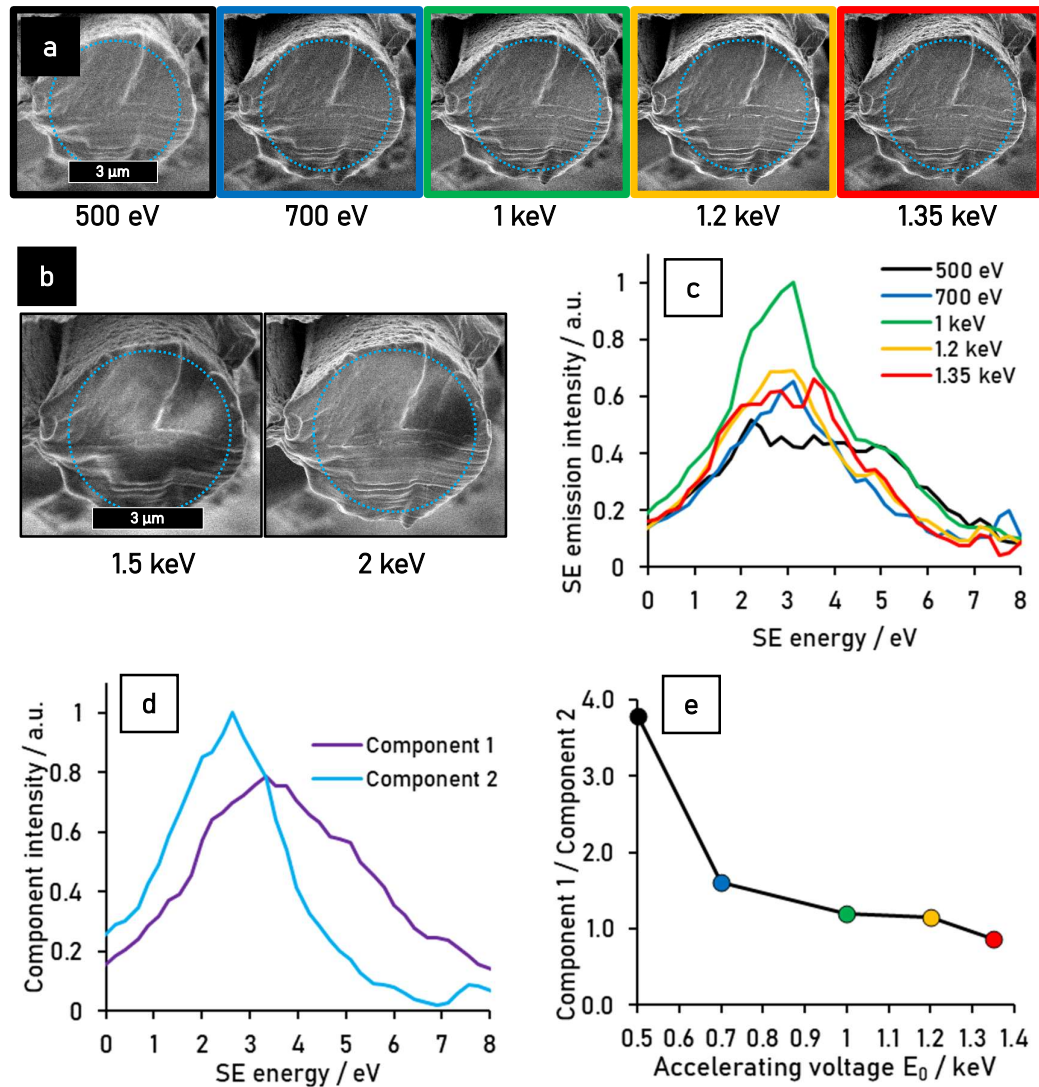
Figure 5.1: Effect of primary beam voltage E_0 on *Nephila edulis* spider silk cross-sections imaged in the Helios SEM at room temperature and 6.3 pA beam current a) Increased image quality with increasing E_0 in the range 500 eV to 1.35 keV, b) positive charging evident at 1.5 and 2 keV c) secondary electron spectrum from the regions of interest indicated by the blue dashed circle with increasing keV d) the two spectral component solution of a NMF multivariate analysis using a point spread function with a standard deviation of 0.5 px in the space, and 0.11 eV in the energy dimension and e) the ratio of component 1 / component 2 with increasing E_0

Spider silk cross-sections cryo-snapped and imaged at room temperature were systematically imaged at different accelerating voltages. The comparison of SE images with accelerating voltages in the range of 500 eV to 2 keV shows that the image quality is optimal in a window between 1–1.35 keV (**Figure 5.1 a–b**). The lower the beam energy, the more precise the electron optics need to be to focus the 'slow' beam, and so the

image resolution degrades below 1 keV for this specific instrument and sample due to instrumental limitations [2,7].

Above 1.35 keV charging occurs inhomogenously across the cross-section, with diffuse areas of reduced image brightness indicating positive charging (**Figure 5.1 b**). Theoretically, as E_0 increases significantly above 1 keV, the overall surface charge should become overall more negative due to the decreased SE yield and emissions. However, it is also well established that surface charging phenomena are dynamic and dependent on many complex factors [4,8,9]. Thus, areas of different overall charging potentials are observed in **Figure 5.1 b**, which degrade image quality and certainly prohibit reliable spectral acquisition. The loss of image stability due to charging at higher E_0 may be a result of the larger interaction volume: charge build-up can occur further below the surface, resulting in poorer charge dissipation and increased fields observed on the surface. Thus, the general rule that E_0 can be increased to counteract positive charging (as proposed by Joy and Joy [3]) does not apply in this case, and images without positive charging artefacts are instead acquired at lower E_0.

From the images alone, one may presume that the optimal imaging window ranges from 1 keV to 1.35 keV, however the spectra show significant variation with E_0 in the range of 500 eV to 1.35 keV. The spectra shown in **Figure 5.1 c** were obtained at the same brightness and contrast settings so that the spectral intensity at a given energy can be compared in relative terms within the data set. The spectrum at E_0 = 1 keV (green) stands out due to its sharp peak at 3.1 eV and its overall higher intensity SE emission. This is consistent with the finding that the maximum secondary electron yield of carbon occurs at 1 keV [3,5], assuming that carbon is most suitable reference material for characterising spider silk SE yield behaviour.

To systematically characterise the difference between the spectra with E_0, a non-negative matrix factorisation (NMF) was performed as a multivariate analysis on the

five spectral data sets presented in **Figure 5.1 d**, as detailed in Chapter 3. The results suggest that the spectra are best described by a combination of a broader curve at higher energy with a peak at 3.3 eV (component 1 in purple) and a sharper curve with a peak at 2.6 eV (component 2 in blue), whereby component 1 is dominant at lower E_0 and component 2 becomes increasingly prominent at larger E_0, as shown by the component 1 / component 2 ratio plotted in **Figure 5.1 e**. The increase of the lower energy component with increasing E_0 may be a result of the complex charging behaviour which manifests in the images above 1.35 keV. This signifies—perhaps not surprisingly—that the SE spectrum is sensitive to surface charging phenomena which are invisible in regular SE images, and that one may make use of this for image and spectral optimisation.

A number of other factors may influence the evolution of spectral components with E_0, for example it may be expected that the SE1 / SE2 ratio is increased at lower accelerating voltages due to the lower backscatter yield at low E_0 [3], and that these may each have distinct contribution to the spectral components. Furthermore, the spectra were recorded starting with the E_0 = 1.35 keV and decreasing values of E_0, meaning that the progression of the component ratio may also reflect the lower overall dose which the cross-section has been subjected to with increasing E_0. Exact characterisation of these factors would require a dedicated experimental set-up and may only be presumed here.

Nonetheless, the results show that for optimal spectral acquisition in this case, a balance between image quality and sample stability is achieved between 1–1.35 keV, whereby the increased overall yield and spectral intensity at 1 keV make it the most favourable setting for this project. It is also clear that the accelerating voltage must be consistent throughout the dataset in order to obtain comparable spectra. An experimental assessment of the optimum parameters akin to the one performed here

is advisable for new samples and imaging conditions, as theoretical approaches can explain basic trends qualitatively, but not without fail, as discussed above. Attempts to numerically quantify secondary electron emission behaviour are complex even for simple systems [1], but tables of experimental E_2 values for polymers and other insulators are available and a good reference point [1,3]. Indeed for Nylon-6, a synthetic polymer with molecular similarity to the proteinaceous spider silk, the E_2 value was measured at 1.2 keV, which may explain the overall image stability around this E_0 value [1].

1 keV   1.2 keV   2keV
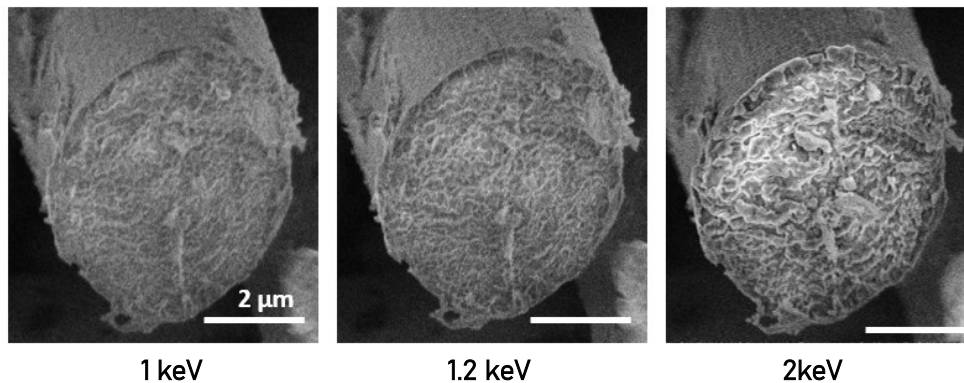
Figure 5.2: Selection of information content between nanostructure and edge effect using E_0. *Nephila edulis* spider silk imaged in the Helios SEM at -180 ℃ and with a beam current of 6.3 pA.

As spider silk is a soft material prone to plastic deformation at room temperature, some SEM observations were performed at cryogenic temperatures to induce brittle fracture and observe structurally unchanged cross-sections. Indeed, as **Figure 5.2** shows, the surface appears rougher and perhaps more structurally preserved than in the room temperature observations, confirming that there are advantages to cryogenic observations. The implications of cryo-SEM and its sample preparation are further discussed in detail below. For the sake of this discussion of imaging parameters it is important to note that the charging behaviour has evidently changed as a function of temperature: whereas the room temperature cross-section exhibits large patches of

positive charging at E_0 > 1.35 keV, this is not the case at cryogenic temperatures even at 2 keV, where inhomogenous brighter areas indicate the presence of negative charging. The conductivity to ground, the secondary electron emission and potentially other significant beam-sample interactions may all be influenced by the drop from room to cryogenic temperature, making theoretical treatments of image stability with temperature too complex for this system, and so direct observations remain the best way to optimise E_0.

Besides mitigating charging, the accelerating voltage series shown in **Figure 5.2** also illustrates another important consideration when selecting E_0: At lower kV the edge effect is supressed due to the smaller interaction volume [10], and contrast is more likely to arise from local nanostructural and compositional differences in the material. Thus, while the 2 keV image has the most favourable resolution, the edge effect overshadows the nanostructural information sought. For this particular sample and imaging conditions an E_0 of 1.2 keV appears to be a good compromise between resolution and access to compositional contrast.

In summary the optimal accelerating voltage for spectral imaging and nanoscale mapping must be determined on a case-by-case basis. The material's experimental second crossover energy E_2 is a good starting point if available. Depending on the instrument and sample, lowering E_0 below the optimal degrades image resolution, whereas increasing E_0 may eventually lead to detrimental charging effects. While the image quality seems to respond sensitively even to small changes in E_0 (in the range of 150 eV and less), it was found throughout a range of samples that there is a window of opportunity for high image quality and a stable sample—usually in the 700 eV to 1.2 keV range.

5.1.2   Dose

The electron dose per image (D_{img}) which the sample is subjected to depends on many parameters. Generally, it is expressed through an overall charge exposure, given by the product of the beam current I_0 and the total exposure time t_{total} per area A, whereby typical quoted units are coulombs per metre squared (C m^{-2}):

$$D_{img} = \frac{I_0 \times t_{total}}{A}$$
              Equation 5.1

Considering that the overall exposure time during image acquisition is defined by the scanning parameters such as dwell time (t_{dwell}), the number of pixels (n_{px}) and the number of image integrations (n_{int}):

$$t_{total} = t_{dwell} \times n_{px} \times n_{int}$$
              Equation 5.2

Equation 5.1 may be modified as follows:

$$D_{img} = \frac{I_0 \times t_{dwell} \times n_{px} \times n_{int}}{A}$$
              Equation 5.3

For successful LV–SEM observation and secondary electron spectral acquisition these parameters must be considered carefully.

5.1.2.1   *Beam current—I_0*

While E_0 determines the energy of the impacting electrons and influences the average charge resulting from electron impact, the beam current I_0 determines how many electrons impact the sample and thus the magnitude of charge injected into the surface. In the instrument, the beam current may be controlled using different apertures and condenser lens settings, which only pass a portion of the electrons generated by the gun onto the sample.

Modern systems specify the current value which specific settings ought to supply, whereas older systems may give these settings different descriptions such as 'spot size' to avoid giving absolute current values since these may fluctuate throughout the lifetime of an electron gun. Absolute beam current values may be measured experimentally using a faraday cup [11], where all beam charge is absorbed and measured by a current probe.
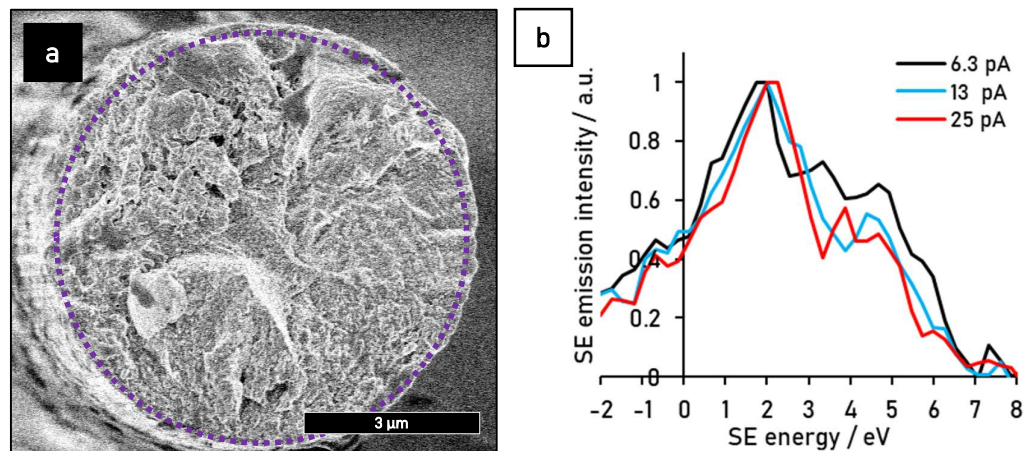

Figure 5.3: a) Detail of carbon fibre cross-section imaged in the Helios SEM at 1 keV and 13 pA beam current b) carbon fibre spectra of the same cross-section recorded at different beam currents, the region of interest included in the spectra is indicated by the purple dashed circle.

In the modern FEI Helios SEM absolute beam current values can be chosen directly. **Figure 5.3 b** shows normalised spectra acquired using different current settings. There are no large systematic changes with current in the case of this carbon fibre cross-section, which demonstrates that the sample is in a dynamic charge balance at the chosen parameters.

It is nonetheless not advisable to select beam currents larger than the minimum required for obtaining sufficient signal, as increased currents and the resulting increased SE emission are known to favour deposition processes which would obscure the surface [12,13]. Additionally, more beam-sensitive materials may benefit from lower currents due to other dose driven processes such as sample damage.

5.1.2.2   Magnification—field width—A

The image magnification directly affects the area A which is exposed to the electron beam over the acquisition of an image. Doubling magnification means that the same total charge is supplied to a quarter of the image area, and consequently a fourfold image dose is reached. It must thus be balanced against the desired spatial resolution for nanoscale applications, especially as magnification is perhaps the most crucial parameter in obtaining the maximum spatial resolution achievable for a given sample and instrument.

The use of magnification in absolute terms can lead to confusion as it describes the ratio of the actual size of the object of interest, and its size in the displayed image. With digital media absolute magnification values are especially unhelpful, as different screen resolutions and zoom factors change the effective magnification value of an image. Instead, magnification will be discussed here as the horizontal field width (HFW) which the image displays.
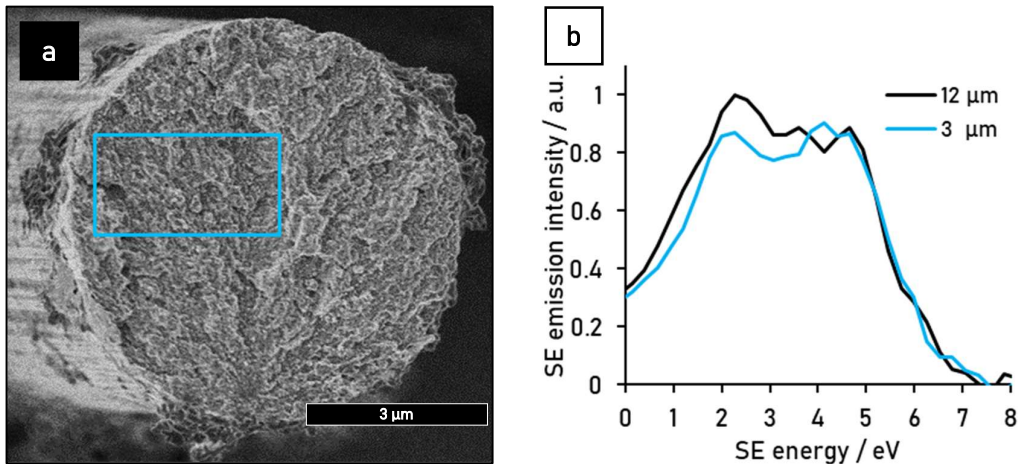

Figure 5.4: Effect of magnification on the spectrum of the same field of view on a carbon fibre cross-section imaged in the Helios SEM at 1 keV and and a beam current of 25 pA a) Image of cross-section showing the spectral measurement region framed in blue b) spectra of the framed region when collecting the image at 12 μm (black) and 3 μm horizontal field width (blue)

Figure 5.4 displays the two spectra collected from the exact same window (shown in blue) on a carbon fibre cross-section, at 12 μm (black, acquired first) and at 3 μm HFW (blue, acquired second). Due to the factor 4 between the magnifications the blue curve represents the spectrum at 16-fold dose exposure. The overall intensity and width of the spectra are similar, however there are some changes in the peak which can be linked to dose effects. Specifically, the major peak at 2.2 eV decreases in intensity, while increased electrons of approximately 4.5 eV are emitted. This is consistent with the formation of surface contamination, of which the spectrum has been published recently [6]. Due to the square relationship between increased magnification and increased dose, special care needs to be taken not to image at unnecessarily high magnifications where these are not required.

5.1.2.3   Scanning Parameters—Scan Interlacing, Dwell Time, and Image Integration

Scanning parameters such as scan interlacing do not directly affect the image dose D_{img}, but instead influence the spatiotemporal dose rate which a sample volume is exposed to over a certain time. This is a parameter which is much more difficult to define than D_{img} itself. The question "How long does it take an irradiated sample nano-volume to relax to a ground state in an SEM" is a complex one, as secondary electrons are emitted within femtoseconds [14], but the time limiting factors are the charge transport dynamics of the insulating sample, which depend on the resistivity and defect sites of the sample material [15], and are difficult to quantify for natural structural materials. For insulating SiO_2 it has been shown that beam exposure of 25 ns is enough to significantly change the surface potential and lower the secondary electron yield at the exposure centre, i.e. the centre of the SEM beam spot [15]. This strongly supports the idea that irradiating an adjacent second pixel before the first has had time to relax exacerbates charge build-up and sample damage processes. As the pixel is probed by the electron beam spot, the spot size (or probe size) is also important. If the probe size is larger in space than one pixel, certain surface areas and furthermore sample nano-volumes will be irradiated multiple times in quick succession, favouring undesired charge build-up and sample damage processes especially in insulators. Unfortunately, the probe size is rarely reliably known in the SEMs, and may vary significantly with different parameters.

Scan interlace = **1 (default)**
32.4 nm between scan lines

Scan interlace = **2**
64.8 nm between scan lines

Scan interlace = **4**
130 nm between scan lines

Scan interlace = **8**
259 nm between scan lines
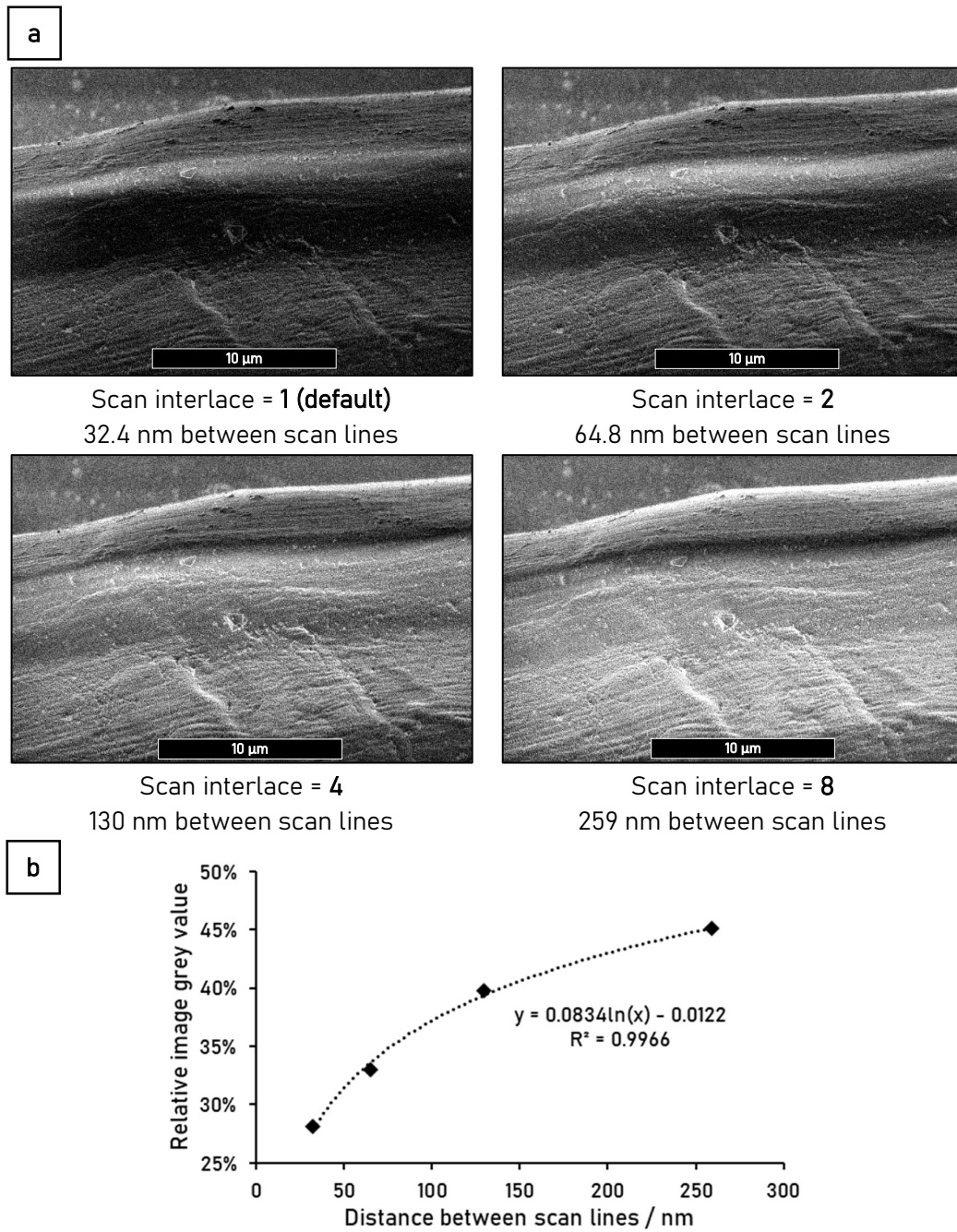
$$y = 0.0834\ln(x) - 0.0122$$
$$R^2 = 0.9966$$

Figure 5.5: a) Ramie nettle plant fibre surface secondary electron images acquired in the Nova SEM at 1 keV and 3 mm working distance b) Plot illustrating the increase in brightness and thus secondary electron yield with the use of increasing scan interlacing on positively charging samples

One way of counteracting the spot overlap during the scan is by the use of scan interlacing. The scanning coils of the SEM can be directed to skip a certain number of scan lines, and thus effectively a distance in real space, to return to them after the bottom of the image is reached. For example with a scan interlace of 2, every second line is skipped so that at first all lines defined by an odd y-resolution values are scanned, before in a second pass over the field of view the even y-resolution values are scanned. Effectively, this spreads out the beam exposure in time and space. **Figure 5.5** exemplifies the benefits of using scan interlace: From the images of this uncoated cellulosic ramie plant fibre positive charging, evident as dark horizontal bands, reduces as the scan interlace spacing is increased. Furthermore, the amount of positive charging can be quantified within the dataset by measuring the average brightness of the image, while keeping all other image acquisition parameters constant. The assumption is made that the brightness is proportional to the secondary electron yield and so the increasing image brightness evident in the series is associated with a decrease in positive surface charge as a result of the more favourable interlaced scanning pattern. Although no absolute charging or SE yield values may be determined from this data set, the increase in brightness with the increase in interlace setting follows a logarithmic relationship, implying that the amount of positive charging caused through imaging two pixels in close vicinity may be governed by a power law.

The availability of interlace scan settings on the Nova SEM only allow the investigation of four interlace distances in the vertical direction, but a more comprehensive study may investigate the effect of a horizontal scan interlace (skipping pixels within the line) as well to continue this work. In taking this idea further, the investigation of spatial and temporal relaxation of insulating samples after electron spot exposure could lead to the development of minimal spatiotemporal scan recipes, where the beam jumps across the field of view, keeping a maximum distance in time and space from all other

spots. However, such (perhaps no longer) scanning patterns could significantly delay the image acquisition, and it is furthermore not clear whether the beam could be blanked while the scanning coils direct the beam to the next point in space to avoid unnecessary exposure of the sample to the beam. The relatively novel EM field of ultrafast (scanning) electron microscopy may offer practical solutions, as femtosecond pulsed electron beams have been realised, albeit for higher electron voltage applications [16,17].

It has been demonstrated and argued that is favourable to spread the electron beam exposure as much as possible in time and space. It follows that the dwell time of the beam should also be minimised, as proposed as early as 1995, while the increased amount of shot noise present in lower dwell time images can be compensated by multiple image integration [1]. However, there are limitations—instrument vibration and stray fields may cause drifts over time, and this has forced the user to choose higher dwell times to maintain resolution at the cost of a slightly distorted image, whereby slower dwell times can cause severe blurring and thus poorer resolution in integrated images. The solution to this problem comes in the form of modern image capture systems, which include live drift correction: one image is captured and before it is combined with another to increase the overall collected signal and reduce the noise, the two are digitally overlaid to match spatially thus correcting any drift which may have occurred between acquisitions. The availability of such image processing tools on the instrument is invaluable for low-voltage applications, as it means the dwell time can be set to the absolute minimum available on the instrument (50 ns in the Nova and Helios) and the required signal to noise can be achieved by image integration without subjecting small sample volumes to intolerable dose rates.

The imaging and secondary electron spectral measurements of insulating systems benefit from applying scan interlacing as much as possible, while minimising dwell

time. Image integration may be used to increase the signal to noise ratio, especially if

digital drift correction is available.

5.1.2.4   Spectral evolution with dose

As the spectra in this project are acquired in serial acquisition rather than parallel

acquisition, a spectral data set is composed of n_{spec} images. Thus the spectral dose D_{spec}

amounts to

$$D_{spec} = D_{img} \times n_{spec}$$ **Equation 5.4**

whereby the number of spectral images is defined by the spectral energy range E_{max} -

E_{min} and the energy difference between two spectral images ΔE

$$n_{spec} = \frac{E_{max} - E_{min}}{\Delta E}$$ **Equation 5.5**

and thus

$$D_{spec} = \frac{D_{img}\,(E_{max} - E_{\min})}{\Delta E}$$ **Equation 5.6**

It follows that if the spectral dose D_{spec} is to be minimised the image dose D_{img}, then the

spectral range E_{max}–E_{min} and the size of the energy step ΔE all compete against each

other in acquiring a high-quality spectrum within a tolerable overall dose. Furthermore,

ΔE may be negative or positive, signifying the scan direction collecting increasing or

decreasing SE energies.

To determine whether the dose affects the spectrum during acquisition, repeat spectra

may be acquired (as presented in Chapter 4 [18]), using the result of the measurement

itself as an indication of measurement-induced changes. Using highly oriented pyrolytic

graphite (HOPG) as a reference material, a multivariate component analysis was

performed using the non-negative matrix factorisation (NMF) algorithm to track the evolution of the different components with increasing dose during multiple spectral acquisitions of the same field of view (FOW), the results of which are shown in **Figure 5.6**.
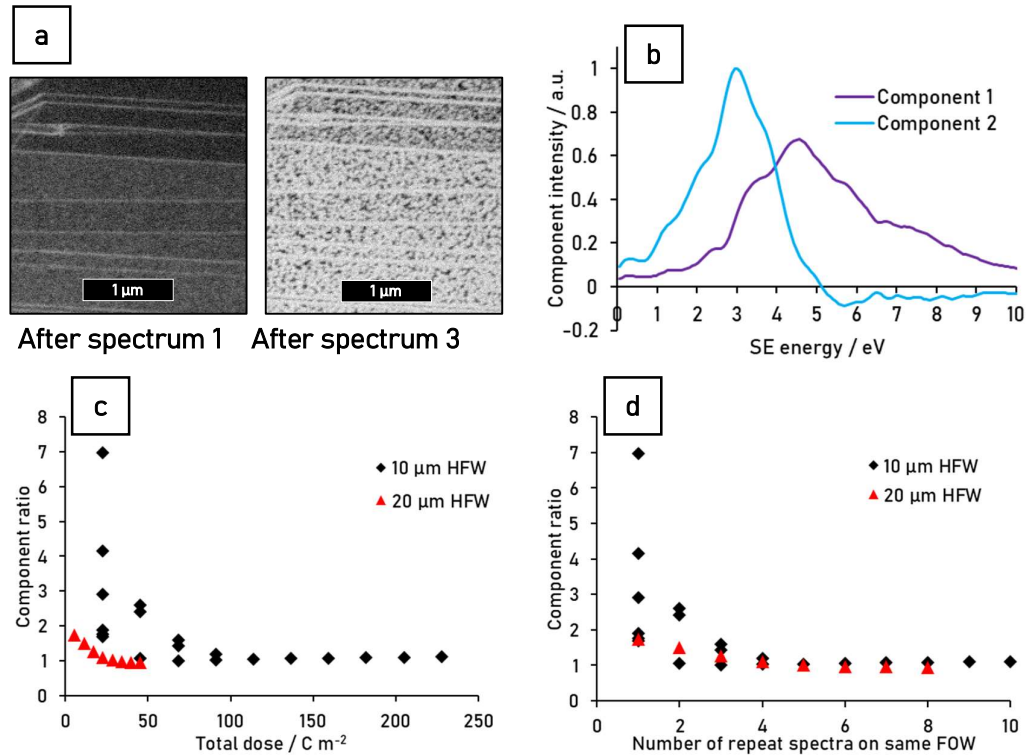

Figure 5.6: Effect of increasing dose during repeat spectral acquisition of HOPG surface in the Nova SEM collected at E_0 = 1 keV, I_0 = 16 pA and a working distance of 2 mm a) growth of contamination on the surface with increased number of spectra taken b) Components isolated from 39 spectra of different areas and dose exposures by a NMF algorithm applying a point spread function of 0.5 px in the space and 0.21 eV in the energy dimension c) Evolution of the component 1/component 2 ratio with increasing total dose at 10 and 20 μm horizontal field width (HFW) d) Evolution of the component 1/component 2 ratio at 10 and 20 μm with increasing number of spectra recorded on the same field of view (FOW).

From AFM results recorded on this same data set it is known that increased beam exposure results in the deposition of a contamination layer through the mechanism of electron beam induced deposition (EBID) [6], and its effect on the image brightness is exemplified in **Figure 5.6 a** where secondary electron images were taken after the acquisition of an increasing number of spectra. The multivariate component analysis

was performed by inputting 39 spectral datasets recorded on the same sample across different areas with a number of systematically varied conditions—specifically those affecting dose—to understand the effect of these parameters on the spectra. The NMF solution with two components shown in **Figure 5.6 b** outputs component 1 (purple) as a broad higher energy component which peaks at 4.7 eV, whereas component 2 (blue) has a sharper peak at 3 eV and overall higher intensity at lower energies. To characterise the evolution of the HOPG spectrum with increasing beam exposure, the ratio of component 1 over component 2 was plotted in **Figure 5.6 c** as a function of dose. From the results of the multivariate analysis it is clear that component 1 represents the freshly exfoliated surface, with component 2 contributing very little to the overall spectrum when the dose is low. The component ratio decreases rapidly even after 1 spectral acquisition and flattens out at a value of about 1, where both components describe the spectrum equally, and the spectrum now completely reflects the deposited contamination layer. It is curious to note that the limiting dose at which this occurs is different for spectra acquired using a higher magnification 10 μm horizontal field width (HFW, black diamonds) and a lower magnification 20 μm HFW (red triangles), with about 100 and 50 C m^{-2} respectively. This is unexpected, as it suggests that dose is not the only factor governing growth of contamination. When plotting the number of spectra acquired on the same area against the component ratio, both the 10 and 20 μm HFW spectra fall onto one curve as shown in **Figure 5.6 d**, suggesting that the number of spectra recorded on the same field of view (FOW)—and thus the total time which the FOW has been exposed to the electron beam—explains the spectral evolution better than simply the dose. What this suggests then, is that in this case the contamination build-up on the HOPG surface up is time-limited, so that an increase in dose does not lead to increased contamination build-up unless it has been illuminated by the electron beam for a longer period of time. This is an important consideration for beam-sensitive

materials, as it illustrates the complexity of beam-surface interactions and highlights the need to understand processes to successfully control them. In this case, simply lowering the dose D_{img} and D_{spec} evidently does not delay the formation of a contamination layer. Instead, time is the crucial factor and so an optimisation looking to minimise n_{spec} would be more successful in minimising contamination build-up.

Another spectral collection parameter to keep in mind is the direction of acquisition—whether the images are collected with incremental or decremental energy steps. **Figure 5.7** demonstrates the difference this can make in a beam-sensitive system: When a spectrum is recorded on a fresh carbon fibre cross-section from 0–8 eV (black curve), a prominent peak is measured at 2 eV, which has degraded by the time the reverse measurement has reached it (red curve). Ideally, only minute changes to the system would occur during the entire spectral collection, and so current, spectral range and energy steps could be further optimised for this sample. However, it is generally favourable in this detection system to collect with incremental eV steps, as the higher and more characteristic spectral intensities typically lie at lower energies.
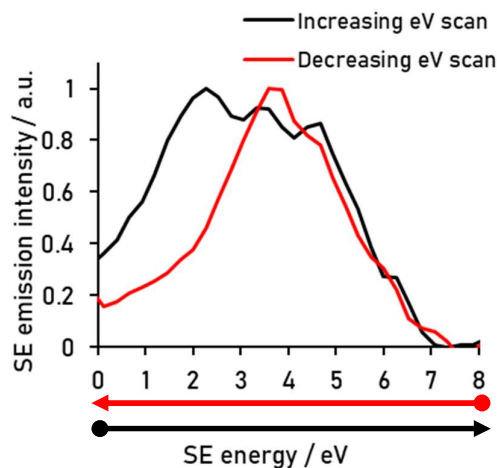

Figure 5.7: Difference arising in the secondary electron spectrum when scanning the spectrum of a carbon fibre cross-section in the Helios at $E_0 = 1$ keV and $I_0 = 25$ pA scanning in the direction of increasing SE energy (black), and decreasing SE energy (red).

A further strategy of limiting beam exposure is the use of 'explorative' spectra collected at larger ranges and larger energy steps, in order to determine the response of the sample to the beam and which energies are of specific interest. In subsequent measurements the overall dose can be reduced by limiting the collection range, or the energy resolution may be increased through smaller energy steps. Throughout this project it was observed that while the Nova SE spectra showed higher resolution spectra, all peaks in the Helios system appear broad, even though the energies of peaks are precise and reproducible. In a system such as the Helios there is no merit in oversampling energies by choosing steps smaller than the resolution limit enforced by the detection system, so the energy step was kept at $\Delta E = 0.21$ eV whereas energy steps down to 0.07 eV were used for the Nova system.

5.1.3   Working distance—WD

The term working distance describes the distance between the pole–piece—the last electromagnetic lens—and the focal point of the beam on the sample. To increase the working distance, the stage and with it the sample are lowered in the chamber. Thus, the working distance determines the overall distance between the signals emanating from the sample and the detectors, which remain in their fixed position. When the detector is further from the sample, secondary electrons are increasingly unlikely to be detected if they are emitted at an angle away from the detector. Additionally, as SE detectors actively attract SEs by applying a field, the higher the energy of an off–axis SE, the less likely it is to be deflected sufficiently to reach the detector.
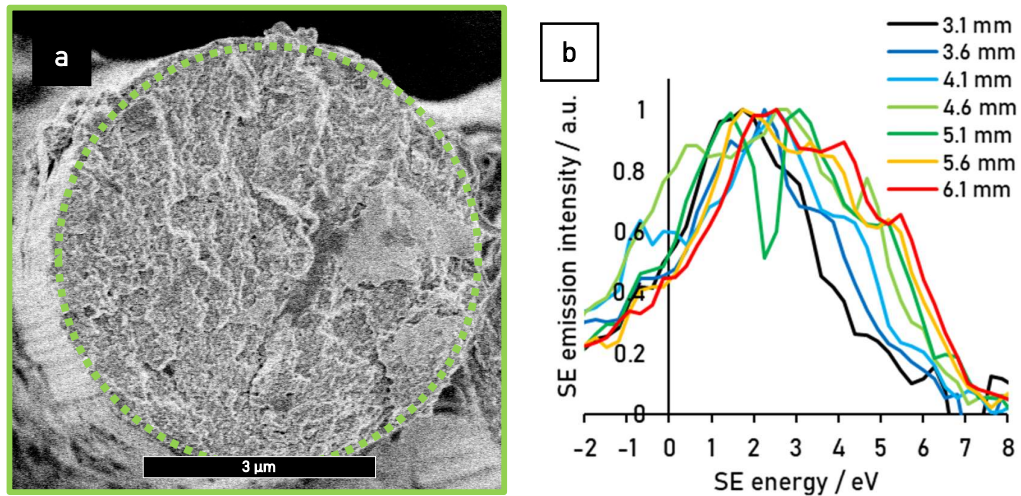
Figure 5.8: a) Carbon fibre imaged in the Helios SEM at 4.1 mm working distance, 1 keV and 25 pA, the measured region of interest is shown by the green dashed circle b) Effect of working distance on the spectra of the same cross-section

Figure 5.8 demonstrates the behaviour of carbon fibre spectra with working distance in the FEI Helios through-lens detection system. Clearly, in the Helios SE energy filter there is a cut-off energy at 3.5–7 eV, which increases with working distance. This can be rationalised through the reduction of the angular collection efficiency of higher energy SEs as the sample comes closer to the pole-piece where the detector lies [19]. The change in angular acceptance of SEs with working distance has important implications for the interpretation of spectra arising from this system, as the working distance governs which energy SEs can be reliably collected. In the Helios system used here a working distance of 4.1 mm is recommended by the manufacturer, as it is the eucentric height—the working distance where the field of view does not shift if the sample stage is tilted—which is important for many instrument functions. At this commonly used working distance of 4.1 mm, this cut-off value lies at about 6 eV.

The working distance dependence of the spectrum must be understood as a limitation of the system, as the gradual energy cut-off means that some energies are more reliably collected than others, and that emission intensity values will not be proportional to the actual number of secondary electrons emitted across the energy

range. This means that yields may only be discussed in relative terms so long as care has been taken to keep the working distance and brightness and contrast settings constant between samples.

5.1.4 Topography and beam incidence angle effects

It is well known that the secondary electron signal responds to topography. This is mostly due to edge and detector shadowing effects, but the sample topography can affect the secondary electron emissions in multiple more ways, for example the angle of an imaged surface relative to the primary beam affects secondary electron emission yields [5]. In the case of large (microscale) topography, the trajectory of electrons could prevent them from reaching the detector, and instead colliding with a different part of the sample. Furthermore, it has been observed throughout this project that exposure of insulating samples of micron to millimetre scale irregular surface geometry can lead to the formation of fields, which may change the surface potential of the material and deflect the emitted secondary electrons.
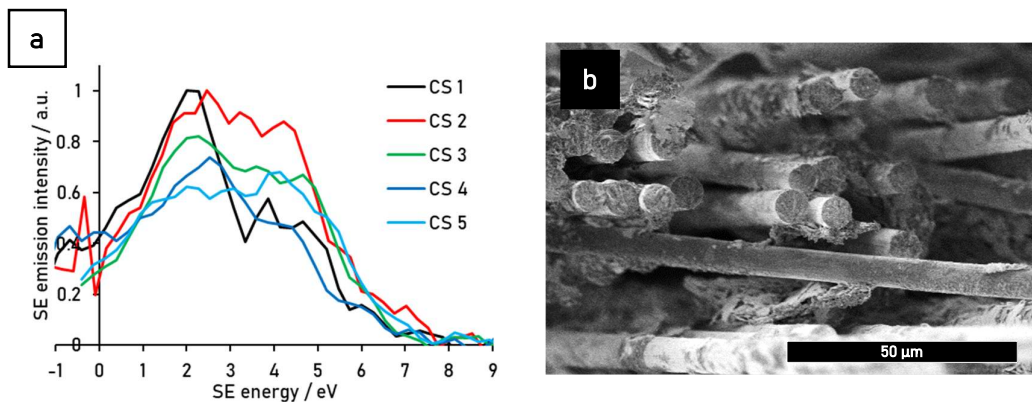

Figure 5.9: a) Variation in spectra between different carbon fibre cross-sections (CSs) of the same cryo-snapped sample imaged in the Helios SEM at room temperature with E_0 = 1 keV and I_0 = 25 pA b) Overview of the cryo-snapped sample showing macroscale topography and varying heights of the imaged cross-sections.

The presence of macroscale topography affects the spectra as illustrated in **Figure 5.9 a**. The curves shown in **a** represent spectra taken from different cross-sections of the cryo-fractured and room-temperature imaged carbon fibre pictured in **b.** The results were obtained on different dates, but with image and spectral collection parameters kept the same and without exposing the cross-sections to the electron beam prior to the measurement to eliminate dose effects causing differences in the spectra. It was found that different cross-sections, which are known to have the same composition, may produce a range of secondary electron emission spectra, although they share some similarities: two peaks are prominent throughout the dataset, one at approximately 2.0 eV and one at 4.3 eV, although the intensities vary significantly. The different intensities of the two peaks may be due to secondary electrons getting diverted on their way to the detector, either by colliding with another part of the sample or by the presence of fields, which would affect lower energy SE more.

It may be proposed that the spectra with lower overall yield come from cross-sections in less favourable positions. This poses a challenge for conducting broad investigations into cross-sections of materials, if not even a well-characterised and single element material such as carbon fibre can reproduce the same spectra reliably. The solution to this problem lies in eliminating micron scale topography and resulting fields as much as possible by fracturing materials in plane with the matrix and imaging a planar surface. Strategies of achieving this are discussed further in the following chapter.

Besides the effect of macroscale topography on fields around the sample and thus the spectrum of the cross-sections, it is also known that the beam impact angle influences the SE emission behaviour [5]. In this work, this was investigated systematically using a single cross-section and by tilting the stage, pivoting on the x-axis to obtain spectra at different angles as shown in **Figure 5.10 a**. Note that 0˚ denotes the case in which the primary beam is at normal incidence to the cross-section's surface.
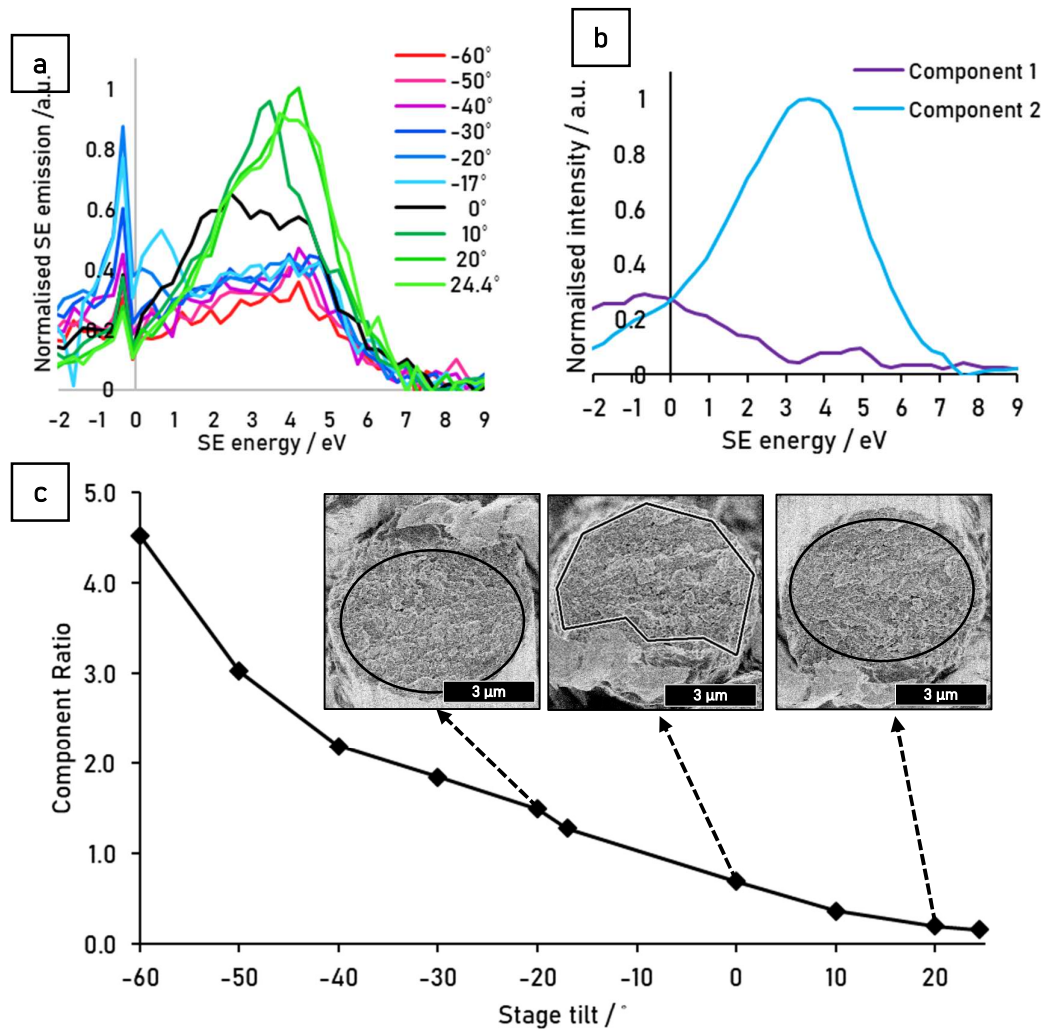
Figure 5.10: Effect of stage tilt on a carbon fibre cross-section in the Helios SEM recorded at $E_0 = 1$ keV and $I_0 = 25$ pA a) Spectra averaged of the surface of the carbon fibre cross-section for different angles b) Two-component solution of a NMF multivariate analysis using a point spread function with a standard deviation of 0.5 px in the space, and 0.13 eV in the energy dimension c) Change of the component 1 / component 2 ratio with stage tilt angle. The inset images illustrate the direction of the tilt and the region of interest included in the measurement

To deconvolute the effect of tilt angle on the spectrum a multivariate analysis using the non-negative matrix factorisation algorithm was performed, inputting the 10 spectral datasets and solving for two components. The results are shown in **Figure 5.10 b**, with Component 1 being generally atypical in shape, with intensity below 0 eV and broad low intensity peaks at about 4 and 5 eV. Component 2 represents a more typical higher intensity spectrum resembling a relatively broad gaussian curve with a peak at 3.7 eV.

The component 1 / component 2 ratio is plotted against the stage tilt angle in **Figure 5.10 c** to reveal a steady decrease in the contribution of component 1 to the overall spectrum, while the higher intensity component 2 becomes more prominent. Note that the spectra were recorded in the order 0˚, 10˚, 20˚, 24,4˚, –10˚, –20˚, …, –60˚, so that the steady trend of the plot is independent of acquisition order and dose effects. If the detection of the secondary electron signal was symmetrical in the SEM chamber, one would expect the plot to mirror vertically around the 0˚ data point. However, the trend continues through zero, illustrating that the detector is at an angle and the positive tilt values seem to work in favour of the spectral acquisition. When comparing the –20˚ and +20˚ datapoint where the relative angle of the primary beam to the surface is the same, it may be said that the orientation of the surface to the detector is significantly more important to the spectral shape than the orientation of the sample surface to the primary beam. This adds further geometric complexity to the system which needs to be taken into account to understand the secondary electron spectra, or at least to obtain reproducible curves.

While the asymmetry of the SE detection in this instrument has been characterised through models and line diagrams recently [19], the magnitude of this effect on experimental data is presented here for the first time. An important implication for achieving a reproducible and consistent images and spectra is the requirement to avoid macroscale roughness on any sample, and to carefully record the beam–sample–detector geometry used as much as possible.

Not all samples (especially not those of interest in this project) may easily be prepared as planar and smooth samples, and so an alternative solution to removing the asymmetry-caused detector shadowing effect is presented in **Figure 5.11**. The silicon cross of a reference sample is imaged, revealing shadows indicated by the orange arrows in **a**. If the sample is free of larger scale topography, the shadows can be moved by 180˚ to the opposite position by rotating the stage, as shown in **b**. The average of both

images shown in **c** is free of the shadowing effect, demonstrating that the detector asymmetry may be corrected to a degree. This is also be applicable to spectral imaging, as done in Chapter 7, although it requires a doubling of acquired images and thus double the dose, unless two spectral datasets at 180˚ to one another are acquired at half the dose and added together, effectively achieving an average as in **Figure 5.11** c.
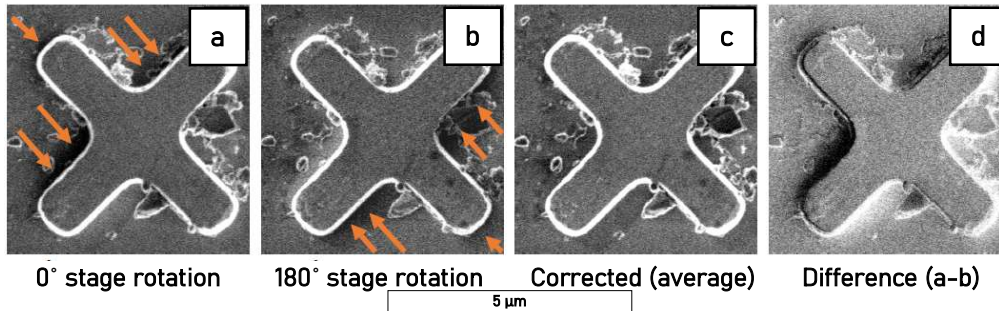

Figure 5.11: Helios SEM micrographs showing detector shadowing (orange arrows) on a 5 x 5 μm Si cross using through-lens detection at a mirror voltage of 10.2 MV (collection of 0–1.47 eV electrons) in the Helios SEM at a) 0˚ stage rotation and b) 180˚ stage rotation—image rotated back 180˚ for direct comparison with a; c) Angular corrected images by taking the average of a and b; d) depiction of the difference (a–b) between a and b isolating the shadowing effect of the detector.

This detector shadowing is a complication for compositional mapping, but may simultaneously be an opportunity for the imaging of 3D structured samples, such as multiscale structural materials: if the influence of angle on the detection efficiency for each SE energy is well characterized, the material and angular contributions could be deconvoluted, as demonstrated simplistically in **Figure 5.11 c** and **d**.

The elimination of angular and topographical effects may be achieved in three ways suggested here: Firstly, if the angular dependencies are well-characterised in all directions they may be corrected, as shown in **Figure 5.11 c**. Secondly, through refined sample-preparation techniques samples could be made as planar as possible to eliminate such effects, as discussed in the following sections. Finally, secondary electron detector designs could be realised, in which angular orientations have less or no effect on the spectral measurement [24].

5.2 Summary of Recommended Workflow

Based on the results presented in this chapter, a recommended spectral acquisition workflow is presented below.

5.2.1 Prepare for imaging

- Home the stage and record relative positions of the stage, sample and detector
- Set working distance and keep it constant for the entire data set

5.2.2 Optimise image parameters

- For uncoated polymer samples, start at $E_0 = 1$ keV or lower and a low beam current with sufficient signal
- Use the maximum scan interlace
- Use the minimum dwell time possible
- Use image integrations to generate sufficient signal to noise
- Use drift correction in conjunction with image integration if available
- Choose maximum magnification which sufficiently resolves structures of interest
- Increment and decrement E_0 until a stable window with good image resolution is found
- Further decrease beam current if possible while maintaining sufficient signal, and adjust number of image integrations to the minimum number while maintaining a good signal to noise ratio

5.2.3 Spectral acquisition

- Scan in the increasing SE energy direction
- Perform initial scan with a larger energy range and identify the SE energy region of interest
- Reduce energy range in subsequent scans
- If required, reduce the energy step without reducing it below the energy resolving power of the energy filter

5.3 References

1. J.H. Butler, D.C. Joy, G.F. Bradley and S.J. Krause: *Low-voltage scanning electron microscopy of polymers*. Polymer (Guildf). **36**, 1781–1790 (1995).
2. J. Pawley: *Low voltage scanning electron microscopy*. J. Microsc. **136**, 45–68 (1984).
3. D.C. Joy and C.S. Joy: *Low voltage scanning electron microscopy*. Micron **27**, 247–263 (1996), doi:10.1016/0968-4328(96)00023-6.
4. D.C. Joy: *Control of charging in low-voltage SEM*. Scanning **11**, 1–4 (1989).
5. H. Seiler: *Secondary electron emission in the scanning electron microscope*. J. Appl. Phys. **54**, R1–R18 (1983), doi:10.1063/1.332840.
6. K.J. Abrams, M. Dapor, N. Stehling, M. Azzolini, S.J. Kyle, J.S. Schäfer, A. Quade, F. Mika, S. Kratky and Z. Pokorna: *Making Sense of Complex Carbon and Metal/Carbon Systems by Secondary Electron Hyperspectral Imaging*. Adv. Sci. 1900719 (2019).
7. G.H. Michler: Electron microscopy of polymers, (Springer Science & Business Media, 2008).
8. J. Cazaux: *Some considerations on the secondary electron emission, δ, from e– irradiated insulators*. J. Appl. Phys. **85**, 1137–1147 (1999).
9. D.C. Joy and C.S. Joy: *Dynamic charging in the low voltage SEM*. Microsc. Microanal. **1**, 109–112 (1995).
10. D.C. Joy and J.B. Pawley: *High-resolution scanning electron microscopy*. Ultramicroscopy **47**, 80–100 (1992), doi:https://doi.org/10.1016/0304-3991(92)90186-N.
11. P.K. Bhattacharya and L. Maynard: *A micron scale Faraday cup for electron beam current measurements*. J. Vac. Sci. Technol. A Vacuum, Surfaces, Film. **9**, 364–368 (1991).
12. P.C. Hoyle, J.R.A. Cleaver and H. Ahmed: *Electron beam induced deposition from W (CO) 6 at 2 to 20 keV and its applications*. J. Vac. Sci. Technol. B Microelectron. Nanom. Struct. Process. Meas. Phenom. **14**, 662–673 (1996).
13. N. Silvis-Cividjian, C.W. Hagen, L.H.A. Leunissen and P. Kruit: *The role of secondary electrons in electron-beam-induced-deposition spatial resolution*. Microelectron. Eng. **61**, 693–699 (2002).
14. C. Li, S.F. Mao and Z.J. Ding: *Time-dependent characteristics of secondary electron emission*. J. Appl. Phys. **125**, 24902 (2019), doi:10.1063/1.5080264.
15. C. Li, S.F. Mao, Y.B. Zou, Y.G. Li, P. Zhang, H.M. Li and Z.J. Ding: *A Monte Carlo modeling on charging effect for structures with arbitrary geometries*. J. Phys. D. Appl. Phys. **51**, 165301 (2018), doi:10.1088/1361-6463/aab2cf.
16. A.H. Zewail: *Four-Dimensional Electron Microscopy*. Science (80-.). **328**, 187 LP – 193 (2010), doi:10.1126/science.1166135.
17. E. Najafi, T.D. Scarborough, J. Tang and A. Zewail: *Four-dimensional imaging of carrier interface dynamics in p-n junctions*. Science (80-.). **347**, 164 LP – 167 (2015), doi:10.1126/science.aaa0217.
18. N. Stehling, R. Masters, Y. Zhou, R. O'Connell, C. Holland, H. Zhang and C. Rodenburg: *New perspectives on nano-engineering by secondary electron spectroscopy in the helium ion and scanning electron microscope*. MRS Commun. **8**, 226–240 (2018), doi:10.1557/mrc.2018.75.
19. I. Konvalina, F. Mika, S. Krátký, E. Materna Mikmeková and I. Müllerová: *In-Lens Band-Pass Filter for Secondary Electrons in Ultrahigh Resolution SEM*. Materials (Basel). **12**, 2307 (2019).
20. V. Kumar, W.L. Schmidt, G. Schileo, R.C. Masters, M. Wong-Stringer, D.C. Sinclair, I.M. Reaney, D. Lidzey and C. Rodenburg: *Nanoscale Mapping of Bromide Segregation on the Cross Sections of Complex Hybrid Perovskite Photovoltaic Films Using Secondary Electron Hyperspectral Imaging in a Scanning Electron Microscope*. ACS Omega **2**, 2126–2133 (2017).
21. N.A. Stehling, K.J. Abrams, C. Holland and C. Rodenburg: *Revealing spider silk's 3D nanostructure through low temperature plasma etching and advanced low-voltage SEM*. Front. Mater. **5**, 84 (2018).
22. Q. Wan, K.J.K.J. Abrams, R.C.R.C. Masters, A.C.S.A. Talari, I.U.I.U. Rehman, F. Claeyssens, C. Holland and C. Rodenburg: *Mapping Nanostructural Variations in Silk by Secondary Electron Hyperspectral Imaging*. Adv. Mater. **29**, 1703510 (2017), doi:10.1002/adma.201703510.
23. R.C. Masters, A.J. Pearson, T.S. Glen, F.-C. Sasam, L. Li, M. Dapor, A.M. Donald, D.G. Lidzey and C. Rodenburg: *Sub-nanometre resolution imaging of polymer-fullerene photovoltaic blends using energy-filtered scanning electron microscopy*. Nat. Commun. **6**, (2015).
24. A. Khursheed: Scanning electron microscope optics and spectrometers, 1st ed., (World Scientific Co Pte, Singapore, 2010).

6 Sample preparation for successful spectral measurements

As established in the previous chapter, a flat surface with minimal stray fields is necessary for consistent spectral imaging of different materials. This poses a significant challenge for natural materials, as they are often rough and structured on many length scales. Additionally, their thermal and chemical sensitivity limits the number of procedures which can be applied to the material without altering it. As SEM is surface sensitive, the observation of cross-sections is necessary for a complete picture of the material, but it is especially challenging as fracturing or sectioning may induce plastic deformation or other sample preparation artefacts. In the following section, procedures are presented which have proven useful for sample preparation for LV-SEM observation of cross-sections, and their advantages and limitation are discussed to guide future projects in overcoming these practical hurdles. Finally, this practical knowledge collected throughout the project is applied on a natural structural material of interest, and the power of modern data analysis techniques in extracting meaningful results is demonstrated.

6.1   Cryo-SEM

In Cryo-SEM the sample preparation and imaging can be performed close to the boiling point of nitrogen gas (-195.8 ℃), which comes at an increased cost and technical requirements for the experiment; however, it eliminates a number of problems which are encountered at room temperature. Firstly, it can be assumed that the materials of interest are investigated in their natural state of hydration—that is, the rapid decrease down to liquid nitrogen temperature captures the water inside the structure where it fulfils its natural function, and it cannot escape into vacuum as easily as at room

temperature. Cryo-SEM has a significant advantage over room-temperature SEM due to the role of water being an ongoing field of investigation for spider silk and the mechanical response of natural structural materials in general [1–5]. Secondly, brittle fractures are much more easily obtained at lower temperatures, where materials are more prone to having a glass-like mechanical response and fail without plastic deformation to yield cleanly fractured cross-sections which reflect the original internal composition and structure of the material. Unfortunately, but rather remarkably, spider silk exhibits plasticity and significant pull-out even at -180 ˚C as evident in **Figure 6.1 a–c**. This is consistent with previously reported observations [6] and more systematic thermal analysis of spider silk which show that spider silk increases in tensile toughness and elongation before break below 0 ˚C and has significant toughness down to liquid nitrogen temperatures [6,7].

Some observations were nonetheless of interest, such as the bell-shaped fracture surfaces (shown in **Figure 6.1 c**) which may indicate increased plastic recovery of the inner core of the fibre compared to the outer core and skin. This is consistent with accounts of a higher order-disrupting proline content in the inner core [8,9], as proline is thought to contribute to the elasticity of the structural protein.

In liquid nitrogen systems going to temperatures significantly lower than -180 ˚C is not an option, so the problem of the plastic fractures of the fibres was approached from a different angle. The observation of the fractures also revealed that there was significant detachment of the fibres from the cryo-glue/graphite matrix (**Figure 6.1 b**), indicating very little surface adhesion. Indeed, the spider silk surface has been observed consistently to be almost perfectly cylindrical and remarkably smooth, as evident in **Figure 6.1 d**. In looking to increase fibre-matrix adhesion the as-spun fibre bundles were exposed to an ex-situ reactive oxygen plasma, whereupon imaging of the surface

morphology confirms that 8 min of treatment results in a significant increase in surface

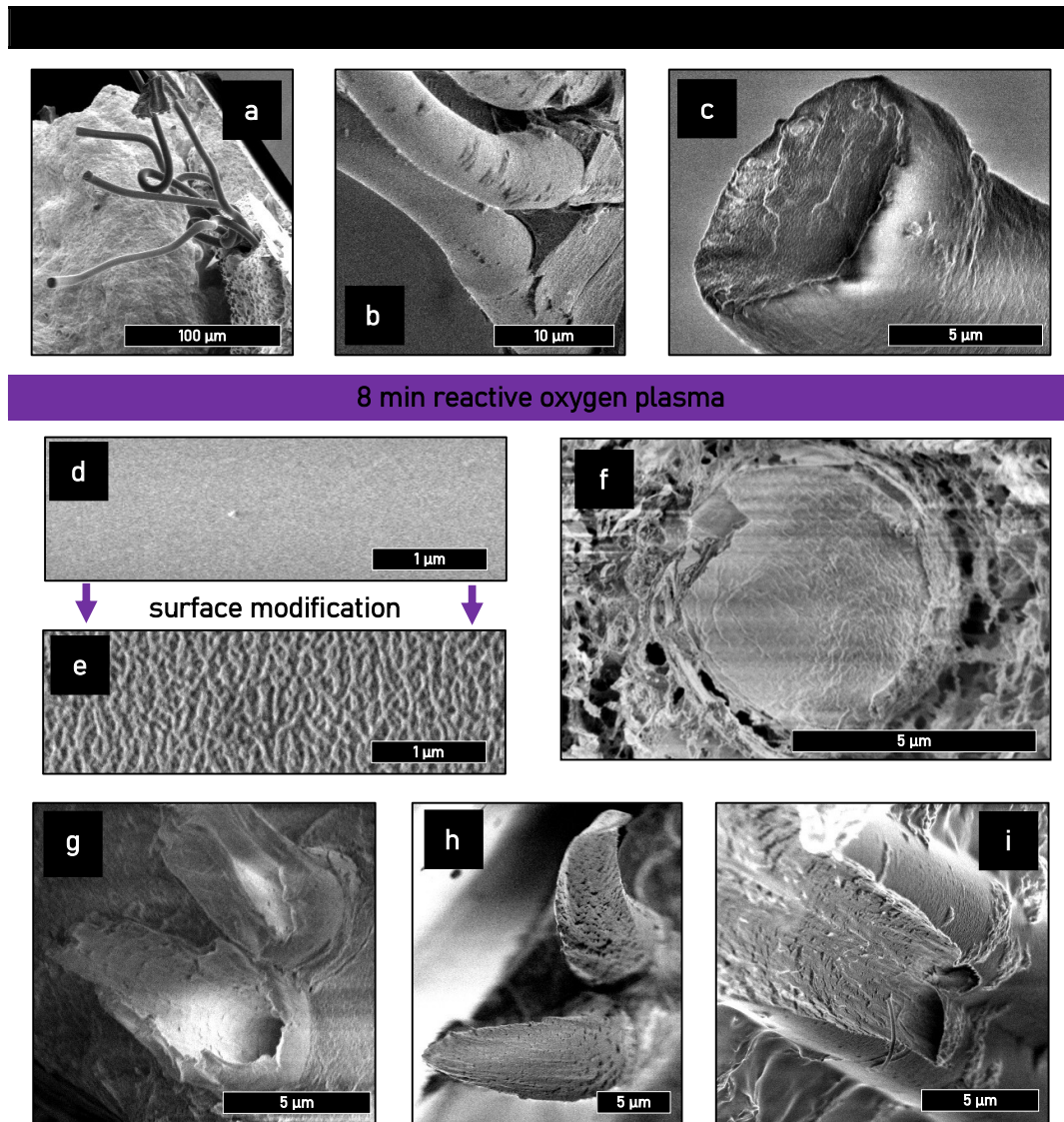roughness due to the formation of nanostructures (see **Figure 6.1 e**).

8 min reactive oxygen plasma

surface modification

Figure 6.1: Cryo–SEM of *Nephila edulis* dragline silk as spun (a–c) and after 8 minutes of non–thermal reactive oxygen plasma treatment (d–i) a) Pull–out of fibre bundle out of matrix b) plastic deformation in the form of necking where the matrix has fractured c) cross–section with bulging evident indicative of a recoil after fracture. d) Smooth surface texture of as–spun *Nephila edulis* dragline silk e) highly nanostructured surface after 8 minutes of non–thermal reactive oxygen plasma f) circular silk cross–section in the fracture plane of the matrix g) skin–core pull out showing the plastic extension of the core in h. i) longitudinal cross–section

The cryofracture procedure using the dedicated cryo–SEM preparation chamber was

repeated using the treated fibres and indeed fracture surfaces were in one plane with

the matrix and without any visible plastic deformation for approximately 50% of fibres in the bundle, as shown in **Figure 6.1 f**. The cross-section shown exhibits significant charging in the form of horizontal banding, however with the imaging and spectral collection optimisation detailed in section 5.1 it should be possible to control charging to a degree where image quality is high and spectra are free of charging effects.

Besides the desirable cross-sections obtained in plane with the fractured matrix, a number of other fracture morphologies were observed (Figure 6.1 g–i). Evidently the plasma treatment has increased matrix-fibre adhesion so dramatically that some fibre cores were pulled out of their own skin (see g and h). Furthermore, longitudinal sections were obtained serendipitously in a few cases (Figure 6.1 i), revealing nanoscale angular structures which may be related to the presence of β-sheet nanocrystals and nanofibrils within the fibre [10]. These results may serve as inspiration for experimental set-ups which aim to produce axial or longitudinal cryo-fractures—perhaps in a more controlled manner by ensuring excellent matrix adhesion and guiding the crack propagation along a certain orientation.

Since these results were obtained the ex-situ non-thermal reactive oxygen plasma treatment has been further optimised. The results of diameter measurements after plasma exposure show that the plasma etches approximately 100 nm min^{-1} off the diameter of the silk fibre [11], suggesting that the 8 minutes used for the results shown in **Figure 6.1 f–i** is a longer than required for the formation of nanostructures on the surface. Furthermore, shorter durations, such as 1 or 2 minutes, will preserve more of the outer layers of the spider silk for observation in cryo-SEM, while having the same favourable effect of surface roughening for cryo-fracture.

6.2   Room temperature imaging

Room temperature observations have the advantage of being simpler, less costly and more available to the scientific community as cryo-techniques require specialist equipment and training. However, the plasticity of materials needs to be taken into account in room-temperature sample preparation. This is especially crucial for spider silk, as slight deformations change the internal structure of the fibre [12]. For the room-temperature observation of spider silk cross-sections, the goal was to prepare a sample which

a)   was kept well below its glass transition temperature of about 160 ℃ [3]

b)   had been kept under the tension it was collected at the entire time

c)   was not exposed to solvents, water or high humidity due to supercontraction [13]

d)   produced clean cross-sections which in the ideal case would be in a plane with the conductive fracture matrix.

In light of these requirements a common approach is to embed the material within a matrix. For spider silk this has previously been done by using wax [14] or resins [8,15]. However, both approaches raise concerns which have not been sufficiently addressed in the respective application: it needs to be clear whether the wax temperature was above or below the decomposition temperature and how it may have affected the fibre. With the epoxy, or any resin embedding, temperature is also an issue, as the liquid components solidify in an exothermic reaction generating unspecified amounts of heat. The extent of chemical reactions between the uncured liquid epoxy components and the silk fibre are also unknown.

In this project, Field's metal was investigated for its use as an embedding matrix. Field's metal is a eutectic alloy of indium tin and bismuth with a melting point of 62 ℃ [16]. The preparation as specified in the methods Chapter 3 exposes the silk to a defined

maximum temperature of 70 °C to satisfy requirement a) in the list above. The encased

Nephila edulis dragline silk bundles remained tensioned in line with requirement b) and

the stream of Ar gas made sure the silk was not exposed to condensation after

cryofracture while it was left to reach room temperature to satisfy requirement c). The

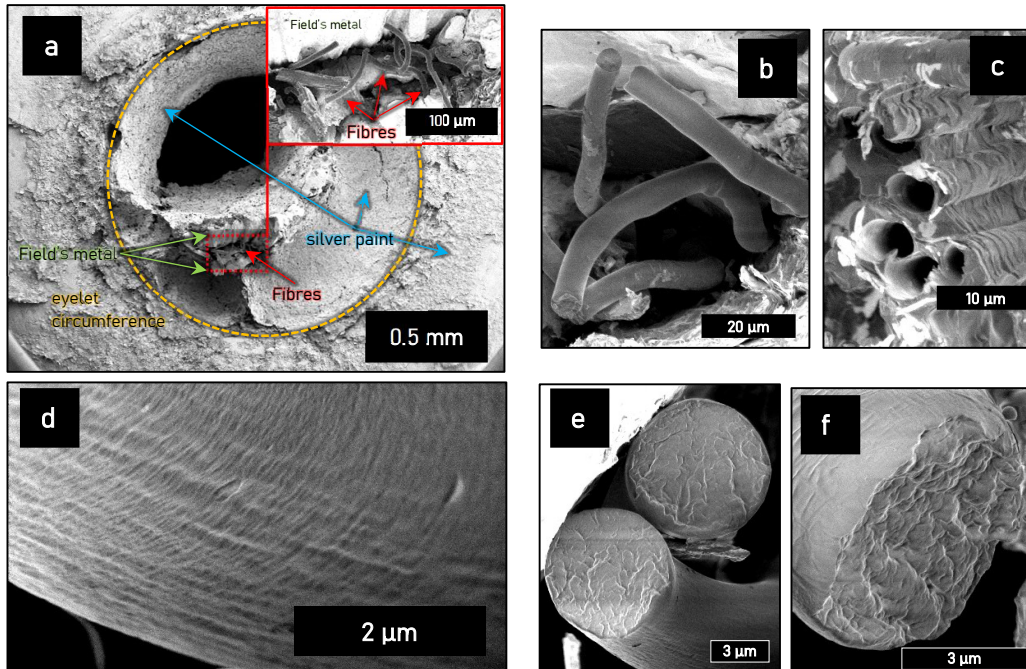resulting fracture is shown in Figure 6.2.

Figure 6.2: a) Overview of *Nephila edulis* spider silk eyelet fracture surface with inset showing fibres b) fibre pull-out with plastic deformation and c) Field's metal cases showing good coverage of fibres but poor adhesion d) Detail of spider silk skin showing intact skin structure e) Fibre cross-sections approximately normal to the electron beam f) fibre cross-section at an angle.

Figure 6.2 illustrates the fracture behaviour of spider silk embedded in Field's metal. It

is clear from **Figure 6.2 a** that the silver adhesive paint did not completely fill the eyelet,

however it did encase the spider silk and Field's metal, resulting in fracture occurring

approximately in plane with the rim of the eyelet. The inset and **Figure 6.2 b** show that

the fibres in the bundle readily pull out of the Field's metal matrix with subsequent

plastic deformation, although **Figure 6.2 c** suggests that the metal coating was

successful in creating a homogenous layer around the fibre for at least some fibres,

despite the poor adhesion between the metal and the skin of the silk. The detail of the

spider silk skin shown in **Figure 6.2 d** demonstrates that the nanostructure of the skin remains intact after exposure to the molten Field's metal at 70 ℃, encouragingly indicating that the metal coating step maintains the fibre properties. Despite the relatively high fraction of pulled-out and deformed fibres and cross-sections, some cross sections remained circular as shown in **Figure 6.2 e**, indicating that the structure remains intact at least in the axial direction of the fibre. However, a normal beam incidence cannot be guaranteed—although it was shown to be important for reproducible spectra—due to the fracture of the fibres away from the metal fracture plane (see **Figure 6.2 f**).

Despite the low success rate of obtaining circular cross-sections at normal beam incidence the samples produced very stable images and high-quality spectra, as is evident from the fact that the results presented in Chapter 5 were obtained using this sample preparation procedure. While this method requires further refinement, it is encouraging that the Field's metal homogenously encases the silk without causing any visible alteration to its structure despite the need for temperatures up to 70 ℃ during the preparation step. As performed with the cryo-SEM sample preparation detailed above, surface roughening of the silk using reactive oxygen plasma treatment may be of use in obtaining fracture of the silk in plane with the metal. The silver adhesive paint is not efficient in filling the eyelet, which leads to undesirable macroscale topography and does not achieve a planar fracture throughout, but the metal case around the silk enables the use of other materials which may otherwise chemically alter the silk, such as resins or glues.

6.3   Chemical and spectral imaging of peacock feather

Taking all the lessons learnt throughout the project into account, an iridescent peacock feather section was embedded in a conductive low melting point thermoplastic and

sectioned using a bench microtome. It was subsequently investigated using secondary electron hyperspectral imaging in conjunction with multivariate analysis. A feather was chosen in favour of spider silk as it has a higher modulus [17], and is expected to maintain its internal structure during microtome sectioning to produce a planar surface. This particular sample is a section of an iridescent peacock (*Pavo cristatus*) feather, where the melanin-rich cells (melanosomes) are arranged along the outside of the feather's barbules in a close-packed fashion to result in structural colour which we perceive as a shimmering iridescence (**Figure 6.3**) [18–20]. For this project it was of interest to see whether secondary electron hyperspectral imaging could detect chemical differences between the melanin-rich edge of the feather barbule and the keratin-rich inside.
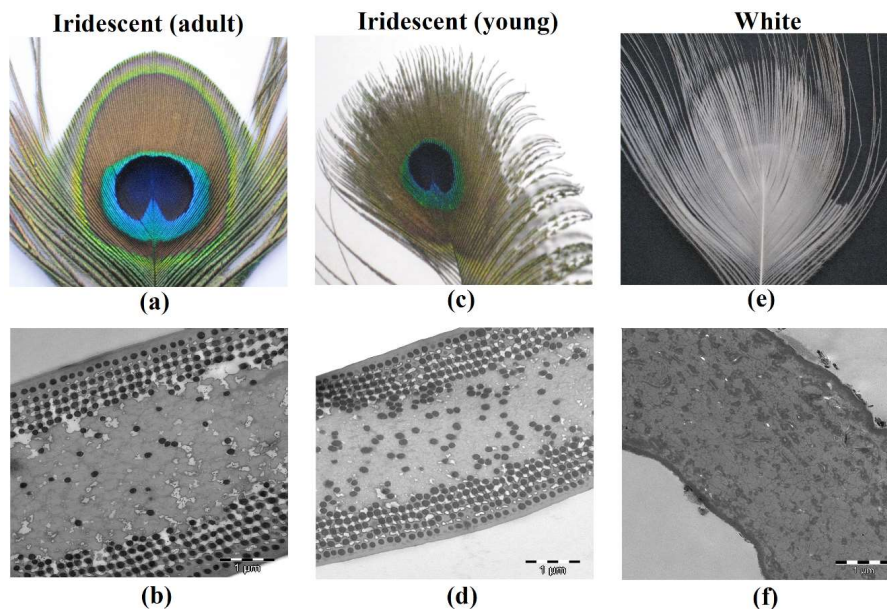
Figure 6.3: *Pavo cristatus* decorative tail feathers and the appearance of their respective barbule cross-sections in TEM, showing the melanin rods concentrated at the edge. Reproduced from [18] under an open access licence, copyright 2015 Optical Society of America.

To access surface properties, the issue of surface contamination must be addressed, as shown on the example of HOPG in Chapter 5, where the evolution of spectra of HOPG

with beam exposure was linked to the degree of contamination present. In the case of HOPG, a fresh sample surface was produced by exfoliation immediately before imaging, but in the case of the feather sectioning procedure it is initially unclear if the 'fresh' previously unexposed surface indeed reflects the real surface chemistry [21], or if adsorption processes have already taken place and surface layers persist even in the vacuum, as SEM chambers are not commonly kept at ultra-high vacuum like Auger spectrometers. However, manufacturers have responded to the problem of surface contamination and hydrocarbon adsorption in the chamber by supplying in-situ plasma systems, which are specialised in removing surface hydrocarbon contamination. These systems are often designed with less beam- and chemically sensitive materials in mind, such as inorganic materials and metals. To characterise whether the plasma treatment has the desirable effect of removing contamination layers, and to confirm that it has not had detrimental effects such as damaging the sample, spectra were recorded on the sectioned iridescent peacock feather surface before and after 3 minutes of in-situ plasma cleaning.

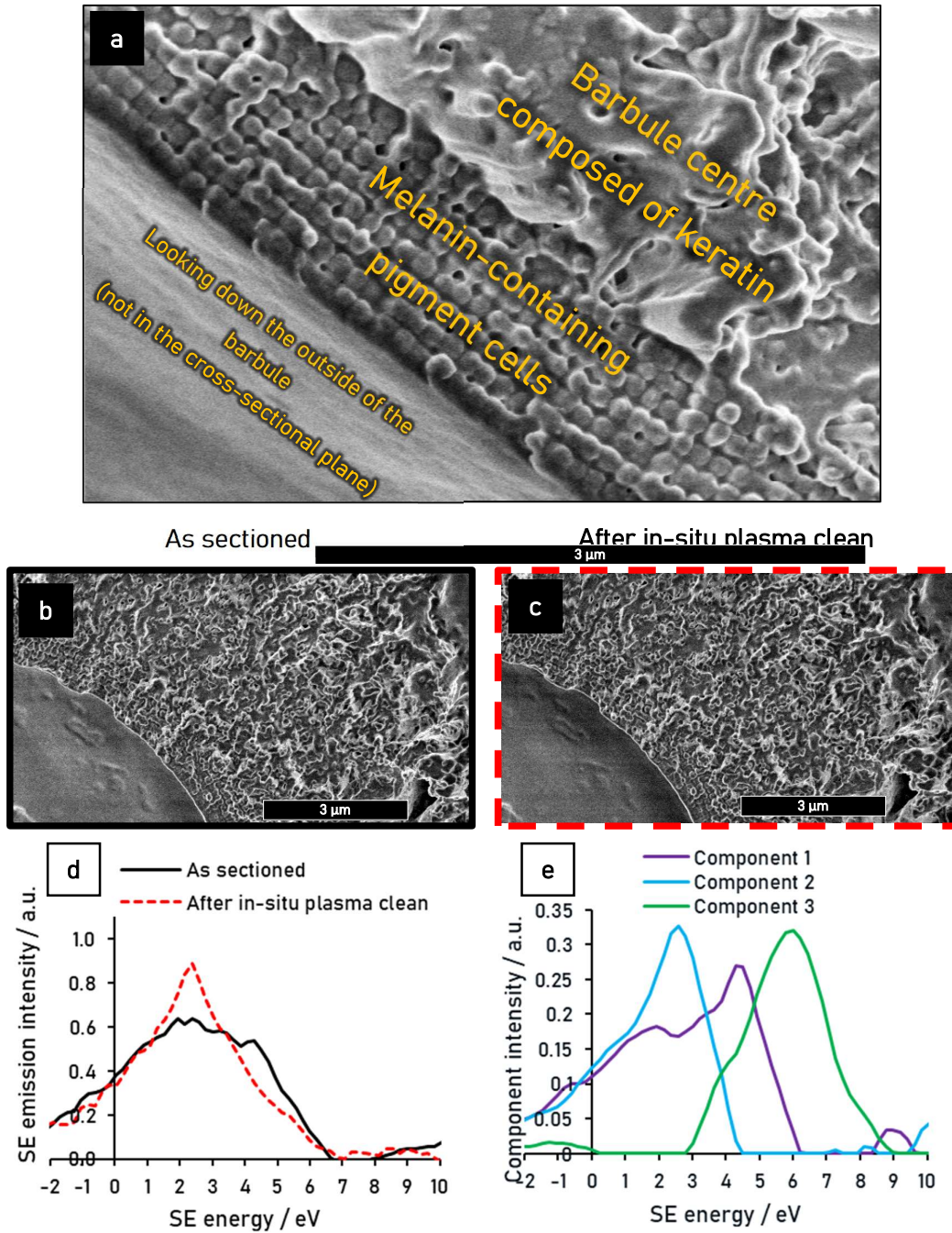**Figure 6.4:** b) Overview of an iridescent sectioned peacock (*Pavo cristatus*) feather barbule b and c) Secondary electron images and d) spectra of sectioned iridescent peacock feather before (solid black line) and after in-situ plasma cleaning (dashed red line). The full rectangular field of view shown was used for the measurement of the spectra e) 3-component result of a non-negative matrix factorisation performed on both stacks.

The comparison of **Figure 6.4 b** and **c** reveals very little difference in the regular secondary electron image, which would suggest that the plasma has not damaged the surface on scales above the nanoscale. Despite the similarity of the images, the spectra shown in **d** reveal significant changes in the spectrum before (solid black line) and after the plasma treatment (dashed red line), highlighting the increase in sensitivity to compositional changes which can be achieved through differentiating secondary electron energies. The intensities of the peaks at 2.2 and 4.5 eV reverse through the plasma treatment, resulting in a higher intensity of the 2.2 eV peak and an overall sharper peak after plasma treatment.

The two stacks were input into a NMF multivariate analysis in an attempt at characterising the spectral components which the plasma treatment removes or produces. The three component solution of the multivariate analysis is shown in **Figure 6.4 e**, with components 2 and 3 representing near-gaussian curves at lower and higher energy respectively. Component 1 has a very characteristic two peak shape, with a lower energy peak at 2 eV and a higher energy peak at 4.5 eV. Component 1 is in excellent agreement with spectra recorded from carbon contamination as the part of previous work performed in the group [21], and thus component 1 can be assigned reliably as characterising the spectrum of carbon contamination. This serves as confirmation that carbon contamination is an issue to keep in mind when imaging these uncoated sections. To study the effect of the plasma treatment on the carbon contamination (component 1) the local loadings of each component were mapped throughout the image as shown in **Figure 6.5**. For each image, a higher local brightness corresponds to a higher local component loading and thus a bigger contribution of the respective component.
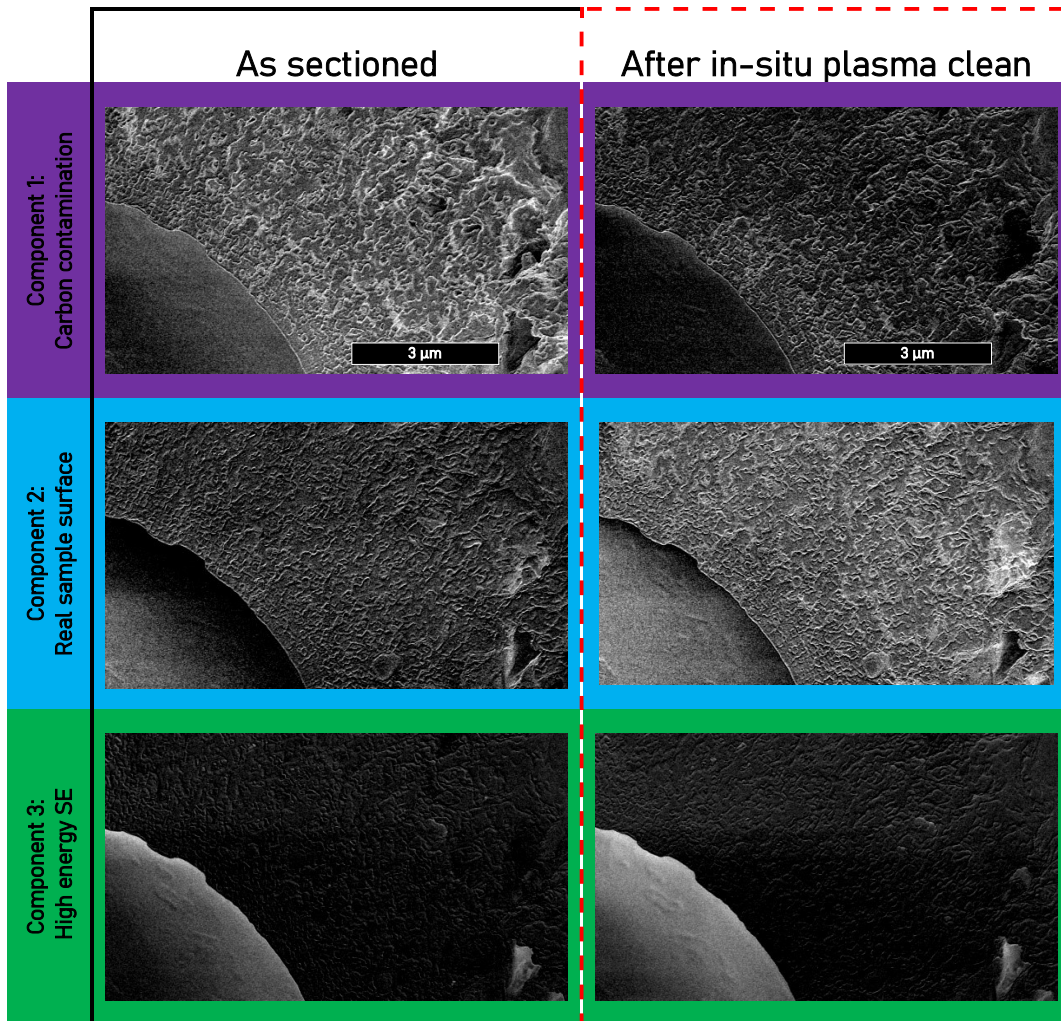
Figure 6.5: Component loadings throughout the field of view for the as sectioned and plasma cleaned feather section.

Component 1 has been assigned to carbon contamination, and thus the component 1 loadings (purple) shown in **Figure 6.5** confirm that the plasma treatment removes significant amounts of carbon contamination, evidenced by the reduced brightness of component 1 after the in-situ chamber plasma clean. Component 2 (blue) can be tentatively assigned as the clean sample surface, which gains intensity after the plasma cleaning procedure where less of the surface will be masked by the contamination layer. The local loadings allow the assignment of component 3 (green) as high-energy and background electrons, which mostly do not arise from the feather as a region of

interest and thus the absence of any obvious change after the plasma treatment is in line with expectations.

The results of the multivariate analysis have shown that the in-chamber plasma treatment is effective in removing carbon contamination and exposing the real sample surface, which is the subject of interest for this sample. In the next step, the regional spectra of the melanin and keratin-rich regions were used to generate hyperspectral images highlighting each composition (**Figure 6.6**).
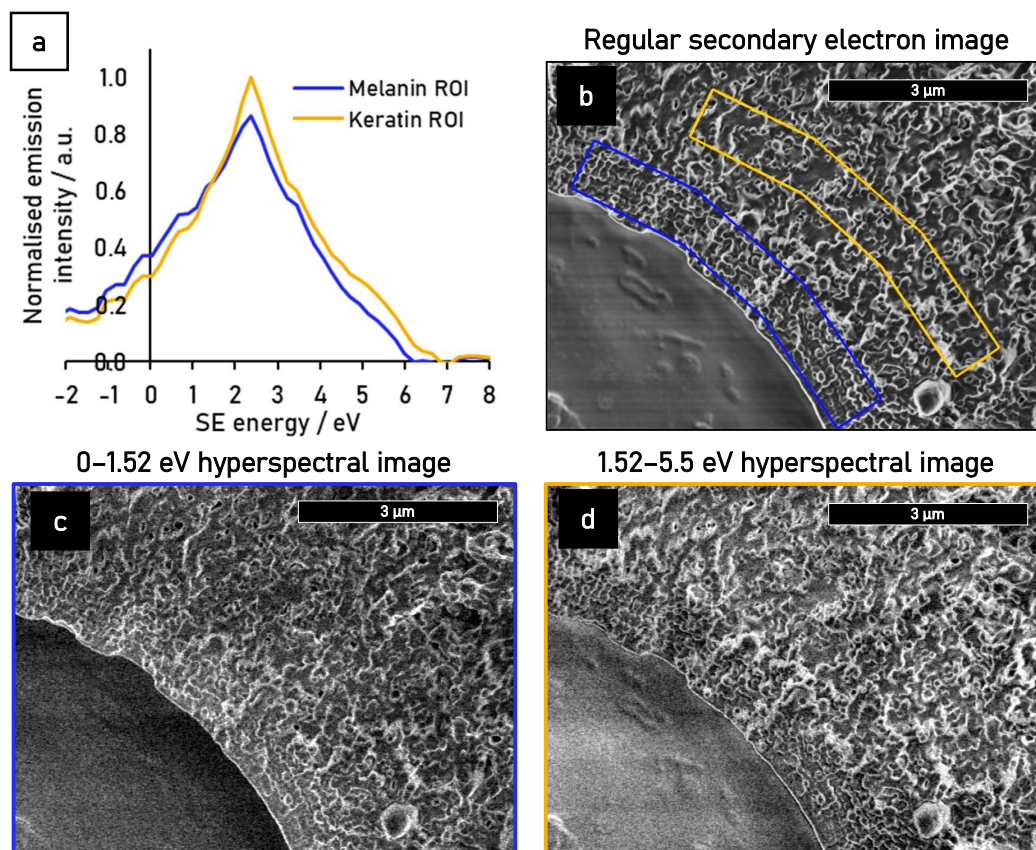
Figure 6.6: Plasma cleaned iridescent peacock feather spectra and hyperspectral images: a) spectra recorded from the melanin rich region (blue) and keratin feather matrix (yellow) b) regular secondary electron image indicating the respective regions of interest c) Hyperspectral image in the energy range of 0–1.52 eV to highlight the melanin-rich regions d) Hyperspectral image in the range of 1.52–5.5 eV to highlight the feather keratin matrix

The fact that the spectral data set has one energy and two spatial dimensions means that a spectrum may be extracted for each pixel. In practice larger areas have to be spatially averaged to result a spectrum with a larger signal to noise ratio, but these areas may still be very specific to the sample composition of interest. **Figure 6.6 a** contrasts the spectrum of the melanin-rich region (blue) at the edge of the section, where the melanosomes are arranged, to the keratin-rich matrix further into the centre of the structure (yellow). The respective regions of interest which were used to produce each spectrum are indicated in **Figure 6.6 b**. The spectra of each were used to formulate energy windows, in which one composition would be expected to be more prominent than the other: The spectral intensity of the melanin-rich region is higher in the energy window of 0–1.52 eV, where the two curves cross and subsequently the keratin-rich spectrum exhibits the higher intensities (1.52–5.5 eV). Hyperspectral images were generated which include only electrons of the purposefully chosen energy windows and indeed the melanin and keratin-rich regions can be mapped throughout the field of view: In **Figure 6.6 c** the melanosomes exhibit a higher brightness than the rest of the section, whereas there is a contrast reversal in the hyperspectral image shown in **Figure 6.6 d**.

This study demonstrates that if imaging parameters, sample preparation considerations and contamination are treated with care and according to the guidelines laid out in this chapter, it is possible to map subtle compositional differences in beam-sensitive and natural structural materials. To the authors knowledge, the chemical differentiation of organic molecules such as melanin and keratin using an electron beam without the need for stains and at nanoscale resolution is a novel result and illustrates the power of the information which lies within the secondary electron signal.

6.4   References

1.   J. Guan, Y.Y. Wang, B. Mortimer, C. Holland, Z. Shao, D. Porter and F. Vollrath: *Glass transitions in native silk fibres studied by dynamic mechanical thermal analysis*. Soft Matter **12**, 5926–5936 (2016), doi:10.1039/C6SM00019C.

2.   G.R. Plaza, G. V Guinea, J. Pérez-Rigueiro and M. Elices: *Thermo-hygro-mechanical behavior of spider dragline silk: Glassy and rubbery states*. J. Polym. Sci. Part B Polym. Phys. **44**, 994–999 (2006), doi:10.1002/polb.20751.

3.   K.B. Guess and C. Viney: *Thermal analysis of major ampullate (drag line) spider silk: the effect of spinning rate on tensile modulus1Presented at TAC 97, Oxford, UK, 14–15 April 1997.1*. Thermochim. Acta **315**, 61–66 (1998), doi:https://doi.org/10.1016/S0040-6031(98)00277-9.

4.   A. Schäfer, T. Vehoff, A. Glišović and T. Salditt: *Spider silk softening by water uptake: an AFM study*. Eur. Biophys. J. **37**, 197–204 (2008).

5.   L.W. Jelinski, A. Blye, O. Liivak, C. Michal, G. LaVerde, A. Seidel, N. Shah and Z. Yang: *Orientation, structure, wet-spinning, and molecular basis for supercontraction of spider dragline silk*. Int. J. Biol. Macromol. **24**, 197–201 (1999), doi:https://doi.org/10.1016/S0141-8130(98)00085-3.

6.   Y. Yang, X. Chen, Z. Shao, P. Zhou, D. Porter, D.P. Knight and F. Vollrath: *Toughness of spider silk at high and low temperatures*. Adv. Mater. **17**, 84–88 (2005).

7.   E.M. Pogozelski, W.L. Becker, B.D. See and C.M. Kieffer: *Mechanical testing of spider silk at cryogenic temperatures*. Int. J. Biol. Macromol. **48**, 27–31 (2011).

8.   A. Sponner, W. Vater, S. Monajembashi, E. Unger, F. Grosse and K. Weisshart: *Composition and hierarchical organisation of a spider silk*. PLoS One **2**, e998 (2007).

9.   D.P. Knight, M.M. Knight and F. Vollrath: *Beta transition and stress-induced phase separation in the spinning of spider dragline silk*. Int. J. Biol. Macromol. **27**, 205–210 (2000).

10.   Q. Wang and H.C. Schniepp: *Nanofibrils as Building Blocks of Silk Fibers: Critical Review of the Experimental Evidence*. Jom (2019), doi:10.1007/s11837-019-03340-y.

11.   N.A. Stehling, K.J. Abrams, C. Holland and C. Rodenburg: *Revealing spider silk's 3D nanostructure through low temperature plasma etching and advanced low-voltage SEM*. Front. Mater. **5**, 84 (2018).

12.   I. Su and M.J. Buehler: *Nanomechanics of silk: the fundamentals of a strong, tough and versatile material*. Nanotechnology **27**, 302001 (2016).

13.   Z. Shao, R.J. Young and F. Vollrath: *The effect of solvents on spider silk studied by mechanical testing and single-fibre Raman spectroscopy*. Int. J. Biol. Macromol. **24**, 295–300 (1999).

14.   C.P. Brown, J. MacLeod, H. Amenitsch, F. Cacho-Nerin, H.S. Gill, A.J. Price, E. Traversa, S. Licoccia and F. Rosei: *The critical role of water in spider silk and its consequence for protein mechanics*. Nanoscale **3**, 3805–3811 (2011).

15.   S.F. Li, A.J. McGhie and S.L. Tang: *New internal structure of spider dragline silk revealed by atomic force microscopy*. Biophys. J. **66**, 1209–1212 (1994), doi:http://dx.doi.org/10.1016/S0006-3495(94)80903-8.

16.   S.Q. Field: Gonzo gizmos: Projects & devices to channel your inner geek, (Chicago Review Press, 2002).

17.   I.M. Weiss and H.O.K. Kirchner: *The peacock's train (Pavo cristatus and Pavo cristatus mut. alba) I. structure, mechanics, and chemistry of the tail feather coverts*. J. Exp. Zool. Part A Ecol. Genet. Physiol. **313**, 690–703 (2010).

18.   J.M. Medina, J.A. Díaz and P. Vukusic: *Classification of peacock feather reflectance using principal component analysis similarity factors from multispectral imaging data*. Opt. Express **23**, 10198–10212 (2015), doi:10.1364/OE.23.010198.

19.   J. Zi, X. Yu, Y. Li, X. Hu, C. Xu, X. Wang, X. Liu and R. Fu: *Coloration strategies in peacock feathers*. Proc. Natl. Acad. Sci. **100**, 12576 LP – 12578 (2003), doi:10.1073/pnas.2133313100.

20.   S. Yoshioka and S. Kinoshita: *Effect of macroscopic structure in iridescent color of the peacock feathers*. FORMA-TOKYO- **17**, 169–181 (2002).

21.   K.J. Abrams, M. Dapor, N. Stehling, M. Azzolini, S.J. Kyle, J.S. Schäfer, A. Quade, F. Mika,
        S. Kratky and Z. Pokorna: *Making Sense of Complex Carbon and Metal/Carbon Systems
        by Secondary Electron Hyperspectral Imaging*. Adv. Sci. 1900719 (2019).

7 Revealing spider silk's 3D nanostructure through low temperature plasma etching and advanced low-voltage SEM

Nicola Stehling[1], Kerry J. Abrams[1], Chris Holland[1], Cornelia Rodenburg[1]*

[1]University of Sheffield, Department of Materials Science and Engineering, Sheffield S1 3JD, United Kingdom

* Correspondence:
Cornelia Rodenburg
C.Rodenburg@sheffield.ac.uk

7.1 Contributions

I performed the majority of the experimental work and data analysis and wrote the first draft of the manuscript. KA performed SEM instrument calibration and validation work central to the spectral data in the manuscript. CH and CR contributed to the experimental design, project supervision, and the writing of the manuscript.

Please see overleaf for the paper.

ORIGINAL RESEARCH

Check for updates

Revealing Spider Silk's 3D Nanostructure Through Low Temperature Plasma Etching and Advanced Low-Voltage SEM

Nicola Stehling, Kerry J. Abrams, Chris Holland and Cornelia Rodenburg*

Department of Materials Science and Engineering, University of Sheffield, Sheffield, United Kingdom

The excellent mechanical properties of spider dragline silk are closely linked to its multiscale hierarchical structuring which develops as it is spun. If this is to be understood and mimicked, multiscale models must emerge which effectively bridge the length scales. This study aims to contribute to this goal by exposing structures within *Nephila* dragline silk using low-temperature plasma etching and advanced Low Voltage Scanning Electron Microscopy (LV-SEM). It is shown that Secondary Electron Hyperspectral Imaging (SEHI) is sensitive to compositional differences on both the micro and nano scale. On larger scales it can distinguish the lipids outermost layer from the protein core, while at smaller scales SEHI is effective in better resolving nanostructures present in the matrix. Key results suggest that the silks spun at lower reeling speeds tend to have a greater proportion of smaller nanostructures in closer proximity to one-another in the fiber, which we associate with the fiber's higher toughness but lower stiffness. The bimodal size distribution of ordered domains, their radial distribution, nanoscale spacings, and crucially their interactions may be key in bridging the length scale gaps which remain in current spider silk structure-property models. Ultimately this will allow successful biomimetic implementation of new models.

Keywords: spider silk, biopolymer, protein, hierarchical structure, multiscale material, natural materials, low voltage scanning electron microscopy

INTRODUCTION

Spider silk is of great interest to a range of scientific communities due to its high-performance and unique mechanical properties (Vollrath and Porter, 2009; Walker et al., 2015; Koeppel and Holland, 2017; Holland et al., 2018b). These properties are attributed to a hierarchical arrangement of ordered and disordered protein structures within a single fiber (Vollrath and Porter, 2009; Vollrath et al., 2011; Porter et al., 2013). This nanostructure has been extensively explored by bulk and space-averaging techniques such as calorimetry (Cebe et al., 2013; Vollrath et al., 2014; Holland et al., 2018a), spectroscopy (Dicko et al., 2007; Boulet-Audet et al., 2015) small angle scattering X-ray and neutron diffraction (Termonia, 1994; Riekel et al., 2000; Greving et al., 2010; Wagner et al., 2017) and solid state nuclear magnetic resonance (NMR) (Willis et al., 1972; Hijirida et al., 1996; Kümmerlen et al., 1996; Yang et al., 2000; Holland et al., 2008; McGill et al., 2018), which together have provided the fuel for a range of modeling approaches (Giesa et al., 2011; Cranford, 2013; Ebrahimi et al., 2015; Rim et al., 2017). In comparison, spatially resolved techniques are yet to be fully explored, but have already hinted at a diverse set of rich nano- and microscale features

such as micelles (Lin et al., 2017; Oktaviani et al., 2018; Parent et al., 2018), nanofibrils (Wang and Schniepp, 2018), elongated cavities (Frische et al., 2002), and an overall radial variation of composition and structure (Li et al., 1994; Knight et al., 2000; Frische et al., 2002; Sponner et al., 2007; Brown et al., 2011). Therefore, in order to uncover the secret of spider silk's mechanical response, the precise spatial distribution of structural elements inside the fiber needs to be better understood.

Investigations of the radial distribution of structures within spider dragline silk show that the composition of the shell, comprising of the lipid, and glycoprotein coating and protein skin, is substantially different compared to that of the core. In a typical dragline fiber of 5 µm diameter, the coating is approximately 100 nm in thickness and can be further differentiated into a waxy lipids and a glycoprotein layer, which together are attributed with the control of moisture content, antimicrobial properties, and pheromonal communication (Augsten et al., 2000; Sponner et al., 2005, 2007). Although it is chemically diverse, the contribution of the coating to the fiber's overall tensile behavior has been proposed to be very small (Yazawa et al., 2018). The underlying skin is of similar thickness to the coating and has been found to compose mostly of minor ampullate spidroin protein (MiSp) which is the main component of minor ampullate fibers (Sponner et al., 2007).

Remarkably, there is a further differentiation of structure within the radial profile of the spider silk's core: below the thin (∼100 nm) proteinous skin lies the β-sheet rich outer-core and finally the proline-rich and more structurally disordered inner core (Li et al., 1994; Knight et al., 2000; Vollrath and Knight, 2001; Sponner et al., 2007). The greatest contribution to the mechanical properties of the fiber arise from these core layers as they make up the bulk of the fiber's volume. The core contains the ordered β-sheet structures but also the disordered amorphous phases. The β-sheet structures have been of intense interest to structural analysis (McGill et al., 2018) and mechanical modeling (Keten et al., 2010; Giesa et al., 2011) whereas the disordered amorphous components have attracted less scientific attention, in part due to the difficulty of structurally characterizing them.

Currently, mechanical models do not consider this radial structure present in the most extensively studied *Nephila* dragline silk, which is at odds with the widespread agreement that multi-scale organization is integral to the fiber's characteristic tensile response (Nova et al., 2010; Giesa et al., 2011; Skelton and Nagase, 2012; López Barreiro et al., 2018; Yarger et al., 2018). A better dataset concerning the 3D mechanical properties and spatial distribution of different structural units within the silk will allow for better multi-scale mechanical models and will be important in successfully designing spider-silk mimicking fibers and polymers with tailored properties (Koeppel and Holland, 2017).

In this study a controlled variation of reeling speed is utilized to produce silk of varying mechanical and structural properties. To elucidate the differences in structure, the fibers are analyzed unstained and uncoated in the secondary electron microscope (SEM) by Secondary Electron Hyperspectral Imaging (Wan et al., 2017) and structures are revealed by low temperature plasma etching. The ultimate goal is to spatially characterize the 3D distribution of nanostructure radially and longitudinally and

presenting results which will aid in the parameterization of multi-scale mechanical models.

MATERIALS AND METHODS
Collection of Single Fiber Dragline Silk
All spider silk samples used in the Secondary Electron Hyperspectral Imaging (SEHI) and the mechanical testing stem from one continuous thread of a single mature *Nephila inaurata* female. The spider was kept in a lab environment and was fed crickets and waxworms *ad libidum*. To obtain single fiber major ampullate dragline silk, the spider was anesthetized using carbon dioxide and subsequently immobilized on a polystyrene block with its underside facing upward. The spider was left to regain consciousness for 30 min to eliminate any effect of the carbon dioxide on the spinning process (Riekel et al., 2004). Under an optical stereo microscope (Leica MZ6), a single major ampullate dragline thread was separated from other silks and taken up onto the reeling device. The reeling device was designed in-house to allow simultaneous control over rotational and lateral translational speeds of the reel, allowing the collection of single fibers with approximately 1 cm lateral spacing at well-defined speeds of 5, 20, and 40 mm s^{-1} and facilitating further sample preparation.

Mechanical Testing
While ensuring that the tension of the fibers was maintained, the *N. inaurata* fibers were applied to stiff paper frames as is common protocol for tensile testing spider silk (Kitagawa and Kitayama, 1997) and were glued above and below the tensile testing window to ensure good adhesion and a gauge length of 5 mm. 18 tensile samples were prepared for each reeling speed. After the glue was left to set for at least 24 h the paper frames were loaded into a Zwick tensile tester equipped with a 5 N loading cell using crocodile clamps, and the frame was cut using nail clippers to obtain the free-standing fiber. Tensile tests of all samples were performed in a controlled lab environment and within 6 h to minimize variability arising from differences in temperature and humidity. The tests were strain controlled at 10 mm min^{-1} and were simultaneously videoed. A sample video the tensile test is available to watch in the **Supplementary Information**. Mechanical properties were extracted from the tensile curves applying cross-sectional areas derived from diameter measurements of each reeling speed obtained by LV-SEM imaging.

SEM and Image Data Processing
All SEM imaging and measurements were performed on a FEI Helios NanoLab SEM.

Imaging
Images were collected at a working distance of 4.1 mm, and a current of 13 pA. The scan preset was chosen to obtain minimum spatiotemporal electron exposure: the dwell time was set to the minimum 50 ns, a scan interlace of 8 was used and 32 scans were integrated using drift correction to obtain the image. Accelerating

voltages of 500 eV or 1 keV were used and are further specified in the figure caption.

Spectral Acquisition

The FEI Helios NanoLab SEM is equipped with a through-lens detector with a voltage controlled mirror electrode, which deflects the SE signal into the detector. By scanning the voltage on the mirror electrode over a range and generating an image each, the energy range of collected SEs is controlled and spectra and hyperspectral images are obtained through post-processing of the spectral image series. The energy calibration of this process is performed through stage bias experiments, as described elsewhere (Kazemian et al., 2007). For a detailed discussion of the method please refer to (Stehling et al., 2018). When considering the SE signal originating from a cylindrical object such as spider silk, the effect of the SE emission angle must be considered. In all spectra and hyperspectral images presented this effect has been corrected for by taking two spectra, the second of which was taken with a stage rotation of 180° relative to the initial spectrum. For each energy the spectral images were averaged to cancel out angular effects and detector shadowing in post-processing to yield geometrically corrected results. The success of this correction was confirmed by the comparison of the non-corrected to the corrected hyperspectral images of a Si calibration standard sample of known geometry.

Image Processing

Image processing was performed using Fiji software (Schindelin et al., 2012). All images presented have been optimized for their brightness and contrast using histogram normalization.

The Voronoi tessellation was performed by assigning the 8-bit greyscale values 255–141 to the nanostructure in the hyperspectral images of the given energy range. The resulting binary image was subsequently skeletonized to represent the bright nanostructure as a one-pixel line using Zang and Suen's algorithm (Zhang and Suen, 1984) and this was used as input for the Voronoi tessellation. A color look-up-table was applied to better illustrate the distances between particles along the tessellation lines and is displayed adjacent to the tessellation maps.

Low Temperature Plasma Treatment

Plasma treatment was performed in a Diener Electronic Zepto plasma cleaner at 40 kHz, 100 W, and 0.3 mbar air for the specified total times. Samples were exposed to the plasma for no longer than 3 min at a time to exclude the effects of sample heating which have been shown to lead to surface modification of a different kind (Yip et al., 2002). For treatment times of more than 3 min, the sample was treated for 3 min, then left to cool for 5 min before a subsequent treatment was performed to make up the total treatment time.

RESULTS

To gain a complete understanding of the structural mechanical make-up of spider dragline silk, the radial as well as the longitudinal structures present within silk need to be considered.

Generally, analysis techniques used for the characterization of structures on different scales are either space-averaging, such as nuclear magnetic resonance spectroscopy (NMR) and X-ray diffraction (XRD), or surface sensitive, such as atomic force microscopy (AFM) and electron microscopy (EM). This poses a practical challenge if 3D information with high spatial resolution in all dimensions is sought. If differences in nanostructure alignment and distribution, such as those proposed in literature are to be spatially resolved, the internal structure's 3D distribution must be revealed.
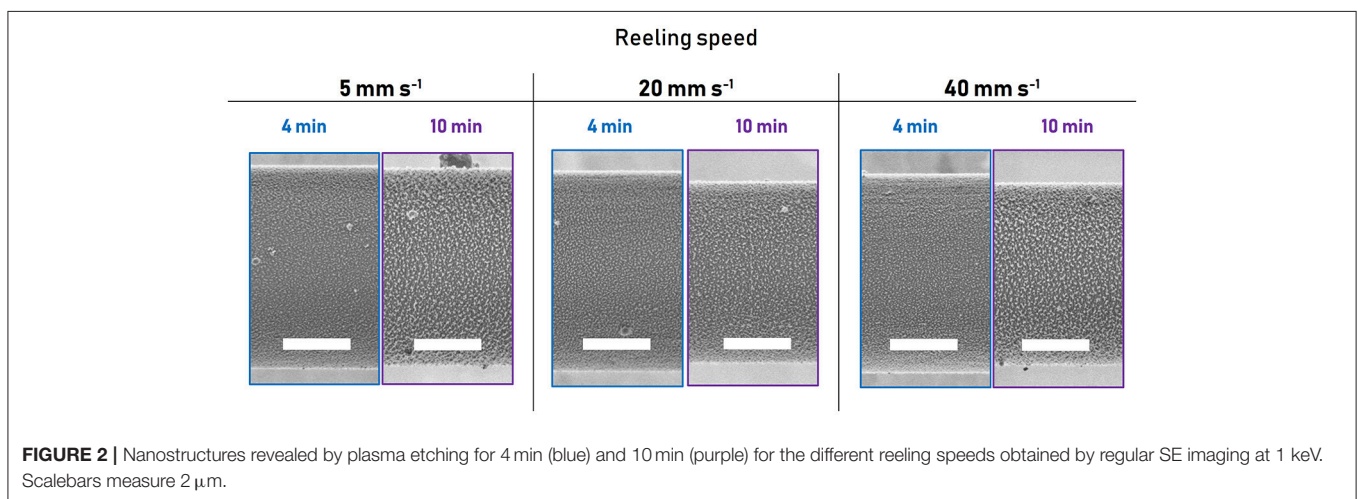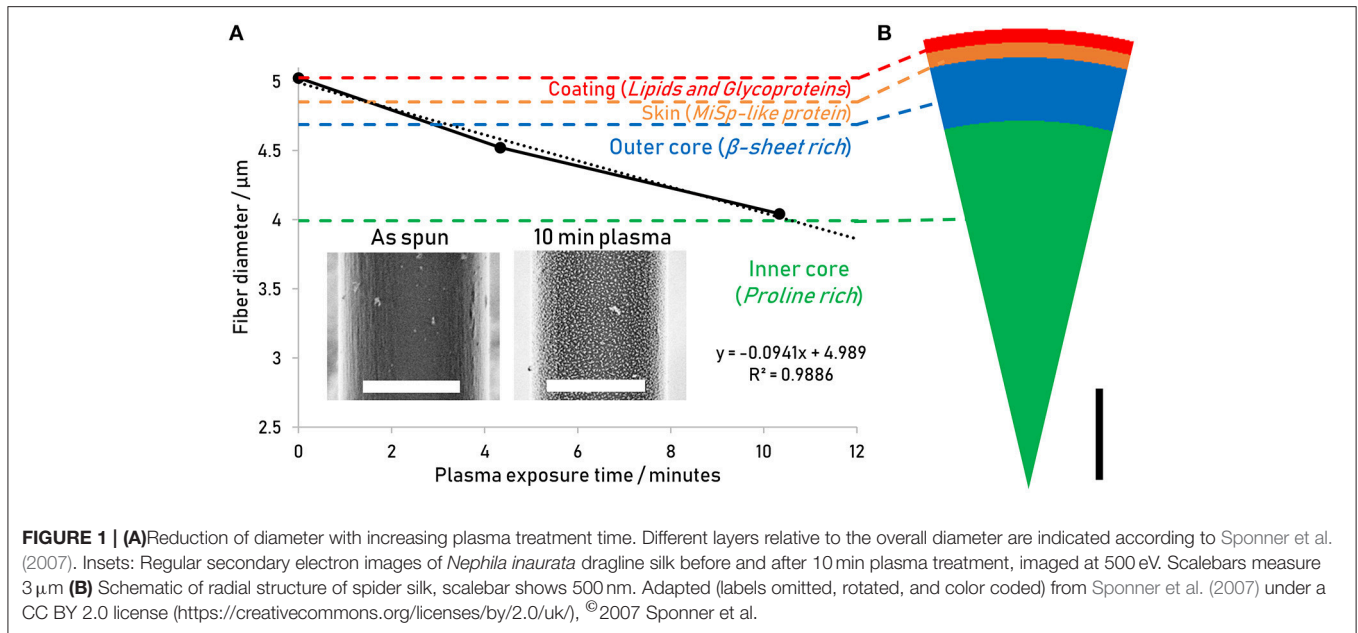
Plasmas are reactive environments in the gas phase and thus modify surfaces in response to the underlying structural composition (Yip et al., 2006). The use of a low temperature plasma for defined periods of time has previously been shown to lead to selective etching of fiber surfaces, with the treated surface morphology being a result of the fiber's crystallinity and its strain history (Wakida and Tokino, 1996; Yip et al., 2002,?, 2006; Stehling et al., 2018). In our experiments, plasma treatment was used to firstly etch away layers of the fiber radially to obtain images showing structure in the fiber axis at a given depth, and secondly to expose any nanostructure which may be influenced by the reeling speed and multi-scale organization of the fiber. Diameter measurements performed in the SEM after plasma treatment confirm that this process etches more material with increased treatment time at a rate of approximately 100 nm min^{-1} (**Figure 1**). Thus, this process opens a pathway to exposing selected radial layers through etching, giving insights into the core of the fiber and the nanostructure within.

After 10 min of plasma treatment, a fiber with an original diameter of 5.02 μm was etched by 0.98 μm (0.49 μm either side) to its outer-core, where β-sheet crystals are thought to characterize the nanostructure and the mechanical response (Knight et al., 2000; Sponner et al., 2007). The nanostructures evident in **Figure 1** inset are most likely a result of the presence of β-sheet rich and ordered nano-domains which etch at a slower rate compared to the disordered amorphous phases. Their appearance is consistent with structures observed in dragline silk by SEM after the shell has been washed away by phosphate buffered saline (Augsten et al., 2000) and are similar to those observed in silkworm silk (Wan et al., 2017).

In order to confirm the effects of the etching process and describe the features revealed, a range of reeling speeds was used to generate different order/disorder ratios (Liu et al., 2005). For each reeling speed, the fibers were treated for 4 and 10 min and the comparison of the resulting nanostructures with reeling speed and plasma treatment are presented in **Figure 2**.

To the naked eye, there is no evident trend in the change in nanostructure with reeling speed. However, there are clear differences across all samples in response to plasma treatment time. Based on predictions from **Figure 1**, the images shown in **Figure 2** for both plasma etching times result in the lipid and glycoprotein coating being etched away to expose the outer core of the fiber—at 4 min the outer core just beneath the skin is exposed, while the 10 min etch predictably exposes the outer core close to the inner core.

The observed differences in nanostructure size may be explained by irregularities in the boundary between the skin

FIGURE 1 | (A) Reduction of diameter with increasing plasma treatment time. Different layers relative to the overall diameter are indicated according to Sponner et al. (2007). Insets: Regular secondary electron images of *Nephila inaurata* dragline silk before and after 10 min plasma treatment, imaged at 500 eV. Scalebars measure 3 μm **(B)** Schematic of radial structure of spider silk, scalebar shows 500 nm. Adapted (labels omitted, rotated, and color coded) from Sponner et al. (2007) under a CC BY 2.0 license (https://creativecommons.org/licenses/by/2.0/uk/), ©2007 Sponner et al.

FIGURE 2 | Nanostructures revealed by plasma etching for 4 min (blue) and 10 min (purple) for the different reeling speeds obtained by regular SE imaging at 1 keV. Scalebars measure 2 μm.

and the outer-core which have previously been observed in AFM and immunostaining studies (Li et al., 1994; Sponner et al., 2005), leading to the 4 min treated surface being more skin-like in composition, whereas the 10 min treated surface is characteristic of the proline devoid and β-sheet crystal rich outer core. The reduced etching rate of the β-sheet crystals may also play a role in the increased size of nanostructure features after 10 min treatment, if after etching through the outer-core more β-sheet-rich ordered domains remain and protrude topographically in the image to appear brighter due to the SEM's edge effect prevalent in regular SE imaging.

The predominance of topographical contrast in regular SE images, specifically the edge effect, can pose a problem to image analysis as it exaggerates the size of the nanostructures and could obscure any contrast arising from material differences between the ordered nanostructures and the surrounding

disordered matrix. Thus, the influence of topography is a significant impairment in any attempt to quantifiably characterize differences between the visible structures when using standard Low Voltage SEM.

To better separate the compositional information from the topographical information present in the untreated and plasma treated fiber surfaces we used Secondary Electron Spectroscopy in conjunction with Secondary Electron Hyperspectral Imaging (SEHI) in the SEM under the same conditions. SEHI makes use of the fact that the secondary electron signal from which SEM images are commonly generated incorporates energy information as well as spatial information. It has previously been shown that depending on the SE energy window selected, topography can be excluded and energy ranges can be assigned to different compositions or phases with sensitivity to elemental composition, hybridization state, degree of order and crystallinity

(Masters et al., 2015; Kumar et al., 2017; Wan et al., 2017; Dapor et al., 2018; Stehling et al., 2018).

SEHI was performed on the silk surface to compare the secondary electron energy signatures of the skin of the as-spun fiber with those of plasma etched fiber. The resulting secondary electron signal arises from the surface of the sample, which in the case of the as-spun fiber is the lipid layer, and in the case of the 10 min plasma treated fiber is the outer-core. Indeed, the difference between the spectrum of the as-spun (**Figure 3A**, blue line) and the etched fiber (**Figure 3D**) is the increased spectral emission intensity of the as-spun surface at lower secondary electron energies of 0–3 eV, so that this energy window may be assigned to the very outer lipid and glycoprotein layer, in the following referred to as the coating. Thus, the 0–3 eV energy window may be characterized as "coating-like."

This hypothesis is further validated by the fact that the "coating-like" energy-window 0–3 eV, indicated by the dashed orange line, has increased intensity toward the edges of the as-spun fiber, where a higher fraction of the escaping secondary electrons have escaped from the electron-thin coating rather than the layers closer to the core (**Figure 3A** red line). Conversely, the higher energy range of 3–5 eV which exhibits higher intensity in the treated fiber can be characterized as the "core-like" window, as marked by the green dashed lines.

While SE information is generally considered to be from the very top surface, information depths of secondary electrons can range up to 100 nm in insulators (Seiler, 1983; Hessel and Gross, 1992). According to Sponner et al. the very outer coating containing lipid and glycoprotein layers around *Nephila* dragline silk only measure approximately 10–20 and 60 nm, respectively (Sponner et al., 2007), resulting in a contribution of the lower proteinous skin layer to the SE signal and spectrum in the untreated fiber—that is, the SE signal arising from the underlying protein layer shines through the coating and is collected by the detector. Note that the fibers investigated in this work are neither sputter coated nor stained, as is common practice for other electron imaging techniques (Yarger et al., 2018). Thus, the difference between the "coating-like" and "core-like" energy windows can be observed and is likely to arise from the different compositional make-ups of the layers, with the "coating-like" spectrum reflecting its lipid composition and the "core-like" region responding to proteinous layers.

This correlation between layer composition and emission energy can be exploited using SEHI to obtain spatially resolved compositional information in the form of hyperspectral images, which map the emission intensity of a certain energy range with increased brightness of a pixel translating to increased emission
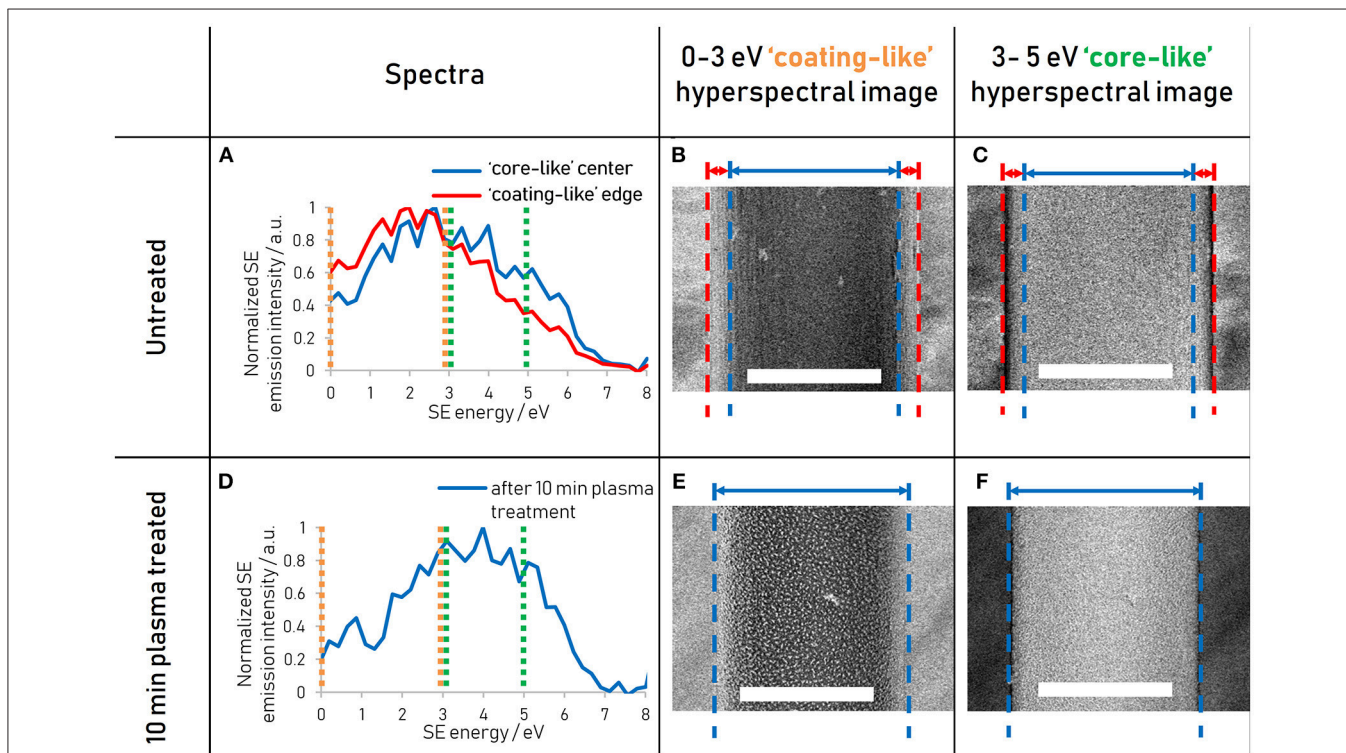

FIGURE 3 | **(A)** Spectra of untreated *Nephila inaurata* dragline silk highlighting differences between the coating-like spectrum arising from the edge (red lines) and the core-like spectrum arising form the middle (blue lines). **(B)** Hyperspectral image of the untreated fiber representing the energy range of 0–3 eV highlighting the coating-like emissions and **(C)** 3–5 eV energy range hyperspectral image highlighting the core-like emissions. **(D)** Spectrum of *Nephila inaurata* dragline silk after the removal of the coating and skin via a 10 min plasma etch. **(E)** and **(F)** as **(B)** and **(C)** for the 10 min treated sample. The hyperspectral energy ranges of 0–3 and 3–5 eV are represented by orange and green dashed lines in the spectra of **(A,D)**, respectively. All spectral images acquired with 500 eV primary beam energy. Scalebars measure 3 μm.

TABLE 1 | Summary of energy ranges used to isolate compositions on different scales.

Energy range/eV	Dominant SE signal response
0–3	Coating
1.5–4	Ordered nanostructure in core
3–5	Core with contribution from nanostructure
4–6	Disordered matrix in core

intensity (Wan et al., 2017). Note that these hyperspectral images are geometrically corrected to eliminate any potential image artifacts arising from angular dependencies of SE emission (for details please refer to the materials and methods section). As expected, the edges of the untreated fiber appear bright in the "coating-like" hyperspectral image (**Figure 3B**) and dark in the "core-like" hyperspectral image (**Figure 3C**), illustrating how the fraction of SEs emerging from the electron-thin coating gradually increases toward the fiber edge due to the cylindrical profile of the fiber. For the treated fiber, where the skin has been etched away, the "coating-like" hyperspectral image does exhibit bright edges, although this is readily explained by the fact that this energy range also responds to the nanostructures revealed by the plasma etching both at the edges and in the middle of the fiber, as seen clearly in the hyperspectral image (**Figure 3E**). The "core-like" hyperspectral image shows a uniform distribution of the gray levels across the fiber and especially at the edges in the treated fiber, illustrating how all SEs originate from the core layer (**Figure 3F**), whereas the "core-like" energy window in the untreated fiber shows a gradual reduction in gray levels as the number of SEs originating from the proteinous skin and core diminishes toward the edges (**Figure 3C**). Note how this energy window is not only insensitive to the difference in composition between the nanostructure and the matrix (**Figure 3F**), but also represses the topography arising from the different etching rates of the β-sheet crystals and amorphous regions.
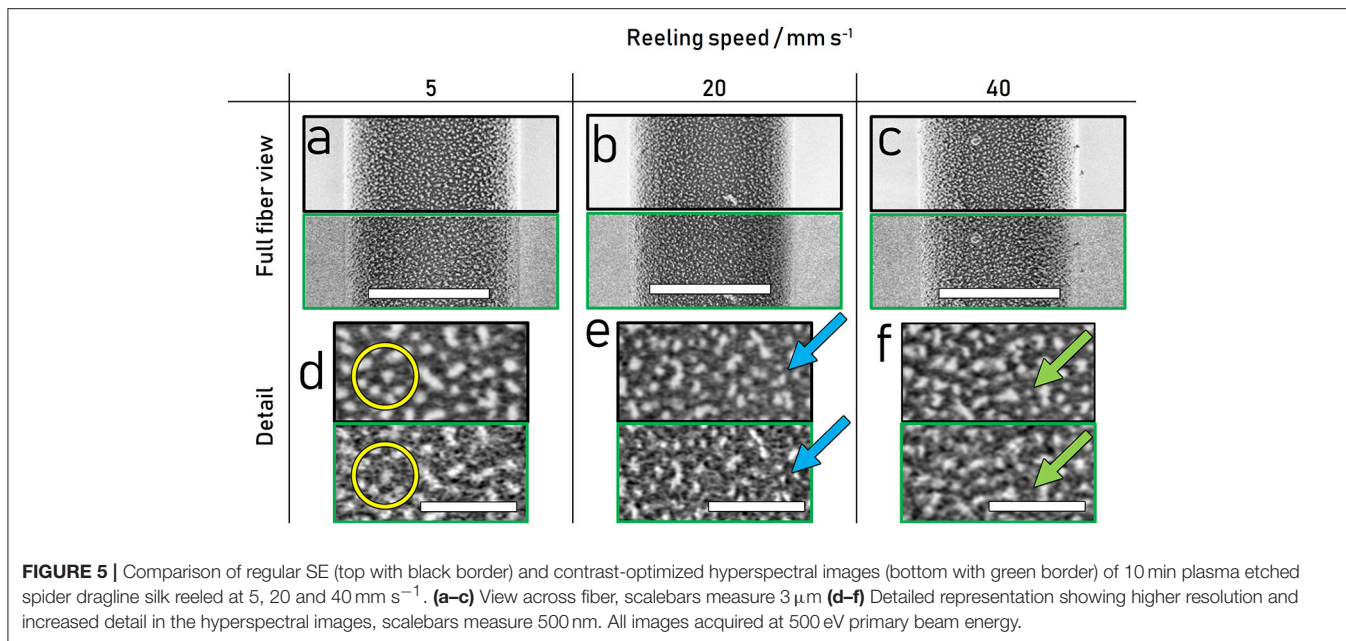
Analogously to the way the coating and the core energy signatures have been compared in **Figure 3**, the energy signature of the nanostructures present in the plasma treated fiber can be compared to that of the matrix by spatially separating the two phases using thresholding of the greyscale values (**Figure 4**). It is clear from the spectra that the nanostructure and the matrix are best distinguished in the energy ranges from 1.5 to 4 eV, where the nanostructure dominates, and from 4 to 6 eV, where the matrix dominates.

The energy ranges isolated for the different components are summarized in **Table 1**. These energy range assignments overlap and are not absolute, so that a quantification in this way using spectral intensities would be problematic. However, the assignment of energy ranges in this fashion allows the determination of optimal energy windows in which the contrast between two components will be amplified compared to a regular SE image.

Thus, the energy windows selected using the spectra in **Figure 4** were used to generate hyperspectral images to isolate the nanostructure, by adding the 1.5–4 eV hyperspectral image
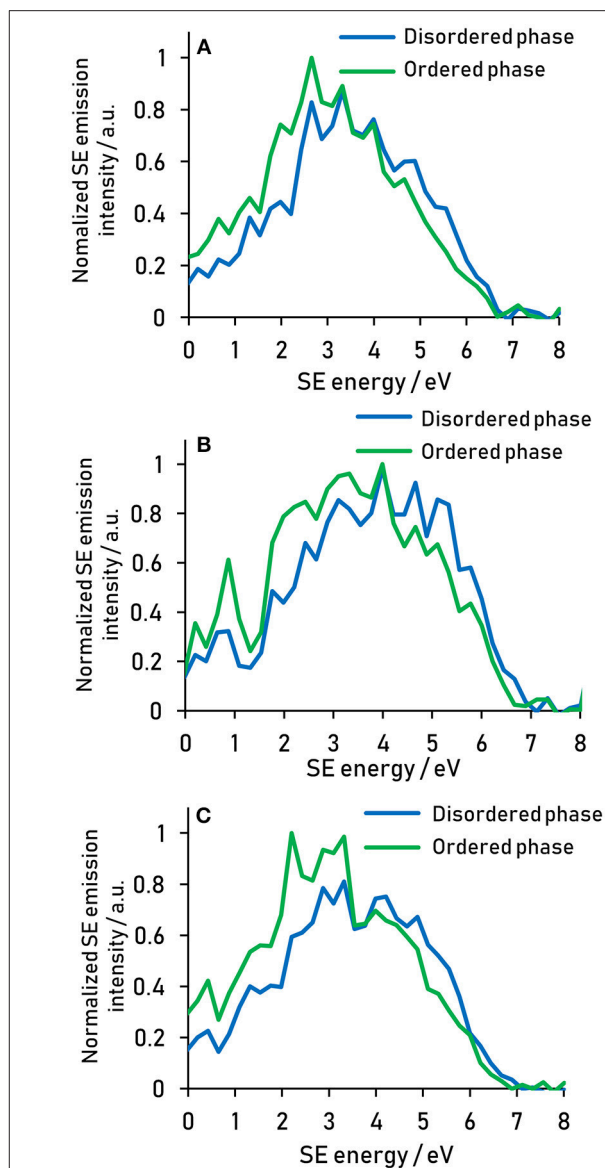
FIGURE 4 | Secondary electron spectral differences between the ordered nanostructure and the disordered matrix present after 10 min plasma treatment for reeling speeds of **(A)** 5 **(B)** 20, and **(C)** 40 mm s^{-1}. Spectra acquired at 500 eV primary beam energy.

to the inverse of the 4–6 eV hyperspectral image, as shown in **Figure 5**. The detailed images d-f illustrate how an isolation based on energy can yield a hyperspectral image with pinpointed information: The nanostructure appears less diffuse in the hyperspectral image compared to the regular SE images and resolves multiple smaller features which appear as one larger feature in the regular SE image (**Figure 5e** blue arrow). Importantly, besides increasing the apparent resolution of the energy-selected nanostructures, the selected energy range also reveals smaller scale structures present within the matrix, such as structures linking the larger particles highlighted in the yellow circle (**Figure 5d**) and sub 10 nm structures present in between

FIGURE 5 | Comparison of regular SE (top with black border) and contrast-optimized hyperspectral images (bottom with green border) of 10 min plasma etched spider dragline silk reeled at 5, 20 and 40 mm s^{-1}. **(a–c)** View across fiber, scalebars measure 3 μm **(d–f)** Detailed representation showing higher resolution and increased detail in the hyperspectral images, scalebars measure 500 nm. All images acquired at 500 eV primary beam energy.

the larger nanostructures highlighted by the green arrow in **Figure 5f**.
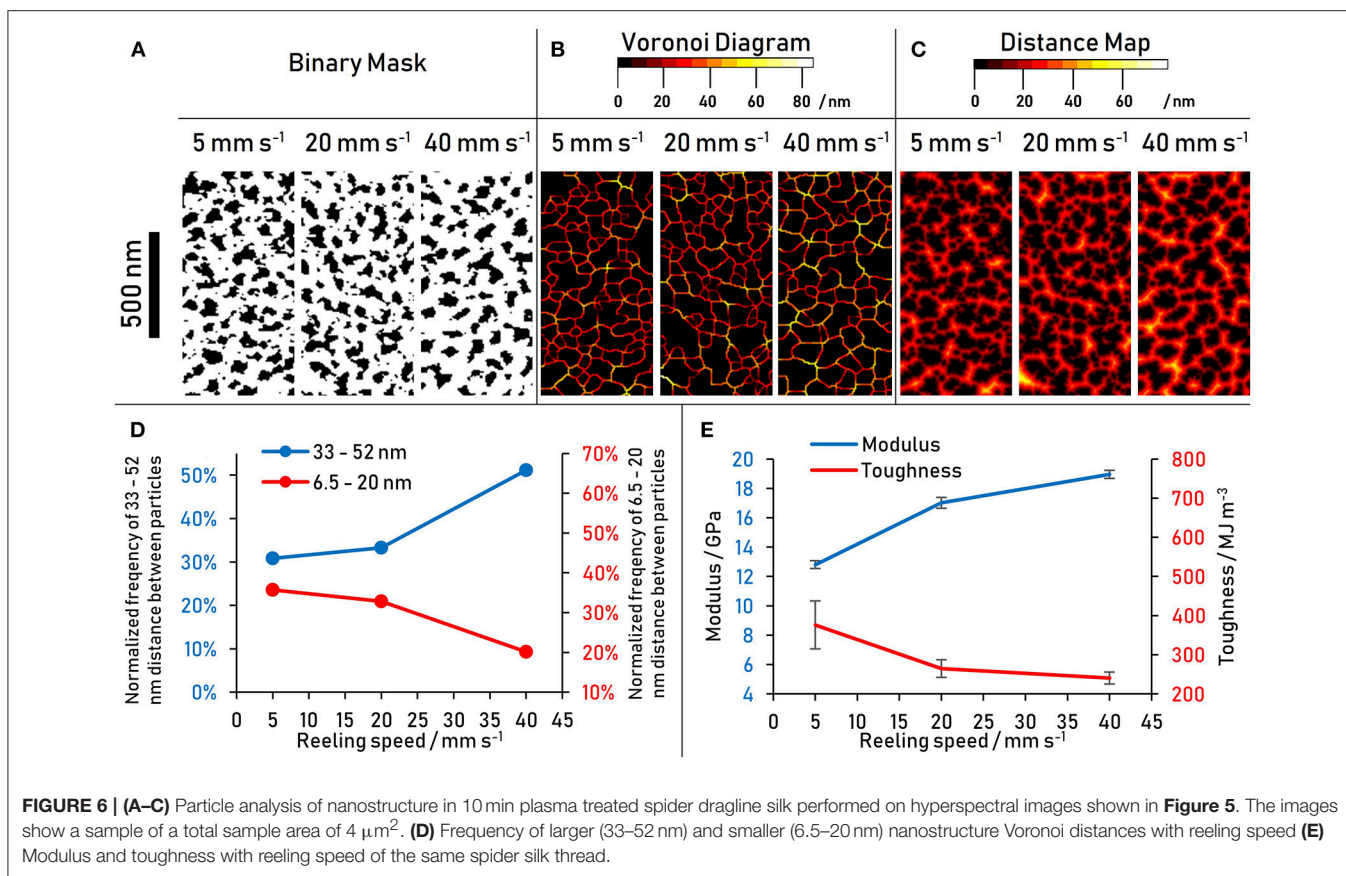
Currently these structures are barely resolved in the presented images and difficult to separate from noise. However, their presence in the nanostructure optimized image and absence in the corresponding regular SE image suggests their composition may lie in between the more ordered and disordered components. Higher resolution hyperspectral images of targeted energies may give a clearer picture of the nature of these structures.

The differences in nanostructure with varying reeling speed are not readily seen with the naked eye in the hyperspectral images in **Figure 5**. To characterize and quantify the nanostructure, different image analysis tools were applied to the hyperspectral images in **Figure 5**, with the results presented in **Figure 6**. Firstly, the bright nanostructures were isolated from the darker matrix using thresholding. The resulting binary images presented in **Figure 6A** were analyzed for the area fraction of the nanostructure and for its size distribution. The area fraction of the particles in the total sampled area decreased from 35 to 31 to 29% for the reeling speeds of 5, 20, and 40 mm s^{-1}, respectively. Interestingly, plotting the area distributions of the nanostructure as a histogram shows indications of a bi-modal distribution of nanostructure sizes consistent with literature (Trancik et al., 2006) (see **Figure S1**). However, there are limits to the area data recorded; Firstly, objects smaller than 6.5 nm cannot be resolved with the given image resolution, and secondly the total area is subject to error introduced by differences in brightness and contrast between images.

To eliminate the sensitivity to differences in brightness and contrast of the source images, a Voronoi tessellation was chosen as a processing tool because it considers only the center of the particle (in this case the nanostructure) and not its entire

area (Voronoi, 1908). Furthermore, it not only considers the properties of the structures, but also characterizes their location relative to one another. In a Voronoi tessellation as shown in **Figure 6B**, the tessellation lines run along where one particle center is equidistant to its nearest neighbor. The color value simultaneously encodes the magnitude of the distance of the Voronoi tessellation boundary to the center of either particle. The increased occurrence of higher distance values with increased reeling speed is evident from the Voronoi diagrams (**Figure 6B**) and the frequency histogram of the Voronoi tessellation was (**Figure S1**). This result is consistent with the indication of a bimodal size distribution of the area distribution, that is, the smaller reeling speeds have an increased number of particles smaller than 20 nm, which in turn results in the higher number of smaller particle distances seen in the Voronoi diagrams. Conversely, at higher reeling speeds the nanostructures are further apart from one another.

It seems then that it is not only the size and size distribution of nanostructures that matters, but also their distances from one-another within the matrix. This would imply that the interaction between the nanostructures and the matrix play an important role in the tensile properties of the outer core. To get a better understanding of the absolute numbers associated with particle distances (i.e., considering the size of the particles as well), the distance map of the binary images presented in **Figure 6A** were generated and analyzed (**Figure 6C**). The population of distances shows the same trend as the Voronoi tessellation distributions: at higher reeling speeds the smaller distances become less frequent while the larger distances become more frequent. This confirms that the trend is not only influenced by the size of a nanostructure, but also by the distribution of the matrix in between the particles. The result is a larger fraction of the matrix further away from any nanostructures at higher reeling speeds,

FIGURE 6 | (A–C) Particle analysis of nanostructure in 10 min plasma treated spider dragline silk performed on hyperspectral images shown in **Figure 5**. The images show a sample of a total sample area of 4 μm^2. **(D)** Frequency of larger (33–52 nm) and smaller (6.5–20 nm) nanostructure Voronoi distances with reeling speed **(E)** Modulus and toughness with reeling speed of the same spider silk thread.

resulting in less scope for matrix-nanostructure interactions and more prominent matrix-matrix interactions. The critical distance between nanostructures where the trend reverses is 20 nm, which may indicate that a bi-modal size distribution and thus a multi-scale organization is present not only within the crystalline nanostructure but also in the disordered domains.

Voronoi tessellation distances of 6.5–20 and 33–52 nm have been grouped to plot this trend in **Figure 6D**. The tensile results of the same silk thread (**Figure 6E**) are shown next to the results of the nanostructure analysis in an attempt to link nanoscale structure to macroscale properties. Assuming that the distribution of the ordered nanostructure within the fiber directly affects mechanical properties of the material, the data suggest that shorter distances between the ordered β-sheet crystals beget toughness, while larger distances contribute to a higher modulus. Potential explanations for this relationship are proposed in the Discussion section.

DISCUSSION

The size and orientation of the ordered domains and especially the β-sheet crystals within spider silk have been subject to intense experimental interest with regards to their contribution to the desirable tensile properties of spider silk (Yang et al., 1997; Riekel and Vollrath, 2001; Sampath et al., 2012; McGill et al., 2018). Thus, modeling studies have focused on their tensile behavior in isolation from the matrix on length scales

of atomistic to nanoscale models (Thiel et al., 1997; Keten et al., 2010; Giesa et al., 2011). The idea that the crystallinity alone is responsible for the dragline fiber's renowned mechanical response is in direct conflict with the fact that both minor ampullate spider silk of the same species and *Bombyx mori* silk have a substantially larger crystalline fraction and less desirable tensile properties (Riekel and Vollrath, 2001; Sampath et al., 2012). The results in this study suggest that the matrix and specifically the matrix-nanostructure interactions are key in the tensile response of the fibers. Although there are promising developments in elucidating the secondary structure and general organization of the amorphous phase (McGill et al., 2018), its inherent lack of order has posed a challenge to the structural analysis community as it cannot be readily described using most methods applied to the crystalline fractions of the fiber. This gives us a possible explanation why there is an underappreciation for its role in spider silk's mechanical response. Although this hypothesis requires further validation, our results suggest that the modulus is governed though the matrix-matrix interactions, whereas matrix-nanocrystal interactions supply a toughening mechanism especially at lower reeling speeds. Through their X-ray and NMR work, Grubb and Jelinski have come to a similar conclusion; that is that spider silk is best described on the macroscale as a filled elastomer, with the β-sheets acting as fillers to enhance the mechanical properties of the rubber-like amorphous and ordered amorphous matrix (Simmons et al., 1996; Grubb and Jelinski, 1997).

To link the parameters given by atomistic models to a larger scale, spider silk fiber has been modeled as a bundle of nanofibrils with diameters of 20–150 nm (Giesa et al., 2011). Initially thought to be cylindrical and spatially confined like those observed in *Bombyx mori* silk, more recent AFM and TEM studies have shown more diffuse structures which are oriented in the fiber direction, with some models considering spider silk thread as a bundle of fibrils (Giesa et al., 2011; Xu et al., 2014) or globules (Cranford, 2013). A directional anisotropy of structures on such length scales were not evident in this work, with the orientation of the exposed nanostructure in the outer-core being broadly isotropic. The size of the revealed structures is however consistent with accounts of a bi-modal size distribution of the higher-order fractions (Trancik et al., 2006). In our current work we see indications of the smaller size population, especially using hyperspectral imaging, although it is still below the resolution limit. Our dominant observed nanostructure is consistent with the larger population of ordered structures of 20–150 nm extension transverse to the fiber direction. The use of SEHI in combination with low temperature plasma etching provides access to a larger number of particles compared to data published in previous AFM (Miller et al., 1999; Du et al., 2006; Schäfer et al., 2008; Brown et al., 2011; Wang and Schniepp, 2018) and TEM (Thiel et al., 1997; Trancik et al., 2006) studies. This is essential to build a quantitative picture of nano- and microstructure distribution, especially considering that spider silk modeling approaches have yet to incorporate our knowledge of these multi-scale structures (Yarger et al., 2018). The various approaches taken to date in the mechanistic modeling of spider silk have been summed up in a recent review (López Barreiro et al., 2018). Various modeling approaches have had some success in reproducing spider silk's mechanical behavior but the incorporation of multiscale structures and their interactions into mechanistic models is yet to be realized in part due to the practical difficulty of liking atomistic approaches to micron scale models.

A complete 3D model of spider silk with its multi-scale organization is additionally hampered by the difficulties of revealing its internal make-up. The largest single fiber silk from a large spider only measures around 5 μm in diameter to start with, and provenly exhibits structures down to 2 nm in size (Trancik et al., 2006). Furthermore, the structures under investigation are sensitive to strain, thermal and chemical treatment and can undergo undesired and unknown structural modification through sample preparation. Thus, it cannot simply be cut or sectioned without potentially manipulating the structures of interest. Previously reported sample preparation procedures employ epoxy embedding, which cures exothermically and may result in thermal modification of fibers, and wax embedding involving solvent dehydration, embedding in molten wax, and rehydration steps. While the results contributed from these studies supply important pieces to the puzzle, such as the observation of a differential in mechanical properties between the inner and the outer core (Brown et al., 2011), it must be kept in mind that the fiber may have been substantially chemically transformed.

In this work we have used low-temperature plasma etching as a non-thermal, surface-acting technique. Previous work

considering the surface modifications of polyamide(6,6) fibers in low temperature plasma establish that the surface morphology after plasma treatment is a result of the sample's crystallinity content and strain history (Yip et al., 2006), which makes this approach especially suitable for the analysis of spider silk force reeled at different speeds. While the methodology requires further optimization, we were able to identify differences in the resulting morphology with reeling speed exposed in the outer-core of the fiber. We show that comparably, plasma treatment may be a mild preparation method to uncover certain layers within the radial structure of spider silk.

Compared to conventional spatially resolved techniques such as conventional SEM, TEM and AFM our secondary electron hyperspectral imaging (SEHI) has key advantages when imaging spider silk and associated nanostructures. The Low-Voltage SEM imaging requires no sample preparation besides the plasma treatment, and thus eliminates potentially damaging or obscuring processes such as coating or staining. Our comparison of SE spectra and hyperspectral images illustrates how powerful this method is in distinguishing natural organic materials and compositions, such as lipids and proteins, while simultaneously enabling the suppression of topographical information of SEs. Secondly, through the systematic selection of energy ranges, we have increased the compositional contrast between the nanostructures and the matrix, revealing structures which are not visible in a conventional SE image. In future studies this approach will be further developed to resolve the sub 10 nm features prevalent in the matrix in between the larger nanostructures, especially in the lower reeling speeds.

We present low temperature plasma etching as a novel tool to uncover layers along the radial profile of *Nephila* spider silk. The use of Secondary Electron Hyperspectral Imaging (SEHI) has allowed high resolution mapping of the different compositions of the components contributing to the multi-scale design of dragline silk, with distinct energy signatures arising from the skin and core on the microscale, and the nanostructures and matrix on the nanoscale. The use of these energy ranges in hyperspectral images has revealed smaller scale structures than those evident in regular SE images. While there were no significant differences in nanostructure area fraction and orientation with reeling speed, the spatial situation of the >20 nm nanostructures is shown to change, with larger distances between nanostructures prevalent at higher reeling speeds.

The combination of plasma etching, LV-SEM, and SEHI provides a top-down approach for the structural analysis of spider silk which bridges multiple length scales and supplies compositional and spatial information simultaneously. Further work will involve varying etching times and thus exposing fiber layers systematically to obtain an extensive dataset illustrating the radial evolution of nanostructures within the fiber. Specifically, such a dataset will serve to bridge the length scale gaps between the current molecular and larger scale models and will help to map out the yet poorly defined disordered domains and the situation of the ordered domains within. A multiscale mechanical model capable of incorporating this information and reproducing silk's complex tensile behavior will be a large step forward in engineering structure-property relationships for bio-inspired man-made materials.

AUTHOR CONTRIBUTIONS

FUNDING

ACKNOWLEDGMENTS

SUPPLEMENTARY MATERIAL

The Supplementary Material for this article can be found online at: https://www.frontiersin.org/articles/10.3389/fmats.2018.00084/full#supplementary-material

REFERENCES

Augsten, K., Muehlig, P., and Herrmann, C. (2000). Glycoproteins and skin-core structure in Nephila clavipes spider silk observed by light and electron microscopy. *Scanning* 22, 12–15. doi: 10.1002/sca.4950220103

Boulet-Audet, M., Vollrath, F., and Holland, C. (2015). Identification and classification of silks using infrared spectroscopy. *J. Exp. Biol.* 218, 3138–3149. doi: 10.1242/jeb.128306

Brown, C. P., MacLeod, J., Amenitsch, H., Cacho-Nerin, F., Gill, H. S., Price, A. J., et al. (2011). The critical role of water in spider silk and its consequence for protein mechanics. *Nanoscale* 3, 3805–3811. doi: 10.1039/c1nr10502g

Cebe, P., Hu, X., Kaplan, D. L., Zhuravlev, E., Wurm, A., Arbeiter, D., et al. (2013). Beating the heat-fast scanning melts silk beta sheet crystals. *Sci. Rep.* 3:1130. doi: 10.1038/srep01130

Cranford, S. W. (2013). Increasing silk fibre strength through heterogeneity of bundled fibrils. *J. R. Soc. Interface* 10:20130148. doi: 10.1098/rsif.2013.0148

Dapor, M., Masters, R. C., Ross, I., Lidzey, D. G., Pearson, A., Abril, I., et al. (2018). Secondary electron spectra of semi-crystalline polymers – A novel polymer characterisation tool? *J. Electron Spectros. Relat. Phenomena* 222, 95–105. doi: 10.1016/j.elspec.2017.08.001

Dicko, C., Porter, D., Bond, J. E., Kenney, J. M., and Vollrath, F. (2007). Structural disorder in silk proteins reveals the emergence of elastomericity. *Biomacromolecules* 9, 216–21. doi: 10.1021/bm701069y

Du, N., Liu, X. Y., Narayanan, J., Li, L., Lim, M. and Li, D. (2006). Design of superior spider silk: from nanostructure to mechanical properties. *Biophys. J.* 91, 4528–4535. doi: 10.1529/biophysj.106.089144

Ebrahimi, D., Tokareva, O., Rim, N. G., Wong, J. Y., Kaplan, D. L., and Buehler, M. J. (2015). Silk–its mysteries, how it is made, and how it is used. *ACS Biomater. Sci. Eng.* 1, 864–876. doi: 10.1021/acsbiomaterials.5b00152

Frische, S., Maunsbach, A. B., and Vollrath, E. (2002). Elongate cavities and skin–core structure in Nephila spider silk observed by electron microscopy. *J. Microsc.* 189, 64–70. doi: 10.1046/j.1365-2818.1998.00285.x

Giesa, T., Arslan, M., Pugno, N. M., and Buehler, M. J. (2011). Nanoconfinement of spider silk fibrils begets superior strength, extensibility, and toughness. *Nano Lett.* 11, 5038–5046. doi: 10.1021/nl203108t

Greving, I., Dicko, C., Terry, A., Callow, P., and Vollrath, F. (2010). Small angle neutron scattering of native and reconstituted silk fibroin. *Soft. Matter.* 6, 4389–4395. doi: 10.1039/c0sm00108b

Grubb, D. T., and Jelinski, L. W. (1997). Fiber morphology of spider silk: the effects of tensile deformation. *Macromolecules* 30, 2860–2867. doi: 10.1021/ma961293c

Hessel, R., and Gross, B. (1992). Escape depth of secondary electrons from electron-irradiated polymers. *IEEE Trans. Electr. Insul.* 27, 831–834. doi: 10.1109/14.155806

Hijirida, D. H., Do, K. G., Michal, C., Wong, S., Zax, D., and Jelinski, L. W. (1996). 13C NMR of Nephila clavipes major ampullate silk gland. *Biophys. J.* 71, 3442–3447. doi: 10.1016/S0006-3495(96)79539-5

Holland, C., Hawkins, N., Frydrych, M., Laity, P., Porter, D., and Vollrath, F. (2018a). Differential scanning calorimetry of native silk feedstock. *Macromol. Biosci.* 9:1800228. doi: 10.1002/mabi.201800228

Holland, C., Numata, K., J., Rnjak-Kovacina, and Seib, F. P. (2018b). The biomedical use of silk: past, present, future. *Adv. Healthc. Mater.* 8:1800465. doi: 10.1002/adhm.201800465

Holland, G. P., Creager, M. S., Jenkins, J. E., Lewis, R. V., and Yarger, J. L. (2008). Determining secondary structure in spider dragline silk by carbon–carbon correlation solid-state NMR spectroscopy. *J. Am. Chem. Soc.* 130, 9871–9877. doi: 10.1021/ja8021208

Kazemian, P., S.,Mentink, A. M., Rodenburg, C., and Humphreys, C. J. (2007). Quantitative secondary electron energy filtering in a scanning electron microscope and its applications. *Ultramicroscopy* 107, 140–150. doi: 10.1016/j.ultramic.2006.06.003

Keten, S., Xu, Z., Ihle, B., and Buehler, M. J. (2010). Nanoconfinement controls stiffness, strength and mechanical toughness of [beta]-sheet crystals in silk. *Nat. Mater.* 9, 359–367. doi: 10.1038/nmat2704

Kitagawa, M., and Kitayama, T. (1997). Mechanical properties of dragline and capture thread for the spider Nephila clavata. *J. Mater. Sci.* 32, 2005–2012. doi: 10.1023/A:1018550116930

Knight, D. P., Knight, M. M., and Vollrath, F. (2000). Beta transition and stress-induced phase separation in the spinning of spider dragline silk. *Int. J. Biol. Macromol.* 27, 205–210. doi: 10.1016/S0141-8130(00)00124-0

Koeppel, A., and Holland, C. (2017). Progress and trends in artificial silk spinning: a systematic review. *ACS Biomater. Sci. Eng.* 3, 226–237. doi: 10.1021/acsbiomaterials.6b00669

Kumar, V., Schmidt, W. L., Schileo, G., Masters, R. C., Wong-Stringer, M., Sinclair, D. C., et al. (2017). Nanoscale mapping of bromide segregation on the cross sections of complex hybrid perovskite photovoltaic films using secondary electron hyperspectral imaging in a scanning electron microscope. *ACS Omega* 2, 2126–2133. doi: 10.1021/acsomega.7b00265

Kümmerlen, J., Van Beek, J. D., Vollrath, F., and Meier, B. H. (1996). Local structure in spider dragline silk investigated by two-dimensional spin-diffusion nuclear magnetic resonance. *Macromolecules* 29, 2920–2928. doi: 10.1021/ma951098i

Li, S. F., McGhie, A. J., and Tang, S. L. (1994). New internal structure of spider dragline silk revealed by atomic force microscopy. *Biophys. J.* 66, 1209–1212. doi: 10.1016/S0006-3495(94)80903-8

Lin, T. Y., Masunaga, H., Sato, R., Malay, A. D., Toyooka, K., Hikima, T., et al. (2017). Liquid crystalline granules align in a hierarchical structure to produce spider dragline microfibrils. *Biomacromolecules* 18, 1350–1355. doi: 10.1021/acs.biomac.7b00086

Liu, Y., Shao, Z., and Vollrath, F. (2005). Relationships between supercontraction and mechanical properties of spider silk. *Nat. Mater.* 4, 901–905. doi: 10.1038/nmat1534

López Barreiro, D., Yeo, J., Tarakanova, A., F. J., Martin-Martinez, and Buehler, M. J. (2018). Multiscale modeling of silk and silk-based biomaterials—a review. *Macromol. Biosci.* e1800253. doi: 10.1002/mabi.201800253. [Epub ahead of print].

Masters, R. C., Pearson, A. J., Glen, T. S., F.-,Sasam, C., Li, L., Dapor, M., et al. (2015). Sub-nanometre resolution imaging of polymer-fullerene photovoltaic blends using energy-filtered scanning electron microscopy. *Nat. Commun.* 6:6928. doi: 10.1038/ncomms7928

McGill, M., Holland, G. P., and Kaplan, D. L. (2018). Experimental methods for characterizing the secondary structure and thermal properties of silk proteins. *Macromol. Rapid Commun.* 40:e1800390. doi: 10.1002/marc.201800390

Miller, L. D., Putthanarat, S., Eby, R. K., and Adams, W. W. (1999). Investigation of the nanofibrillar morphology in silk fibers by small angle X-ray scattering and atomic force microscopy. *Int. J. Biol. Macromol.* 24, 159–165. doi: 10.1016/S0141-8130(99)00024-0

Nova, A., Keten, S., Pugno, N. M., Redaelli, A., and Buehler, M. J. (2010). Molecular and nanostructural mechanisms of deformation, strength and toughness of spider silk fibrils. *Nano Lett.* 10, 2626–2634. doi: 10.1021/nl101341w

Oktaviani, N. A., Matsugami, A., Malay, A. D., Hayashi, F., Kaplan, D. L., and Numata, K. (2018). Conformation and dynamics of soluble repetitive domain elucidates the initial β-sheet formation of spider silk. *Nat. Commun.* 9:2121. doi: 10.1038/s41467-018-04570-5

Parent, L. R., Onofrei, D., Xu, D., Stengel, D., Roehling, J. D., Addison, J. B., et al. (2018). Hierarchical spidroin micellar nanoparticles as the fundamental precursors of spider silks. *Proc. Natl. Acad. Sci. U.S.A.* 115, 11507–11512. doi: 10.1073/pnas.1810203115

Porter, D., Guan, J., and Vollrath, F. (2013). Spider silk: super material or thin fibre? *Adv. Mater.* 25, 1275–1279. doi: 10.1002/adma.201204158

Riekel, C., Madsen, B., Knight, D., and Vollrath, F. (2000). X-ray diffraction on spider silk during controlled extrusion under a synchrotron radiation X-ray beam. *Biomacromolecules* 1, 622–626. doi: 10.1021/bm000047c

Riekel, C., Rössle, M., Sapede, D., and Vollrath, F. (2004). Influence of CO_2 on the micro-structural properties of spider dragline silk: X-ray microdiffraction results. *Naturwissenschaften* 91, 30–33. doi: 10.1007/s00114-003-0482-8

Riekel, C., and Vollrath, F. (2001). Spider silk fibre extrusion: combined wide- and small-angle X-ray microdiffraction experiments. *Int. J. Biol. Macromol.* 29, 203–210. doi: 10.1016/S0141-8130(01)00166-0

Rim, N. G., Roberts, E. G., Ebrahimi, D., Dinjaski, N., Jacobsen, M. M., Martín-Moldes, Z., et al. (2017). Predicting silk fiber mechanical properties through multiscale simulation and protein design. *ACS Biomater. Sci. Eng.* 3, 1542–1556. doi: 10.1021/acsbiomaterials.7b00292

Sampath, S., Isdebski, T., Jenkins, J. E., V., Ayon, J., Henning, R. W., et al. (2012). X-ray diffraction study of nanocrystalline and amorphous structure within major and minor ampullate dragline spider silks. *Soft. Matter.* 8, 6713–6722. doi: 10.1039/c2sm25373a

Schäfer, A., Vehoff, T., Glišović, A., and Salditt, T. (2008). Spider silk softening by water uptake: an AFM study. *Eur. Biophys. J.* 37, 197–204. doi: 10.1007/s00249-007-0216-5

Schindelin, J., Arganda-Carreras, I., Frise, E., Kaynig, V., Longair, M., Pietzsch, T., et al. (2012). Fiji: an open-source platform for biological-image analysis. *Nat. Methods* 9:676. doi: 10.1038/nmeth.2019

Seiler, H. (1983). Secondary electron emission in the scanning electron microscope. *J. Appl. Phys.* 54, R1–R18. doi: 10.1063/1.332840

Simmons, A. H., Michal, C. A., and Jelinski, L. W. (1996). Molecular orientation and two-component nature of the crystalline fraction of spider dragline silk. *Science* 271, 84–87. doi: 10.1126/science.271.5245.84

Skelton, R. E., and Nagase, K. (2012). Tensile tensegrity structures. *Int. J. Sp. Struct.* 27, 131–137. doi: 10.1260/0266-3511.27.2-3.131

Sponner, A., Unger, E., Grosse, F., and Weisshart, K. (2005). Differential polymerization of the two main protein components of dragline silk during fibre spinning. *Nat. Mater.* 4, 772–775. doi: 10.1038/nmat1493

Sponner, A., Vater, W., Monajembashi, S., Unger, E., Grosse, F., and Weisshart, K. (2007). Composition and hierarchical organisation of a spider silk. *PLoS ONE* 2:e998. doi: 10.1371/journal.pone.0000998

Stehling, N., Masters, R., Zhou, Y., O'Connell, R., Holland, C., Zhang, H., et al. (2018). New perspectives on nano-engineering by secondary electron spectroscopy in the helium ion and scanning electron microscope. *MRS Commun.* 8, 226–240. doi: 10.1557/mrc.2018.75

Termonia, Y. (1994). Molecular modeling of spider silk elasticity. *Macromolecules* 27, 7378–7381. doi: 10.1021/ma00103a018

Thiel, B. L., Guess, K. B., and Viney, C. (1997). Non-periodic lattice crystals in the hierarchical microstructure of spider (major ampullate) silk. *Biopolym. Orig. Res. Biomol.* 41, 703–719. doi: 10.1002/(SICI)1097-0282(199706)41:7&<;703::AID-BIP1&>;3.0.CO;2-T

Trancik, J. E., Czernuszka, J. T., Bell, F. I., and Viney, C. (2006). Nanostructural features of a spider dragline silk as revealed by electron and X-ray diffraction studies. *Polymer* 47, 5633–5642. doi: 10.1016/j.polymer.2005.01.110

Vollrath, F., Hawkins, N., Porter, D., Holland, C., and M., Boulet-Audet (2014). Differential scanning fluorimetry provides high throughput data on silk protein transitions. *Sci. Rep.* 4:5625. doi: 10.1038/srep05625

Vollrath, F., and Knight, D. P. (2001). Liquid crystalline spinning of spider silk. *Nature* 410, 541–548. doi: 10.1038/35069000

Vollrath, F., and Porter, D. (2009). Silks as ancient models for modern polymers. *Polymer* 50, 5623–5632. doi: 10.1016/j.polymer.2009.09.068

Vollrath, F., Porter, D., and Holland, C. (2011). There are many more lessons still to be learned from spider silks. *Soft Matter* 7, 9595–9600. doi: 10.1039/c1sm05812f

Voronoi, G. (1908). Nouvelles applications des paramètres continus à la théorie des formes quadratiques. Deuxième mémoire. Recherches sur les parallélloèdres primitifs. *J. Für Die Reine Und Angew. Math.* 134, 198–287.

Wagner, J. A., Patil, S. P., Greving, I., Lämmel, M., Gkagkas, K., Seydel, T., et al. (2017). Stress-induced long-range ordering in spider silk. *Sci. Rep.* 7:15273. doi: 10.1038/s41598-017-15384-8

Wakida, T., and Tokino, S. (1996). Surface modification of fibre and polymeric materials by discharge treatment and its application to textile processing. *Indian J. Fibre Textile Res.* 21, 69–78.

Walker, A. A., Holland, C., and Sutherland, T. D. (2015). More than one way to spin a crystallite: multiple trajectories through liquid crystallinity to solid silk. *Proc. R. Soc. B* 282:20150259. doi: 10.1098/rspb.2015.0259

Wan, Q., K. J., Abrams, K. J., R. C., Masters, R. C., Talari, A. C. S., Rehman I. U., Claeyssens, F., et al. (2017). Mapping nanostructural variations in silk by secondary electron hyperspectral imaging. *Adv. Mater.* 29:1703510. doi: 10.1002/adma.201703510

Wang, Q., and Schniepp, H. C. (2018). Strength of recluse Spider's silk originates from nanofibrils. *ACS Macro Lett.* 7, 1364–1370. doi: 10.1021/acsmacrolett.8b00678

Willis, R. F., Fitton, B., and Skinner, D. K. (1972). Study of carbon-fiber surfaces using Auger and secondary electron emission spectroscopy. *J. Appl. Phys.* 43, 4412–4419. doi: 10.1063/1.1660936

Xu, G., Gong, L., Yang, Z., and Liu, X. Y. (2014). What makes spider silk fibers so strong? From molecular-crystallite network to hierarchical network structures. *Soft Matter* 10, 2116–2123. doi: 10.1039/C3SM52845F

Yang, Z., Grubb, D. T., and Jelinski, L. W. (1997). Small-angle X-ray scattering of spider dragline silk. *Macromolecules* 30, 8254–8261. doi: 10.1021/ma970548z

Yang, Z., Liivak, O., Seidel, A., LaVerde, G., Zax, D. B., and Jelinski, L. W. (2000). Supercontraction and backbone dynamics in spider silk: 13C and 2H NMR studies. *J. Am. Chem. Soc.* 122, 9019–9025. doi: 10.1021/ja0017099

Yarger, J. L., Cherry, B. R., and A., Van Der Vaart (2018). Uncovering the structure–function relationship in spider silk. *Nat. Rev. Mater.* 3:18008. doi: 10.1038/natrevmats.2018.8

Yazawa, K., Malay, A. D., Masunaga, H., and Numata, K. (2018). Role of skin layers on mechanical properties and supercontraction of spider dragline silk fiber. *Macromol. Biosci.* 1800220. doi: 10.1002/mabi.201800220. [Epub ahead of print].

Yip, J., Chan, K., Sin, K. M., and Lau, K. S. (2002). Low temperature plasma-treated nylon fabrics. *J. Mater. Process. Technol.* 123, 5–12. doi: 10.1016/S0924-0136(02)00024-9

Yip, J., Chan, K., Sin, K. M., and Lau, K. S. (2002). Study of plasma-etched and laser-irradiated polyamide materials. *Mater. Res. Innov.* 6, 44–50. doi: 10.1007/s10019-002-0169-3

Yip, J., Chan, K., Sin, K. M., and Lau, K. S. (2006). Formation of periodic structures by surface treatments of polyamide fiber: part II. Low temperature plasma treatment. *Appl. Surf. Sci.* 253, 2493–2497. doi: 10.1016/j.apsusc.2006.05.004

Zhang, T. Y., and Suen, C. Y. (1984). A fast parallel algorithm for thinning digital patterns. *Commun. ACM* 27, 236–239. doi: 10.1145/357994.358023

8 Conclusion

The key findings of the two papers and two results chapters of this thesis are summarised in the following.

In Chapter 4, the publication "New perspectives on nano-engineering by secondary electron spectroscopy in the helium ion and scanning electron microscope" highlights the current capabilities and future potential of utilising secondary electron energy in helium ion and scanning electron microscopes. The limitations of available instrumentation are discussed both theoretically and in light of experimental data. Simultaneously it is demonstrated that—through the exclusion of topography in select SE energy windows and the sensitivity of the measurement to surface changes— secondary electron spectroscopy and secondary electron hyperspectral imaging have immense potential for the nanostructural and nanocompositional analysis of beam sensitive materials. Thus, it is shown that using electron energy spectra can inform the microscope operator about contamination and damage processes and thus overcome a key limitation of this surface sensitive technique. It is suggested that the secondary electron energy signal may also be of use in automated process control for innovative new methods.

The general challenges of low-voltage SEM of uncoated insulating samples and the limitations of the SE energy filter set-up used in this work are mitigated by the deliberate selection of imaging parameters, as demonstrated in Chapter 5. Parameters must be optimised case-by-case for the respective sample and experimental set-up, however the results presented lead to the recommendation of an optimisation workflow which builds on past considerations in the literature but for the first time considers modern image capture developments, such as the increased user control over primary

beam voltage, currents and scan patterns. It is argued that the limited control of the user over the scan pattern is currently a limitation for the imaging of insulators, and potential future instrumental developments are proposed which may optimise the way in which beam-sensitive samples are irradiated in space and time. Through rigorous analysis of the data, it is shown that automated multivariate analysis of large spectral datasets is exceedingly useful for deducing spectral trends with varying parameters. The chapter concludes with a recommended workflow for low voltage secondary electron imaging, and secondary electron spectroscopic acquisition.

Building on Chapter 5, Chapter 6 presents sample preparation workflows for spectral imaging of the cross-sections of natural proteinaceous materials. Novel ways of producing cryo-fractured spider dragline silk cross-sections for spectral imaging at liquid nitrogen and room temperatures are presented as an alternative to previous sample preparation methods, which may have had a detrimental effect on the material itself. Plasma treatment has proven useful in two different applications for this project: firstly, the ex-situ non-thermal atmospheric plasma treatment of spider silk fibres results in a surface roughening effect which proves to be exceptionally effective for increasing fibre-matrix adhesion and inducing—to the authors knowledge—the first reported cryo-fracture of a spider silk fibre in plane with the matrix. Secondly, the inbuilt reactive oxygen plasma of the Helios SEM has been shown to be effective at removing hydrocarbon contamination to give access to the true sample surface. For the first time, the use of multivariate analysis confirms that hydrocarbon contamination has a very characteristic spectrum—this is immensely important and useful for future work, as it means that contamination can be reliably identified through spectral measurement and can therefore be mitigated. Once the hydrocarbon layer is removed it is shown that there are subtle differences in the average spectra of melanin and keratin-rich regions of a peacock feather section. These differences are significantly more apparent in the

targeted SE energy hyperspectral images through a contrast reversal in the relevant areas—signifying the possibility to map different organic compositions within a complex hierarchical structural polymer.

In the second publication presented as part of this thesis—"Revealing Spider Silk's 3D Nanostructure Through Low Temperature Plasma Etching and Advanced Low-Voltage SEM"—an ex-situ non-thermal reactive oxygen plasma is used to etch away layers on spider dragline silk radially, exposing nanostructure on the surface. It is shown that secondary electron spectra correspond to compositional differences in the radial structure and nanostructure of the fibre. The systematic selection of energy produces hyperspectral images with increased resolution of the nanostructures of interest, and in a further step the spatial distribution of the exposed nanostructure is characterised and correlated to macroscale tensile properties of the fibres. Combining plasma etching with secondary electron hyperspectral imaging is proposed as a vehicle towards mapping the 3D spatial distribution of the more and less ordered domains present within, which will ultimately inform future mechanical models of spider silk and provide blueprints for synthetic material designs.

A continuation of this work would lie in combining the parameterisation methodology of chapter 5 and the practical considerations of chapter 6 in further cryo–SEM work, to compare room temperature and cryogenic spectra with the aim of pinpointing differences in the nanomechanical make-up of biopolymers and particularly the role of water. A cryo–microtome may assist in obtaining favourable sections of biopolymers for analysis and would simultaneously allow comparison with TEM results.

On a higher level, this work highlights the need for purpose-built secondary electron energy analysers for this field to advance. This would entail well-characterised electron energy analysers, with energy and angular collection efficiencies of such systems being a base requirement for reproducibility between instruments. Consistency between

systems would allow the construction of data bases for reference materials—and crucially contamination and beam deposition markers—which are the basis of success for established spectroscopies such as X-ray and RAMAN spectroscopy. EELS and Auger spectroscopy research is ahead of secondary electron spectroscopy as far as technical— specifically electron optical—challenges are concerned and may serve as a source of inspiration with respect to detector designs and data processing strategies.

To fully understand which electronic state of the material probed in an SE spectrum, further research is required to characterise the time-dependent response of insulating materials to the electron beam, and the role of beam voltage and current on the irradiation process kinetics of a material. Promising developments in this regard are the ultrafast pulsed electron beam and the wider access to customisable scanning patterns, which are relevant to FIB and STEM work as well.

Overall, this work contributes to the understanding of complex hierarchical polymers by combining novel sample preparation processes, systematic optimisation of secondary electron spectral acquisition and targeted hyperspectral imaging. Differences in the internal composition of spider silk and pigmented feathers was mapped successfully using the secondary electron signal only, a method with scope to increase spatial resolution in future. In the process, multiple sample preparation and statistical data analysis protocols were developed which may prove useful for the wider scientific field.

9 Appendix

9.1 Code for non-negative matrix factorisation in Matlab 2017b

(see overleaf)

```matlab
% Performns a non-negative matrix factorisation on thee dimensional image
% data stacks.
%% initialise
clear
clc
stackDiff = [];
keepOn = true;
iterations = 0;
imagePathNoName = 'C:\Users\Niki\Google Drive\PhD\Results\SEM';
waitbarSections = 3;
%% create user interface for input
[dim, xy_smooth, z_smooth, do_diff] = user_input();
%% Get stack
while keepOn
    clear stack
    [imageName, imagePath] = uigetfile('*.tif','Please choose a stack for the PCA');
    waitBar = waitbar(0/waitbarSections,'Loading stack', 'Name', 'PCA progress');
    imagePathNoName = imagePath;
    imagePath = [imagePath imageName];
    %%
    info = imfinfo(imagePath);
    num_images = numel(info);
    if ~exist('resY','var')
        resY = info(1).Height;
        resX = info(1).Width;
    else
        resY = [resY ; info(1).Height];
        resX = [resX; info(1).Width];
    end
    if mean(mean(imread(imagePath,1))) < mean(mean(imread(imagePath,num_images))) %↙
you don't want to do a nnmf on negative data...
        readOrder = 1:num_images;
    else
        readOrder = num_images:-1:1;
    end
    %%
    n = 1;
    for k = readOrder
        stack(:,:,n) = imread(imagePath, k);
        n = n+1;
    end
    stack = double(stack);
    if isvalid(waitBar)
        waitbar(1/waitbarSections, waitBar, 'Applying PSF');
    end
    stack = psf_gpu(stack,xy_smooth,z_smooth);
    stack = reshape(stack, [resY(iterations+1)*resX(iterations+1), num_images]);
    %%
    if isvalid(waitBar)
        waitbar(2/waitbarSections, waitBar, 'Differentiating');
    end
    if do_diff
        stackDiff = [stackDiff; diff(stack,1,2)]; % if you want differentiated
    else
```

```matlab
        stackDiff = [stackDiff; stack]; % if you want S-curve only
    end
    iterations = iterations + 1;
    %%
    if isvalid(waitBar)
        waitbar(3/waitbarSections, waitBar, 'Differentiating');
        delete(waitBar)
    end
    toContinue = questdlg(['Would you like to load another stack? (', num2str↵
(iterations), ' stack(s) so far)'], 'Stack selection', 'Yes', 'No', 'No');
    switch toContinue
        case 'Yes'
            keepOn = true;
        otherwise
            keepOn = false;
    end
end
%%
tic;
waitBar2 = waitbar(0,'Performing nnmf', 'Name', 'PCA progress');
options = statset('UseParallel',0);
[result_images_nums,result_spectra] = nnmf(stackDiff, dim, 'options', options);
result_images = zeros(max(resY), max(resX), iterations*dim);
timeTaken = toc;
% result_images = reshape(result_images, [resY, resX, iterations*dim]);
%%
start_read = 1;
for i = 1:iterations
    px = resX(i)*resY(i);
    result_images(1:resY(i),1:resX(i), (1:dim)+(dim*(i-1))) = reshape↵
(result_images_nums(start_read:(start_read+px-1),:),resY(i), resX(i), dim);
    start_read = start_read + px;
end
if isvalid(waitBar2)
    waitbar(1/2, waitBar2, 'Writing result files');
end
for h = 1:size(result_images, 3)
    imwrite(result_images(1:resY(ceil(h/dim)),1:resX(ceil(h/dim)),h)/max(max(max↵
(result_images))), [fileparts(imagePath), '\image_normAll', num2str(h), '.tif'])
    imwrite(result_images(1:resY(ceil(h/dim)),1:resX(ceil(h/dim)),h)/max(max↵
(result_images(:,:,h))), [fileparts(imagePath), '\image_normSelf', num2str(h), '.↵
tif'])
end
csvwrite([fileparts(imagePath), '\spectra.csv'], result_spectra')
if isvalid(waitBar2)
    waitbar(1, waitBar2, 'Writing result files');
    delete(waitBar2)
end
```

```matlab
%% asks user for nnmf input.
function [dim, xy_smooth, z_smooth, do_diff] = user_input()
%%
set(0,'units','pixels')
screensize = get(0,'screensize');
figure_width = 410;
figure_height = 190;
f = figure('MenuBar', 'none', 'Name', 'User input', 'Position',[(screensize(3)/2)-↙
(figure_width/2),(screensize(4)/2)-(figure_height/2), figure_width, figure_height]);

title_text = uicontrol('Style','text');
title_text.String = 'Please select the desired parameters for the non-negative↙
matrix factorization.';
title_text.Position = [5 130 400 50];
title_text.FontSize = 10;

dim_text = uicontrol('Style','text');
dim_text.String = 'Number of components to output';
dim_text.Position = [20 108 250 20];
dim_edit = uicontrol('Style', 'edit');
dim_edit.String = '2';
dim_edit.Position = [280 110 50 20];

xy_text = uicontrol('Style','text');
xy_text.String = 'Spatial smoothing sigma (px)';
xy_text.Position = [20 83 250 20];
xy_edit = uicontrol('Style', 'edit');
xy_edit.String = '0.5';
xy_edit.Position = [280 85 50 20];

z_text = uicontrol('Style','text');
z_text.String = 'Energy smoothing sigma (scales with energy step)';
z_text.Position = [20 58 250 20];
z_edit = uicontrol('Style', 'edit');
z_edit.String = '2';
z_edit.Position = [280 60 50 20];

diff_text = uicontrol('Style','text');
diff_text.String = 'Analyse differentiated spectra or S-curves?';
diff_text.Position = [20 33 250 20];
diff_popup = uicontrol('Style', 'popupmenu');
diff_popup.String = {'S-curves','Differentiated curves'};
diff_popup.Value = 1;
diff_popup.Position = [280 35 130 20];

ok_pushbutton = uicontrol('Style','pushbutton');
ok_pushbutton.String = 'Ok';
ok_pushbutton.Position = [180 10 50 20];
ok_pushbutton.Callback = @ok_push;

uiwait()

%%
    function ok_push(~,~)
```

```matlab
        %Validate inputs
        close_f = true;
        if str2double(dim_edit.String) > 0 % kicks out NaNs & other invals
            dim = str2double(dim_edit.String);
            if abs(round(dim) - dim) > 0.0001 % correct if not an integer
                close_f = false;
                dim_edit.String = num2str(round(dim));
            end
        else
            dim_edit.String = '2'; %reset to default value
            close_f = false;
        end
        if str2double(xy_edit.String) >= 0 %kicks out NaNs as well
            if str2double(xy_edit.String) < 0.0001 % tolerance for double float
                xy_edit.String = '0.0001'; % As Psf cannot deal with absolute 0
            end
            xy_smooth = str2double(xy_edit.String);
        else
            xy_edit.String = '0.5';
            close_f = false;
        end
        if str2double(z_edit.String) >= 0 %kicks out NaNs as well
            if str2double(z_edit.String) < 0.0001 % tolerance for double float
                z_edit.String = '0.0001'; % As Psf cannot deal with absolute 0
            end
            z_smooth = str2double(z_edit.String);
        else
            z_edit.String = '2';
            close_f = false;
        end
        switch diff_popup.Value
            case 1
                do_diff = false;
            case 2
                do_diff = true;
            otherwise
                diff_popup.Value = 1;
                close_f = false;
        end
        if close_f
            close(f)
        end
    end
end
```

```matlab
%%  Apply a point spread function using GPU
function filteredStack = psf_gpu(stackMatrix, GaussStdevXY, GaussStdevZ)
    inSigma = [GaussStdevXY, GaussStdevXY, GaussStdevZ];
    S=diag(inSigma); % defines the covariance matrix
    maxSize = 2*ceil(2*max(inSigma))+1;
    [gaussGridX, gaussGridY, gaussGridZ] = meshgrid(-maxSize:1:maxSize);
    coord=[gaussGridX(:) gaussGridY(:) gaussGridZ(:)];
    mu=mean(coord);
    outsize=size(gaussGridX);
    p = mvnpdf(coord, mu, S);
    nonIsoGauss = reshape(p,outsize);
    stackMatrix_GPU = gpuArray(stackMatrix);
    filteredStack_GPU = imfilter(stackMatrix_GPU, nonIsoGauss, 'replicate');
    filteredStack = gather(filteredStack_GPU);
end
```